UNIVERSIDADE ESTADUAL DE CAMPINAS
Faculdade de Engenharia Elétrica e de Computação

Igor Alves Maronni

An Impedance-Based Stability Analysis of a Deadbeat-Controlled Grid-Forming Inverter for AC Microgrids

Análise de Estabilidade Baseada em Impedância de um Inversor Formador de Rede para Microrredes CA

Campinas

2023

UNIVERSIDADE ESTADUAL DE CAMPINAS
Faculdade de Engenharia Elétrica e de Computação

Igor Alves Maronni

An Impedance-Based Stability Analysis of a Deadbeat-Controlled Grid-Forming Inverter for AC Microgrids

Análise de Estabilidade Baseada em Impedância de um Inversor Formador de Rede para Microrredes CA

Dissertation presented to the School of Electrical and Computer Engineering of the University of Campinas in partial fulfillment of the requirements for the Master's degree in Electrical Engineering, in the area of Electrical Energy.

Dissertação apresentada à Faculdade de Engenharia Elétrica e de Computação da Universidade Estadual de Campinas como parte dos requisitos exigidos para a obtenção do título de Mestre em Engenharia Elétrica, na Área de Energia Eletrica.

Supervisor: Prof. Dr. José Antenor Pomílio

Co-supervisor Dr. Joel Filipe Guerreiro

Este trabalho corresponde à versão final da dissertação defendida pelo aluno Igor Alves Maronni, e orientada pelo Prof. Dr. José Antenor Pomílio

Campinas

2023

Ficha catalográfica
Universidade Estadual de Campinas
Biblioteca da Área de Engenharia e Arquitetura
Rose Meire da Silva - CRB 8/5974

M347i

Maronni, Igor Alves, 1996-
An impedance-based stability analysis of a deadbeat-controlled grid-forming inverter for ac microgrids / Igor Alves Maronni. – Campinas, SP : [s.n.], 2023.

Orientador: José Antenor Pomilio.
Coorientador: Joel Filipe Guerreiro.
Dissertação (mestrado) – Universidade Estadual de Campinas, Faculdade de Engenharia Elétrica e de Computação.

1. Sistemas de energia elétrica - Estabilidade. 2. Eletrônica industrial - Sistemas de controle. 3. Impedância elétrica. 4. Eletrônica de Potência. 5. Inversores Elétricos. I. Pomilio, José Antenor, 1960-. II. Guerreiro, Joel Filipe, 1988-. III. Universidade Estadual de Campinas. Faculdade de Engenharia Elétrica e de Computação. IV. Título.

Informações Complementares

Título em outro idioma: Análise de estabilidade baseada em impedância de um inversor formador de rede para microrredes CA
Palavras-chave em inglês:
Electrical systems - Stability
Industrial electronics - Control systems
Electrical impedance
Power Electronics
Inverters
Área de concentração: Energia Elétrica
Titulação: Mestre em Engenharia Elétrica
Banca examinadora:
José Antenor Pomilio [Orientador]
Simone Buso
Tárcio André dos Santos Barros
Data de defesa: 26-01-2023
Programa de Pós-Graduação: Engenharia Elétrica

Identificação e informações acadêmicas do(a) aluno(a)
- ORCID do autor: https://orcid.org/0000-0002-9395-7885
- Currículo Lattes do autor: http://lattes.cnpq.br/2908320810259069

COMISSÃO JULGADORA - DISSERTAÇÃO DE MESTRADO

Candidato: Igor Alves Maronni RA: 155755

Data da Defesa: 26 de janeiro de 2023

Título da Tese: "An Impedance-Based Stability Analysis of a Deadbeat-Controlled Grid-Forming Inverter for AC Microgrid".

Prof. Dr. José Antenor Pomilio (Presidente)

Prof. Dr. Simone Buso

Prof. Dr. Tárcio André dos Santos Barros

A ata de defesa, com as respectivas assinaturas dos membros da Comissão Julgadora, encontra-se no SIGA (Sistema de Fluxo de Dissertação/Tese) e na Secretaria de Pós-Graduação da Faculdade de Engenharia Elétrica e de Computação.

To my family

Acknowledgements

Este trabalho foi resultado da colaboração de muitas pessoas. Daquelas que, mesmo de forma indireta, contribuíram com uma palavra, com um gesto de incentivo. Daquelas que me forneceram toda a base teórica necessária para o projeto. Daquelas que me mostraram como transformar a teoria em prática. Das pessoas que, mesmo durante uma conversa descontraída, puderam muito me ensinar, e cuja companhia no cafezinho da tarde, ou na carona para casa, foi essencial para me manter motivado.

Um agradecimento especial a minha família e a meus amigos por todo o apoio, sem o qual não teria sido possível chegar até aqui. Obrigado por sempre me incentivarem a correr atrás daquilo que eu quero e por acreditarem.

Agradeço ao meu orientador José Antenor Pomilio por todo o ensinamento desde o primeiro dia e por sempre estar disponível para ajudar. Obrigado por todas as aulas que me deu, sempre com sua capacidade de fazer os olhos de qualquer um brilharem quando o assunto é eletrônica de potência. Obrigado por sempre estar disposto a ensinar, mesmo nas conversas rápidas do dia a dia.

Ao meu coorientador, Joel Filipe Guerreiro, agradeço por me mostrar a direção, por me encaminhar rumo ao objetivo. Obrigado por todos os ensinamentos, desde as bases da formulação teórica até as etapas práticas do projeto, passando pelos valiosos detalhes da montagem experimental. Obrigado por todas as ricas discussões que tivemos e, principalmente, por acreditar em minhas ideias. Mas não somente — obrigado por me mostrar como colocá-las para funcionar.

Aos demais colegas de laboratório, obrigado pelo companheirismo ao longo do mestrado. Agradeço ao Hildo por todo o suporte direto ao projeto; sem sua colaboração, nada disso teria sido possível. Victor, obrigado por todo o apoio durante as montagens e ensaios experimentais. André, Eliabe, João, Mateus, Débora, Leonardo, agradeço pelos momentos de descontração, pelas conversas e desabafos, e pelos ensinamentos no dia a dia. Pude aprender bastante com vocês.

O presente trabalho foi realizado com apoio do processo nº 2020/09598-0, da Fundação de Amparo à Pesquisa do Estado de São Paulo (FAPESP). Agradeço também ao projeto de P&D PD-00063-3058/2019 - PA3058: "MERGE - Microgrids for Efficient, Reliable and Greener Energy", realizado em parceria com a CPFL Energia. Além disso, o presente trabalho foi realizado com apoio da Coordenação de Aperfeiçoamento de Pessoal de Nível Superior - Brasil (CAPES) - Código de Financiamento 001.

“Cette tête de l’homme du peuple, cultivez-la, défrichez-la, arrosez-la, fécondez-la, éclairez-la, moralisez-la, utilisez-la ; vous n’aurez pas besoin de la couper.”

(Victor Hugo in Claude Gueux, 1834)

Abstract

The electrical system has been through major changes towards a more decentralized organization, in which the concept of microgrids has gained importance. However, stability issues related to the increased penetration of power converters may arise due to the interaction among the converters themselves and the network. This problem has motivated the development of methods and criteria for the assessment of the overall system's stability, among which the impedance-based stability criteria have attracted attention. These criteria, though, require the impedances of the network to be known, which, in turn, can be identified by the power converters themselves. In this sense, this dissertation aims at the stability examination in an isolated-microgrid scenario, focusing on three main aspects—the impedance identification, the controller of a grid-forming inverter, and the stability assessment of an interconnected-converter system. For the identification, the cross-correlation method, based on the injection of pseudorandom binary sequences, is used. For all tested cases, the method presented a satisfactory accuracy for frequencies ranging from twice the fundamental component up to at least one tenth of the binary sequence generation frequency, which was adequate for both for controller and stability analyses. Concerning the second topic, the deadbeat predictive controller is thoroughly analyzed and tested. Impedance models for the grid-forming inverter are derived, and the identification method is used to experimentally measure its impedance. By comparing the measured impedance with the analytical model, the controller could be diagnosed and improved, reaching significant voltage distortion reductions on distorted current scenarios. Finally, concerning the third topic, the identification method is employed for the stability assessment of an interconnected system composed by the grid-forming inverter and an active rectifier, pointing out the practical challenges regarding the stability evaluation. It was shown that the discussed methods could correctly assess the overall stability; yet, safe margins must be considered in real applications due to identification accuracy limitations within certain frequency ranges. Besides, it was shown that the presence of passive impedances in the system—as line inductance—complicates the stability evaluation.

Keywords: Microgrids; Impedance-Based Stability Criteria; PRBS; Grid-Forming Inverter; Deadbeat controller.

Resumo

O sistema elétrico vem passando por grandes mudanças em direção a uma organização mais descentralizada, na qual o conceito de microrredes vem ganhando importância. No entanto, problemas de estabilidade relacionados à alta penetração de conversores eletrônicos podem surgir devido às interações entre os próprios conversores e a rede. Este problema motivou o desenvolvimento de métodos e critérios para a avaliação da estabilidade a nível de sistema, dentre os quais os critérios de estabilidade baseados em impedância ganharam relevância. Estes critérios, entretanto, requerem que as impedâncias da rede sejam conhecidas, as quais, por sua vez, podem ser identificadas pelos próprios conversores eletrônicos. Nesse sentido, esta dissertação tem como foco o estudo da estabilidade em um cenário de microrrede isolada, apoiando-se em três pontos principais: o método de identificação de impedâncias, o controlador de um conversor formador de rede e a avaliação da estabilidade de uma sistema formado por conversores interconectados. Para a identificação, o método de correlação, baseado na injeção de sequências binárias pseudoaleatórias, é utilizado. Em todos os casos testados, o método apresentou precisão satisfatória para a faixa de frequências compreendida entre duas vezes a componente fundamental e, pelo menos, um décimo da frequência de geração da sequência binária. Em relação ao segundo ponto, o controlador preditivo do tipo *deadbeat* é minuciosamente analisado e testado. Modelos de impedância são derivados para o conversor formador de rede, e o método de identificação é utilizado para medir experimentalmente sua impedância. Comparando a impedância medida com seu modelo analítico, foi possível diagnosticar e aprimorar o controlador, obtendo reduções significativas de distorção da tensão produzida em cenários com corrente distorcida. Por último, o método de identificação é empregado para a avaliação da estabilidade de um sistema composto pelo conversor formador de rede e um retificador ativo interconectados, destacando-se os desafios práticos envolvidos. Os métodos discutidos foram capazes de avaliar corretamente a estabilidade sistêmica; no entanto, margens de segurança devem ser utilizadas em aplicações reais devido a limitações na precisão da identificação para certas faixas de frequência. Além disso, mostrou-se que a presença de impedâncias passivas no sistema — como indutâncias de linha — tornam a avaliação da estabilidade mais desafiadora.

Palavras-chaves: Microrredes; Critérios de Estabilidade Baseados em Impedância; PRBS; Conversor Formador de Rede; Controle Deadbeat.

List of Figures

List of Tables

Contents

1 Introduction

In the last decades, the electrical system has been through major transformations. The electrical network was traditionally characterized by centralized, high-power plants that would provide power to distant consumers through lengthy transmission lines. The integration of renewable resources into the grid, however, fostered a change in the grid paradigm towards a more distributed system, in which the energy resources are sparsely located throughout the network via the so-called distributed energy resources (DER). Indeed, small-scale DERs—positioned closer to the consumers—have gained particular relevance, specially photovoltaic panels and wind turbines. As a consequence, even the power flow dynamics has changed, giving raise to the concept of *prosumer*—a consumer that does not exclusively use energy passively, but also produces electricity, becoming an active part of the grid.

This process was accompanied by an increase in the number of power electronics converters (PEC) in the electrical network, reaching all three generation, transmission, and distribution systems. Most renewable energy resources require an interface power converter in order to be connected to the grid. As suggested in Figure 1.1, the penetration of power-converter-based DERs tends to increase and to seize the role of the once dominant generators based on rotating machines—mostly synchronous generators. Also, the pursuit of a more efficient use of energy, driven by environmental concerns, has motivated the electrification of industrial processes and transportation, which implies the insertion of more PECs into the grid. This trend regards the average-consumer as well, whose ordinary electronic equipment—as computers and LED light bulbs—are connected to the utility through an electronic converter. Finaly, at the transmission level, PECs are present for supporting the grid through the use of FACTS (flexible ac transmission systems) or HVDC (high-voltage direct current transmission systems) (BOSE, 2013), for instance.

In this context, the integration of DERs and energy storage systems (ESS) facilitated the development of the so-called microgrids, which are defined in (IEEE. . . , 2018) as

> *"a group of interconnected loads and distributed energy resources with clearly defined electrical boundaries that acts as a single controllable entity with respect to the grid and can connect and disconnect from the grid to enable it to operate in both grid-connected or island modes."*

The microgrids have become an advantageous option for integrating DERs and ESSs in

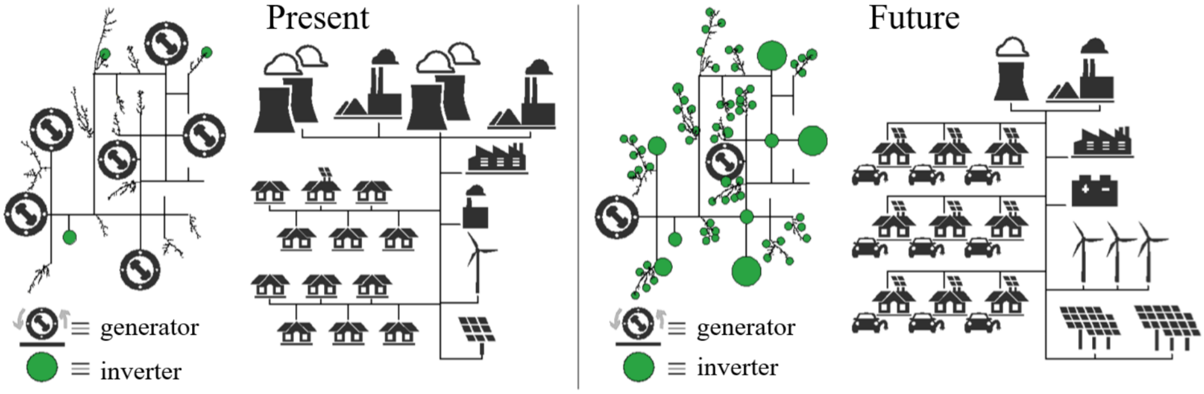

Figure 1.1 – Grid paradigm change towards a more inverter-based configuration, adapted from (LIN *et al.*, 2020).

an efficient, scalable, and reliable way. Efficient because its various control layers allows an optimized overall operation; scalable since new equipment can be easily added to the microgrid; and reliable considering that it can operate autonomously with respect to the main grid, which is essential in case of grid failure.

The PECs in a microgrid operate in different modes depending on their role (ROCABERT *et al.*, 2012). On the one hand, PECs interfacing renewable energy resources, as wind turbines and photovoltaic panels, are controlled such that the power provided by the primary source is delivered to the network. This is usually enabled by an adequate current control with a synchronization scheme, responsible for providing a reference of the grid voltage phase for the controller. The same is the case for converters interfacing batteries, whose charge and discharge may be determined by a current-controlled converter. The PECs operating as such are classified as *grid-following* converters, since they inject (or absorb) power into the grid in synchronism with the grid voltage. On the other hand, PECs that are voltage-controlled may be classified as *grid-forming* converters. These converters can be understood as voltage sources, whose output power is determined by the loads, and not by its control scheme. When an ac microgrid operates in island mode, disconnected from the grid, the voltages—which are not ensured by the utility grid anymore—have to be kept within normal levels of amplitude and frequency. Grid-Forming inverters (GFI) interfacing controllable energy resources, as batteries and fuel cells, are usually responsible for this task. As the name suggests, the GFIs are voltage-controlled inverters in charge of forming the ac voltages using a dc power source, and the voltage quality provided has to be satisfactory regardless of the nature of the loads within the microgrid boundaries, which may present current distortion and nonlinear behavior.

A simplified microgrid scheme is illustrated in Figure 1.2. The main elements composing the system are a battery, a set of solar panels, and a consumer unit with different kinds of loads, including electronic equipment. These components are connected at a point of common coupling (PCC) in the ac bus through different electronic converters. The microgrid itself is linked to the external grid through a switch (SW) that allows the system to disconnect and operate autonomously. Both converters interfacing the photovoltaic system and the electronic loads are current-controlled and operate in the grid-following mode, providing and draining power from the grid, respectively. The converter interfacing the battery, however, may operate in either grid-following or grid-forming modes. When the microgrid is in connected mode, the voltages in the system are ensured by the external grid. In this case, the converter operates in the grid-following mode, regulating the battery power flow. Nevertheless, for an islanded operation, the converter assumes the grid-forming mode and uses the stored energy to establish the voltage amplitude and frequency of the microgrid.

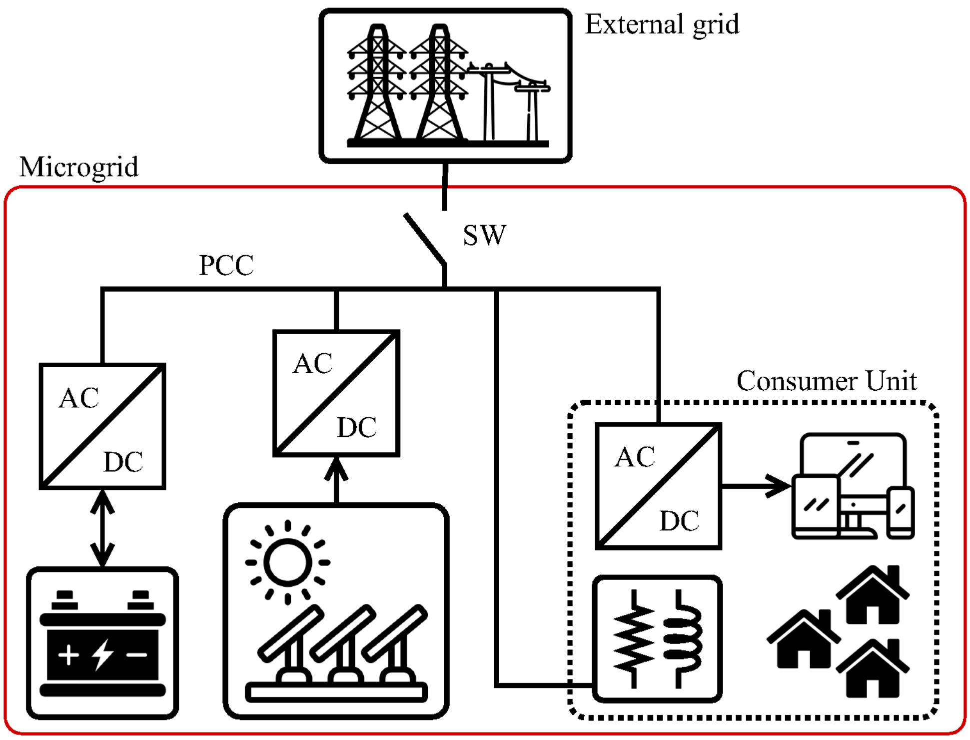

Figure 1.2 – Example of microgrid topology.

In such scenario, with high penetration of PECs, the stability should be a matter of concern since the presence of PECs may affect the dynamics of the system (HATZIARGYRIOU *et al.*, 2021). Problems may arise due to the reciprocal actions between the dynamics of the power converters. In a system with several converters, from different manufacturers, employing manifold control strategies, it is reasonable to say that the dynamics of one converter may interfere on the operation of the others, leading to undamped oscillations that can cause system failure. Indeed, this sort of problem has been reported in many works, as (WANG; BLAABJERG, 2019; YOON *et al.*, 2016; PENG *et al.*, 2019). This sort of instability issue is usually associated with the PEC's control scheme, and it will be the focus of this dissertation. In particular, the study developed in this work regards the stability of a GFI in an islanded microgrid scenario.

In response to this problem, effort has been made in developing new models and techniques to study the stability of interconnected-converters systems (MU *et al.*, 2020; PENG; YANG, 2020; SALIS *et al.*, 2017). Two approaches are usually employed for that purpose: the eigenvalues analysis and the impedance-based stability criteria (IBSC) (WANG; BLAABJERG, 2019; AMIN; MOLINAS, 2017). The eigenvalues analysis provides accurate conclusions about the small-signal stability at a specific operating point and offers a satisfactory understanding about which modes of the system mostly affects the stability (WANG *et al.*, 2017). However, it requires a precise state-space modeling of the system, which may be a tough task depending on the model order. The IBSC, in turn, rely just on the frequency response of the terminal characteristics of the interconnected devices, allowing the system to be treated as a black-box if needed (ABDOLLAHI *et al.*, 2020). This class of criteria was firstly introduced in the same year by (UNDRILL; KOSTYNIAK, 1976) and (MIDDLEBROOK, 1976) for the analysis of subsynchronous oscillations of power systems, and for the design of input filters for dc-dc converters, respectively. Later, the work in (SUN, 2011) applied the IBSC to the stability analysis of grid-connected converters. This criteria will be discussed further in Chapter 2; however, in a nutshell, such criteria elucidate the influence that the small-signal impedances of the converter and of the grid has over the overall system stability. Thus, as the main consequence, the stability of the system is affected by any topological change in the network (as load connections/disconnections), as well as by any adjustment in the control schemes of the interconnected converters, since their impedance depends on the controllers in use.

A requirement for applying the IBSC is that the impedances involved are known. For that purpose, system identification techniques must be useful (LJUNG, 1999; PINTELON; SCHOUKENS, 2012), specially the ones that can be employed in an online fashion, i.e. applied to the system in real-time during normal operation; indeed, offline identification is usually insufficient in this context since the impedance of the grid varies over time. In order to apply the identification techniques to real systems, the PECs themselves can be used. Most methods utilize the PECs to excite the system with a disturbance of well-known spectral content in such a way that the small-signal frequency response of the impedance can be measured. In (CESPEDES; SUN, 2012), for instance, the authors perturb the system with an impulse using an inverter to measure the grid impedance. Similar procedure is employed in (ROINILA *et al.*, 2013), which also includes a comparison between injecting an impulse and injecting another disturbing signal—the maximum-length pseudorandom binary sequence (PRBS).

The binary sequences are wideband signals usually employed along with the cross-correlation method (CCM), which is a nonparametric identification technique ubiquitously utilized in the context of power electronics. In (BARKLEY; SANTI, 2009) and (MIAO *et al.*, 2005), this method was used for identifying the control-to-output frequency response of a dc-dc converter, and, in (MARTIN; SANTI, 2014), it was used for determining the ac-filter inductance of a deadbeat-current-controlled inverter. In (ABDOLLAHI *et al.*, 2020), the PRBS is used for assessing the stability of a dc network and, in several works (ROINILA *et al.*, 2014; ROINILA *et al.*, 2018; MARTIN *et al.*, 2013), it is used for identifying the grid impedance. Moreover, the work in (LUHTALA *et al.*, 2018) uses the grid impedance identified via PRBS along with the theoretical model of the inverter impedance to conclude about the inverter-grid system stability.

Assessing the stability of the network is important since this information can be used by the PECs to act and avoid unstable operations by changing control parameter values and, consequently, shaping the PEC's impedance. This is the principle behind adaptive controllers, and the identification via PRBS is utilized in several works for this purpose. In (ROINILA *et al.*, 2019), the authors propose a strategy for the adaptation of the impedance of the converters in a multiconverter system through a positive feedforward technique. In this case, the information acquired via PRBS is utilized to adapt the parameters of the feedforward path. Similar reasoning is found in (KHODAMORADI *et al.*, 2020), in which the control loops of a multiconverter system are measured through PRBS and then used to change the voltage-loop gain of the converters.

In view of the new challenges regarding the electrical system, this dissertation aims to study the stability of a single-phase GFI through the impedance-based criteria in an islanded microgrid scenario. Concerning the GFI controller, different control strategies have been proposed in the literature—as reviewed by (LIU *et al.*, 2020)—among which the deadbeat (DB) predictive controller appears as an attractive technique due to its high-bandwidth character. This controller appears in many works in the literature. In (BUSO *et al.*, 2001), a design procedure is presented for a DSP-based implementation of the DB controller. Later, a higher-bandwidth FPGA-based version is presented in (BUSO *et al.*, 2015). In (BUSO *et al.*, 2019), a FPGA-based version was used in the inner loops of a current-controlled inverter. The DB controller version implemented in this work will be described and thoroughly analyzed in further chapters.

This dissertation is organized as follows. Chapter 2 introduces the stability issues in converter-based networks and presents the impedance-based stability criteria, which rely on the frequency responses of the inverter and grid impedances. In Chapter 3, it is shown how these impedances can be identified. The principles behind the PRBS and the cross-correlation method are presented, and two identification post-treatment strategies are proposed and compared through simulation and experimental results. The

GFI control strategy is presented in Chapter 4, in which the DB predictive controller is described. Also, the GFI performance is experimentally evaluated considering different scenarios. In Chapter 5, the DB-GFI impedance model is presented and the results of the GFI impedance identification performed by another inverter are discussed. From the experimental impedance measurement, the DB controller is diagnosed and improved. In Chapter 6, the stability of a two-converter system—composed by the GFI supplying an active rectifier—is discussed and experimentally evaluated. Finally, the main conclusions and future work are presented in Chapter 7.

As the main contributions of this work, can be listed the post-treatment methods for the impedance identification in ac systems, the detailed DB-GFI impedance analysis followed by the improvement of the controller based on its impedance characteristics, and the discussion on some practical challenges related to the stability assessment in a multi-converter system presenting non-negligible line impedances or passive loads.

2 Impedance-Based Stability Analysis

The presence of PECs introduce some challenges regarding their wide-range frequency behavior. Some authors use the term *harmonic stability* (WANG; BLAABJERG, 2019) to refer to the multiple-timescale interactions that exist between the converter and the network to which it is connected, which may include other electronic devices, specially in an islanded microgrid scenario. This kind of stability issue mostly regards the control schemes of the converters, and is the one that will be addressed in this work. As an example, Figure 2.1, obtained from (WANG; BLAABJERG, 2019), illustrates the different frequency rages involved in the control of a PEC. To illustrate, it takes an inverter with cascaded control. The inner loop regulates the output current in the *dq* reference frame while the external voltage loop regulates both the dc and the ac voltage—whereas the dc voltage controller regulates the active power, producing the *d*-current reference, the ac voltage controller generates the *q*-current reference, thus regulating the reactive power injected or absorbed from the grid. For the reference frame transformation and for synchronization purposes, a PLL is needed as well. The different bandwidths involved interact with the grid impedance and may cause instabilities in different frequencies, ranging from the sub-synchronous zone up to the switching frequency and beyond.

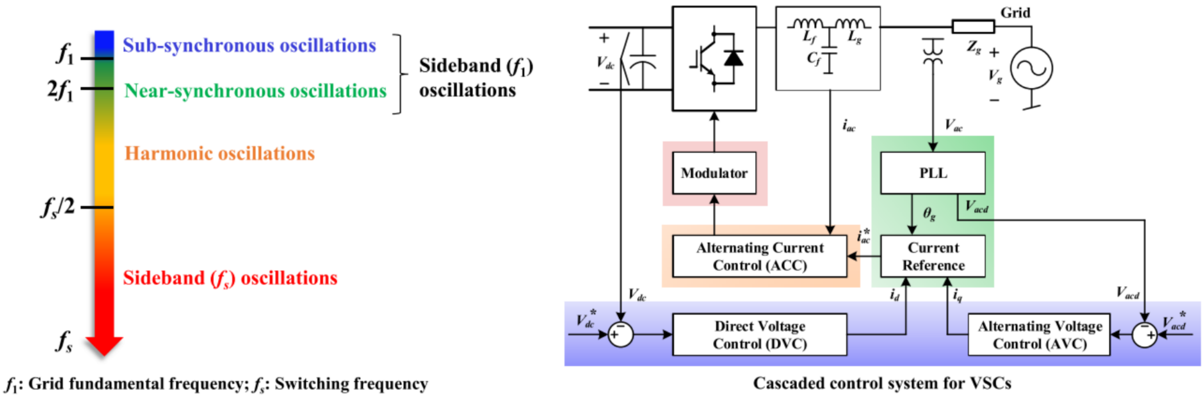

Figure 2.1 – Phenomena of different frequency ranges in an inverter control system (WANG; BLAABJERG, 2019).

The harmonic stability issues are complex—sometimes with more than one cause or phenomena involved—, and it still represents a challenge in terms of system modeling and analysis. Besides, the problem scales faster when more PECs are connected to the same network. Nevertheless, this issue becomes more tangible when analyzed in terms of impedances, as will be discussed in the following paragraphs.

As mentioned in Chapter 1, there are two main approaches commonly utilized to assess the stability of converter-based networks. The first one is the eigenvalue analysis using the state-space representation of the system, following standard procedures of the classical control theory. This approach can provide a better understanding on which modes (or states) of the system are related to stability issues. This can be done through the application of participation analysis (WANG *et al.*, 2017). For obtaining reliable conclusions, however, the eigenvalue analysis requires a detailed, precise model of the system. Unfortunately, depending on the amount of converters, the model order may become relatively high, which introduces computational and analytical complexity (MU *et al.*, 2020). Besides, not all parameters of the system are always available, which may undermine the model accuracy. Another drawback of this method is the lack of flexibility and scalability in the sense that it is not trivial to factor in new devices into the analysis if needed. Hence, if new converters, for instance, join the grid, the model has to be reconsidered.

The second approach regards the subject of this chapter—the IBSC—which rely on the small-signal impedances of the converters and loads composing the grid, as will be further explained in section 2.1.1. This approach does not necessarily require a complete model since the impedances of interest can be assessed through measurement or any estimation method (MARONNI *et al.*, 2021; ABDOLLAHI *et al.*, 2020). This class of criteria is also useful in the design phase of converter's control systems—the controller can be designed such that the converter presents an impedance that ensures stable operation with a certain safe margin. Besides, the IBSC offer more flexibility and scalability compared with the state-space modeling; in fact, if the impedances can be measured, no difficulty is introduced upon system topology change. The main drawback of this approach, however, is that it does not provide a precise knowledge of the oscillatory or unstable modes, i.e. the state variables related to the instability are not explicitly highlighted (LI *et al.*, 2021).

Recently, other methods have arisen in order to compensate for the drawbacks of both approaches. The Component Connection Method, for instance, appeared as a modeling technique through which the state-space representation can be retrieved in a modular fashion, i.e. by modeling each equipment composing the system separately, and then linking the models together via algebraic relationships (WANG *et al.*, 2017). The main advantage of this method is that it approximates the eigenvalue analysis to the IBSC with respect to its scalability property. Looking at the other way round, the IBSC can also provide some insights on the phenomena affecting the stability of the system if analytical impedance models are available. In (LI *et al.*, 2021), for example, a "gray-box" impedance model is presented for a grid-forming inverter, providing an intuitive visualization of the influence of each control feature on the stability of the system, with no loss of the flexibility that is inherent in the IBSC.

In this work, the IBSC will be employed due to their advantages over the eigenvalue stability analysis, specially because this approach becomes more suitable when it comes to online stability assessment since the impedances can be measured or identified in real time. Hence, in the next section, the IBSC will be further explored, aiming to unravel some concepts that are sometimes mixed-up, and to give an overview on the existing IBSC.

2.1 The Impedance-Based Stability Criteria

2.1.1 General Principles

The IBSC are based on the principle that every power converter can be modeled in terms of its Thevenin's or Norton's equivalent circuits, with their respective impedances, which depend on the physical components of the converter—as filters—and on its control scheme. To apply the IBSC, the network can be modeled as two different subsystems connected at a point of common coupling (PCC); typically, a load and a source subsystems expressed on their Thevenin's or Norton's representation whether they are voltage- or current-controlled, respectively (SUN, 2011). Also, it is important to highlight that this analysis is valid either for ac or dc networks, since this is a small-signal approach. For the sake of simplicity, the discussion herein presented considers that each subsystem is composed only by one load or one converter, although each of them could represent an association of several devices. The systems depicted in Figure 2.2 will be used as references in the following explanation. It shows four situations, representing different combinations of voltage-controlled sources (Z), current-controlled sources (Y), and passive loads (Load).

The IBSC are numerous and can be classified into different groups, which may differ from author to author. In this section, two major categories will be exposed: the methods based on the definition of an impedance ratio—called the minor-loop gain (MLG)—, and those based on the passivity properties of the impedances. Other categories can be found in works such as (LIAO; WANG, 2020).

2.1.2 MLG-Based Criteria

Taking the Z+Y system depicted in Figure 2.2b, the current i through the circuit can be written in the frequency domain as

$$i(s) = \frac{I_2(s) - V_1(s)Y_2(s)}{1 + Z_1(s)Y_2(s)} = [I_2(s) - V_1(s)Y_2(s)] \cdot \frac{1}{1 + MLG(s)}, \tag{2.1}$$

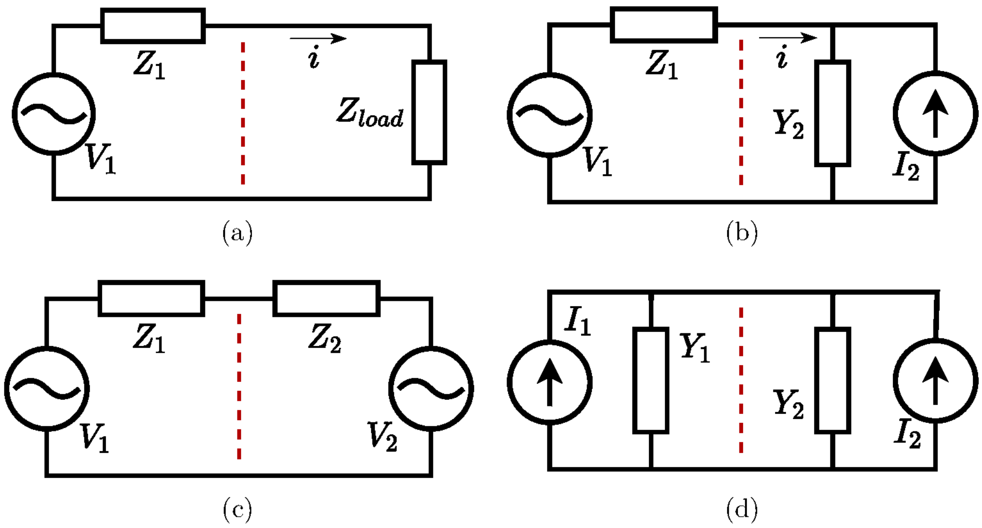

Figure 2.2 – System models for IBSC application. (a) Z+Load system, (b) Z+Y system, (c) Z+Z system, and (d) Y+Y system.

where the MLG is defined as the ratio between the impedances of the voltage and the current sources, $Z_1/Z_2 = Z_1Y_2$. Note that the MLG is equivalent to the feedback gain of a controlled system—as its name suggests. Hence, from (2.1), in order for the system to be closed-loop stable, the following conditions have to be simultaneously satisfied:

1. V_1 is stable;
2. I_2 and Y_2 are stable;
3. the MLG satisfies the Nyquist Stability Criterion (NSC).

Conditions 1 and 2 are equivalent to say that the voltage-source and the current-source converters are individually stable by design, respectively. Similar conditions can be found for the other scenarios shown in Fig. 2.2, each of them having a different MLG definition, as shown in Table 2.1. Since it is plausible to consider that the inverters are individually stable by design—which implies on stable voltage/current sources and on stable impedances—, it is common practice to look only at the third condition to conclude about the stability.

Table 2.1 – MLG Definition

System type	MLG
Z+Load	Z_1/Z_{load}
Z+Y	Z_1Y_2
Z+Z	Z_1/Z_2 or Z_2/Z_1
Y+Y	Y_1/Y_2 or Y_2/Y_1

From the reasoning above, different stability criteria have arisen. One class of criteria, for instance, consists of defining special regions on the complex plane through which the frequency response of the MLG is not allowed to pass. These are the so-called *forbidden regions* criteria. Such criteria are based on the fact that the MLG cannot encircle the critical point $-1 + j0$ in order for the closed-loop system to be stable, satisfying the NSC. Figure 2.3, obtained from (RICCOBONO; SANTI, 2014), exemplifies the concept of forbidden regions. The red circle, for instance, represents the criterion defined by Middlebrook, which establishes that, if the MLG frequency response is confined within this circle, the critical point is surely not going to be encircled; therefore, stability is ensured. Note, however, that this is a sufficient but not necessary condition. Indeed, the MLG could transit through other areas without reaching the critical point. That is the major reason why other less conservative criteria arose and tried to expand the allowed regions while keeping the MLG away from the critical point, as illustrated in Figure 2.3 as well. Since the forbidden regions criteria establish sufficient conditions for stability, they are not able to tell for sure when a system is unstable. Hence, these criteria are not very helpful when a detailed stability analysis is required. Yet, they are certainly convenient at the design phase of power converters, for the converter's impedance can be shaped such that the stability is guaranteed.

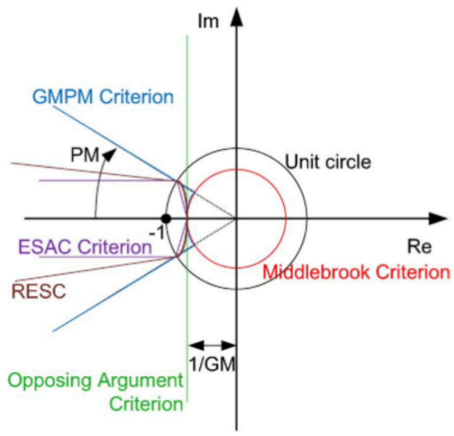

Figure 2.3 – IBSC based on forbidden regions (RICCOBONO; SANTI, 2014).

The reader must have noticed that the forbidden regions criteria do not consider the existence of unstable poles in the MLG. Actually, the NSC states that a system is stable if and only if its open-loop transfer function encircles the critical point N_p times counterclockwise, being N_p the number of open-loop unstable poles (LIAO; WANG, 2020). Thus, making the MLG avoid the critical point only implies stability if the MLG has no unstable poles.

Nevertheless, unstable poles may be present depending on the system configuration. For the Z+Load system in Fig. 2.2a, any unstable pole appearing in the MLG would be either an unstable pole of Z_1 or an unstable pole of Y_{load}. Both options would only be true if the inverter or the load were individually unstable, respectively. The same can be concluded about the Z+Y system (see Fig. 2.2b), whose MLG is similarly defined as Z_1Y_2. Thus, unstable poles are not supposed to be present in these kinds of system. However, the scenario is different for Z+Z and Y+Y systems where unstable poles may appear in the MLG even if both converters are stable by design. For these systems, the MLG is given by Z_1/Z_2 or Z_2/Z_1, and by Y_1/Y_2 or Y_2/Y_1, respectively, as shown in Table 2.1. As a consequence, impedance or admittance unstable zeros may become unstable poles in the MLG, as discussed in (LIAO; WANG, 2020) and (LIU *et al.*, 2014). Moreover, for the fact that the MLG-based IBSC depend on the arbitrarily chosen PCC, unstable poles may appear for specific choices of the PCC, but not for others.

Having unstable poles in the MLG is not a problem as long as the closed-loop transfer function remains stable; however, the stability assessment becomes more complicated. For instance, the forbidden regions methods are no longer valid, and if the stability is to be assessed via the identification of the MLG frequency response in a black-box fashion, one must take extra care and know beforehand about the existence of unstable poles in order not to lead to mistaken conclusions, as recommended in (MARONNI *et al.*, 2021). Moreover, unstable open-loop responses precludes the definition of accurate phase or gain stability margins, which makes it more challenging to predict how far the system is from instability. In conclusion, for the general case, the complete NSC, with no simplifying hypotheses, has to be applied to the MLG to properly conclude about the stability of the system.

2.1.3 Passivity Criterion

The principle behind the Passivity Criterion is that passive electrical components (resistors, capacitors, and inductors) are naturally stable, i.e. when supplied by ideal voltage sources, they produce stable currents. Hence, this criterion states that, if the total impedance of the bus to which the converters and loads are connected presents a passive behavior, the system will be stable. An impedance $Z(j\omega)$ is passive if the following two conditions are satisfied (RICCOBONO; SANTI, 2014):

1. $Z(j\omega)$ is stable, i.e. it has no unstable poles;

2. $\mathrm{Re}\{Z(j\omega)\} \geq 0, \forall\omega$, which is equivalent to $-90^\circ \leq \arg\{Z(j\omega)\} \leq 90^\circ, \forall\omega$.

In other words, if the total bus impedance is confined within the right half-plane (RHP) of the complex plane, the system will be stable. As the forbidden regions criteria, only a sufficient condition can be derived by looking at the passivity of the impedance—in case it is not passive, no conclusion can be stated about the stability of the system.

In a PEC-dominated system, however, it is unlikely that all devices are passive for all frequencies since the controllers themselves may introduce negative-real-part regions in the impedance. As discussed in (HARNEFORS *et al.*, 2016), the controller total time delay (PWM plus computation delay), the dynamics of the control loops, and the phase-locked loop (PLL) dynamics can make the converter's impedance become nonpassive for certain frequency ranges. Even though it is not feasible to have a passive behavior for all frequencies, it remains important to reduce the nonpassive regions whenever possible from the passivity criterion point of view.

Some works apply the passivity concept to the MLG-based criteria. Indeed, the problem can be formulated as for the MLG-based criteria—instead of looking at the total bus impedance, one can carry the analysis in terms of an impedance ratio (MLG) as well. If the impedances composing the ratio are both passive, the MLG readily satisfies the Nyquist criterion (PETRIC *et al.*, 2022).

The concepts of MLG and passivity will be used throughout this work, specially in Chapters 5 and 6, in which the GFI impedance model is derived and the MLG of a two-converter system is analyzed. Before this, next chapter will expose how the frequency response of an impedance can be identified.

3 System Identification for Stability Assessment

Chapter 2 has introduced the stability-related problems around networks with high penetration of PECs and has presented the impedance-based approach for analyzing the stability of such systems. Now, this chapter advances to the discussion on how the frequency response of the impedances can be identified.

The small-signal behavior of a linear system can be estimated by injecting a known disturbance at its input and measuring the corresponding response at the output. There are several possible options for selecting a disturbing (or exciting) signal. The simplest one is a pure sinusoidal wave of a given frequency. The response of the system, i.e. its gain and phase, can be obtained by looking at the amplitude and the phase shift of the sinus acquired at the output. This procedure, however, only provides information for one specific frequency. If needed, an ac-sweep (LJUNG, 1999) can be done by varying the frequency of the injected sinus in order to cover more frequency points.

In complex system, as those with power converters, the dynamics of interest are likely to be spread throughout a wide spectrum, ranging from frequencies as low as fractions of Hz to frequencies near and beyond the switching frequency, reaching hundreds of kHz. Because of that, using wideband exciting signals in lieu of narrow-band ones is preferable. Whereas for the latter the power spectrum is concentrated within small frequency ranges (or just in a single frequency for the pure sinus wave), the wideband signals exhibit a power spectrum distributed over several frequencies. Covering a large frequency range in the identification process is less time-consuming when using wideband signals, which is a desirable feature in most applications.

Minimizing the impedance identification duration is important due to many reasons. Firstly, reducing the total disturbance-injection time is essential to prevent the system from deviating from the operation point. Moreover, during the injection, the voltages and currents of the system will be affected by the disturbance, which may either become a power-quality problem or interfere in the operation of other devices if the injection lingers on. Secondly, the impedance of a network usually presents a time-varying behavior for the fact that converters and loads can be connected and disconnected at random, converters may change their operating points, system failures may occur, etc (ROINILA *et al.*, 2021). Hence, the longer it takes to complete one identification experiment, the higher will be the probability of acquiring samples that does not correspond to the same state of the network, leading to incorrect results. That is also one of the motivations behind the necessity of carrying out online identifications. Besides, minimizing the identification time can save computational resources that are usually scarce in embedded systems.

Among the wideband signals, the binary sequences represent a suitable choice in the context of impedance identification. First of all, the idea is that the PECs themselves should be able to perform the identification; thus, the binary sequences become an easy-to-generate option that can be applied at the control level of the converters. Also, these sequences present a considerably high ratio between spectrum energy and time-domain amplitude (PINTELON; SCHOUKENS, 2012), which means that the disturbance amplitude usually does not need to be very high in order to excite the system above the noise level. Moreover, compared to other wideband signals, such as the impulse and the step, the spectral content of the binary sequences is stronger—with respect to the time-domain peak—and more controllable through design (ROINILA *et al.*, 2021).

A good review on different types of binary sequences can be found in (ROINILA *et al.*, 2021), in which the authors describe the maximum-length binary sequences (MLBS), the inverse-repeat binary sequence (IRS), the discrete-interval binary sequences (DIBS), and the orthogonal binary sequences (OBS). The MLBS are what is usually simply called pseudorandom binary sequences (PRBS). The PRBS will be presented in details in section 3.2, but, in a nutshell, they are white-noise-like sequences that present nonzero spectrum power at a large range of discrete frequencies. The IRS have similar characteristics except that they also provide immunity against even-order nonlinearities (at the expense of being longer than the PRBS), which is a noteworthy characteristic since the majority of converter systems are ultimately nonlinear. Differently from the PRBS and the IRS, the DIBS can be designed to have energy only at specified harmonics, which may be interesting in cases where the signal-to-noise ratio (SNR) is a matter of concern and the spectral energy has to be properly tuned (ROINILA *et al.*, 2014). Finally, the OBS are binary sequences that are orthogonal among them, i.e. that do not contain energy at the same frequencies, which enables the simultaneous identification of different transfer functions without one interfering on the others (KHODAMORADI *et al.*, 2020; ROINILA *et al.*, 2019).

In this work, the PRBS in its simplest form will be used along with the cross-correlation method (CCM) for the online identification of impedances in ac systems. In the next sections, the CCM is introduced and the design procedure for the PRBS is explained. Then two different data post-treatment methods are presented and compared through simulation and experimental results.

3.1 The Cross-Correlation Method

The cross-correlation method (MIAO *et al.*, 2005; BARKLEY; SANTI, 2009) is one of the nonparametric techniques for system identification by means of which the frequency response of a "black-box" system can be assessed. The principle of this method is to properly design an input signal (u) such that the step response (h) of the system is directly given by the cross-correlation (R_{uy}) between the measured output (y) and the input, regardless of any system disturbance (v) at the output. Once the step response is obtained, the Fast Fourier Transform (FFT) can be applied to obtain the system frequency response.

The output y of a discrete–time, linear, time invariant system can be written as

$$y(n) = \sum_{k=1}^{\infty} h(k)u(n-k) + v(n). \tag{3.1}$$

Assuming that u and v are centered, second-order stationary, uncorrelated, random signals (GODOY, 2014), the cross-correlation between output y and input u can be written as

$$\begin{aligned} R_{uy}(m) = \sum_{n=1}^{\infty} u(n)y(n+m) = \sum_{n=1}^{\infty} u(n)\left[\sum_{k=1}^{\infty} h(k)u(n-k+m) + v(n+m)\right] = \\ \sum_{m=1}^{\infty}\sum_{k=1}^{\infty} h(k)u(n)u(n+m-k) + R_{uv}(m) = \sum_{k=1}^{\infty} h(k)R_{uu}(m-k) + R_{uv}(m), \end{aligned} \tag{3.2}$$

where R_{uu} is the auto-correlation of the input signal and R_{uv} is the cross-correlation between the input and the disturbance. From the hypotheses for u and v, $R_{uv} = 0$ and (3.2) can be rewritten as

$$R_{uy}(m) = \sum_{n=1}^{\infty} u(n)y(n+m) = \sum_{k=1}^{\infty} h(k)R_{uu}(m-k). \tag{3.3}$$

Equation (3.3) states that R_{uy} is equal to the convolution between the system's impulse response and the auto-correlation R_{uu}. Thus, it is equivalent to say that R_{uy} will be the output of the system when it is excited by the input R_{uu}. If u is chosen to be white noise, R_{uu} will be simply given by an impulse at the origin, and, by definition, the aforementioned hypothesis concerning the disturbance v is satisfied. Thus, (3.3) becomes

$$R_{uy}(m) = \sum_{k=1}^{\infty} h(k)\delta(m-k) = h(m). \tag{3.4}$$

Hence, when the system is excited by a white noise, the impulse response is readily given by the cross-correlation between the output and the input. Once R_{uy} (or, equivalently, h) is obtained, the FFT can be applied to it in order to obtain the system's frequency response.

The feature presented in (3.4) will only be verified if the input signal is imbued with white-noise-like properties. Since it is not easy to digitally generate a real white noise, the maximum-length pseudorandom binary sequence (PRBS) is often selected as an alternative (BARKLEY; SANTI, 2009). Nevertheless, the PRBS must be cautiously designed depending on what is desired to be identified, as discussed in the following.

3.2 Pseudorandom Binary Sequencies (PRBS)

A PRBS is a periodic, deterministic signal that can be easily created via a linear-feedback shift register (LFSR) by means of a XOR operation between two well-determined bits, as exemplified in Figure 3.1. The number of bits N of the LFSR determines the length $M = 2^N - 1$ of a single period of the PRBS. The output binary values are scaled to a desired amplitude e so that the sequence presents zero average. The PRBS must be properly designed—the number of bits (N), the number of periods (P), the amplitude (e), and the PRBS generation frequency (f_0), must be carefully chosen according to the application and the characteristics of the system to be identified.

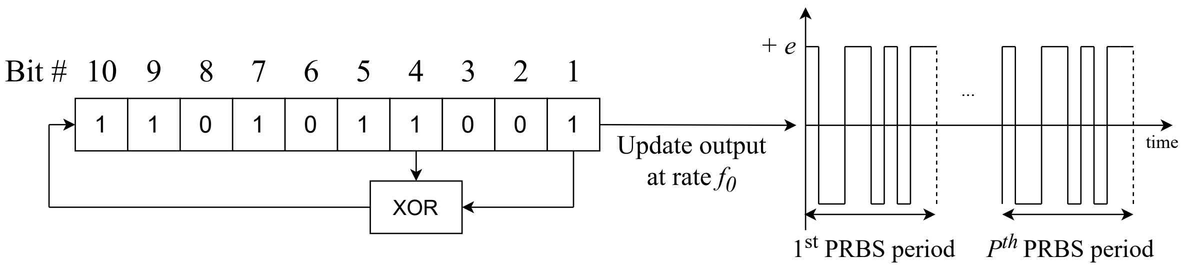

Figure 3.1 – Example of a 10-bit, maximum-length PRBS generation.

Figure 3.2 shows the continuous-time auto-correlation function of an infinite-period PRBS (HAMPTON, 1965). Note that R_{uu} is formed by triangles of peak equal to e^2 that repeat with a period corresponding to the duration of a single PRBS. Also, R_{uu} assumes a constant value of $-e^2/M$ between the triangles. If M is selected to be large enough, the terms $-e^2/M$ tend to zero and, assuming that $\Delta t = 1/f_0$ is very small, R_{uu} becomes an almost ideal impulse train, as needed for the cross-correlation method.

The PRBS power spectrum Φ_u may give more intuitive insights about the parameters choice. It is possible to show that Φ_u is given by

$$\Phi_u\left(f = \frac{kf_0}{M}\right) = \frac{e^2(M+1)}{M^2} sinc^2\left(\pi \frac{f}{f_0}\right), k = \pm 1, \pm 2, ... \pm \infty, \tag{3.5}$$

and that $\Phi(0) = e^2/M^2$ by applying the Fourier transform to $R_{uu}(\tau)$. Figure 3.3 illustrates the power spectrum function, which is composed only by uniformly-spaced discrete frequency values. The main consequence of this fact is that the frequencies that can be

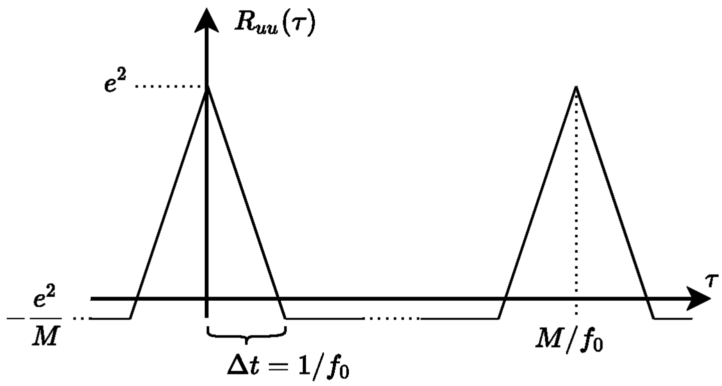

Figure 3.2 – PRBS auto-correlation function $R_{uu}(\tau)$.

identified are not continuously distributed through the spectrum as for a white-noise excitation. Actually, the PRBS implies a frequency resolution $\Delta f = f_0/M$, which also represents the lowest frequency component that can be identified. Due to the *sinc* envelope, the majority of the energy is concentrated bellow $0.4f_0$ (where a $-3\,\mathrm{dB}$ magnitude drop occurs). Thus, the generation frequency has to be selected accordingly, in a way that the highest frequency of interest be located within this range; otherwise, the noise of the experiment may undermine the identification for high frequencies. Note that there is also a trade-off between the frequency resolution and the maximum frequency that can be identified—the higher is f_0, the higher will be the maximum frequency, but the poorer will be the resolution and the low-frequency identification. This trade-off, however, can be balanced by choosing M wisely—for larger M, a better frequency resolution is obtained at the expense of reducing the PRBS energy.

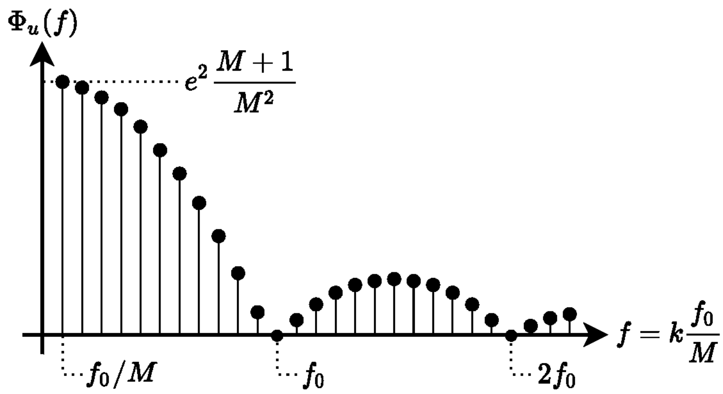

Figure 3.3 – PRBS power spectrum $\Phi_u(f)$.

The amplitude of the PRBS must be carefully chosen as well. On the one hand, e must be sufficiently high so as to excite the system above noise levels. On the other hand, if a very high amplitude is chosen, the system may deviate from the linear approximation, causing nonlinear artifacts to appear. In noisy systems, a good way to improve the SNR without increasing e is utilizing several PRBS periods. By doing so, the data corresponding to each period injection can be averaged. Since the noise is random and uncorrelated, it tends to vanish when averaged over several acquisition periods (MIAO *et al.*, 2005). It is important to point out, however, that if the total acquisition extends for a very long time, the system may diverge from the operation point and the linearity may no longer be valid. Moreover, dealing with larger data-sets requires more memory and computational effort (ROINILA *et al.*, 2021). Hence, there also exists a trade-off between the choice of the amplitude e and the number of periods P.

Despite being a versatile, easy-to-generate, exciting signal with a well-behaved spectrum, the PRBS presents some drawbacks as well. The main one is that it exhibits worse performance upon nonlinearities. When a linear system is perturbed by a signal with a certain frequency, only this frequency will be excited and therefore present at the output; for nonlinear systems, however, the response may be spread over several other frequencies that were not in the input signal. As the PRBS is able to excite several frequencies at once, a nonlinearity may cause frequency overlap at the output. Another drawback is that, in extremely noisy environments, the amplitude of the PRBS may be very high or the acquisition length may be very long in order to overcome the noise. This is due to the fact that the spectral power of the PRBS is distributed over a wide range, and that the amplitude of each frequency component cannot be individually tuned (as for the DIBS, for example) (ROINILA *et al.*, 2021).

3.3 Impedance Identification Using PECs

To perform the identification, it is preferable to use the converters that already exist in the network. By doing so, no additional equipment or sensors have to be added to the system, and the converter can use the measured frequency response to undertake corrective actions whenever the stability is at risk. This sort of adaptive technique will be explored in future work. For the identification, the idea is that the PECs themselves should be able to inject the disturbance into the system, acquire the desired data, and perform the calculations in order to complete the identification process.

In (MARTIN *et al.*, 2013), the PRBS is injected directly into the PWM such that the converter works as a power amplifier for the disturbance. In works like (ROINILA *et al.*, 2014; ROINILA *et al.*, 2018; LUHTALA *et al.*, 2018) the PRBS is superposed to the current reference of a three-phase, dq-frame-controlled inverter to identify the grid impedance. In (ROINILA *et al.*, 2019) the PRBS is also injected into the current reference, but for a dc-dc converter. The point of injection must be chosen according to the application—a transfer function analysis can be done in order to select it. The authors in (RICCOBONO *et al.*, 2018) adopt the strategy of adding the disturbance at several points. The converter under discussion was a three-phase inverter controlled in the dq domain through two cascaded control loops (an inner current loop and an outer voltage loop). The authors injected the PRBS at three different points with different weights—at the PWM level, and over the current and voltage references. By doing so, they avoided the spectral power of the disturbance being attenuated by the control system before reaching the PCC.

Figure 3.4 illustrates an example in which a single-phase inverter is used to identify the impedance of an ac grid. In this example, the PRBS is added to the modulating signal (m) generated by the inverter controller. Considering that the disturbance energy is sufficiently high, the voltages and currents of the system will be perturbed; each one will be composed by the steady-state component—represented in the figure with an overline ($\bar{i}_L$, $\bar{i}_{grid}$, $\bar{v}_{pcc}$)—and by a disturbed component ($\tilde{i}_L$, $\tilde{i}_{grid}$, $\tilde{v}_{pcc}$). Once the grid current and the PCC voltage are excited by the PRBS, the grid impedance can be calculated by relating the respective disturbed components $\tilde{i}_{grid}$ and $\tilde{v}_{pcc}$. The next section discusses how the cross-correlation method can be used to do so, and explains the details behind the data processing involved.

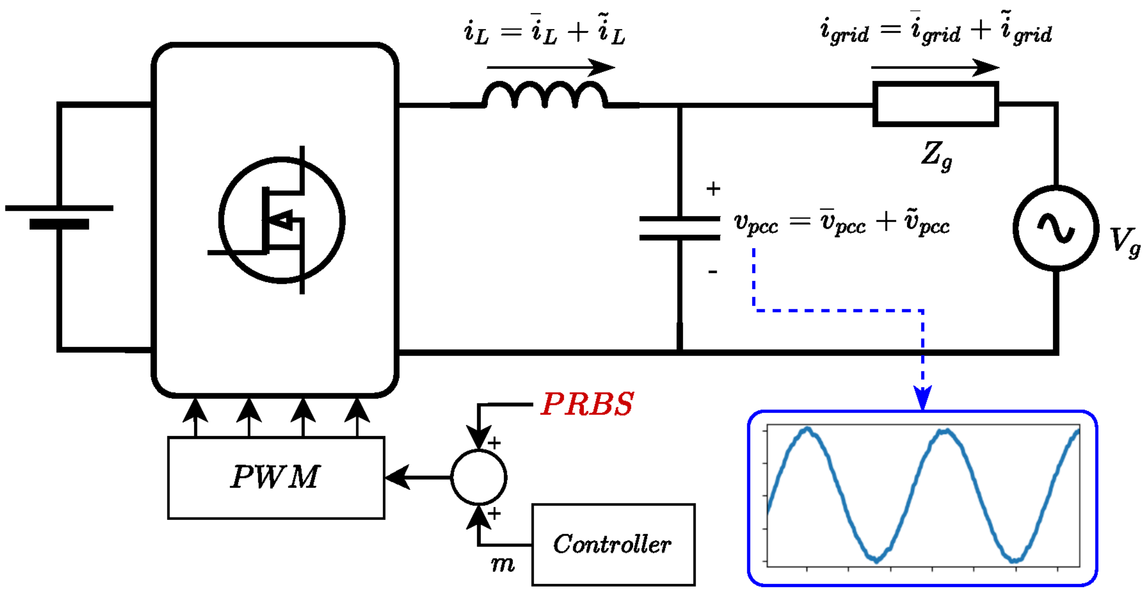

Figure 3.4 – Example of disturbance injection for grid impedance measurement.

3.4 Post-Treatment Methods

The post-treatment regards the data processing that is necessary to obtain the desired frequency response from the sampled input and output data. It becomes a challenging aspect of the identification if one recalls that the exciting signal—in our case, the PRBS—will be superposed to a steady-state component that is already part of the operating point of the system, as discussed in the previous section. In dc networks, the treatment is less complicated for the fact that the operating point is either constant or varies very slowly within an identification window; thus, separating the disturbed components from the steady-state ones is straightforward. In ac networks, however, the operation point is usually composed by alternate signals at 50 Hz or 60 Hz plus harmonics. Therefore, applying the CCM in such a system implies injecting the PRBS over these signals, which add some difficulties and makes the post-treatment more complex (MARTIN *et al.*, 2013). Since the amplitude of the PRBS must be several times smaller than that of the steady-state signal, the disturbed component at the output of the system has to be isolated before applying the CCM.

In three-phase systems, the ac-component problem can be bypassed if the control scheme is implemented in the dq reference frame. In this case, the PRBS can be injected in the direct frame, for instance, and the direct components of the currents and voltages can be used in the identification. Aside from eventual harmonic content or PLL dynamics, the disturbed components will be superposed to a constant value, which is easier to deal with. For single-phase systems, however, using the dq domain is not straightforward; although possible, more complex calculations are introduced (SILVA *et al.*, 2004; RICCOBONO *et al.*, 2016), which may affect the quality of the identified frequency response.

In this work, a single-phase ac system is considered, and both the controller and the disturbance injection will be performed in the sinusoidal domain. Two post-treatment methods are proposed and will be examined in the following.

3.4.1 Time-Alignment Method

The time-alignment method solves the problem of separating the output disturbed component by acquiring the output prior to the PRBS injection and using this information to subtract from the total, disturbed signal. In other words, if the output y is equal to $\overline{y} + \tilde{y}$ during the PRBS injection, the disturbed component $\tilde{y}$ can be obtained by subtracting the output that was sampled before the injection ($y_{prev} \approx \overline{y}$) from the total signal y. Thus, this method requires the previous state of the system to be known.

Figure 3.5 illustrates the method. First, the previous state of the system (y_{prev}) is acquired immediately before the start of the PRBS injection. During the injection, the output y of interest and the input u—which is necessarily the PRBS in this case—are sampled. y must be sampled at least at the generation frequency f_0. The PRBS, in theory, would not need to be sampled, since it is a well-known, deterministic signal that could be digitally reconstructed. However, the phase of the PRBS with respect to the sampled

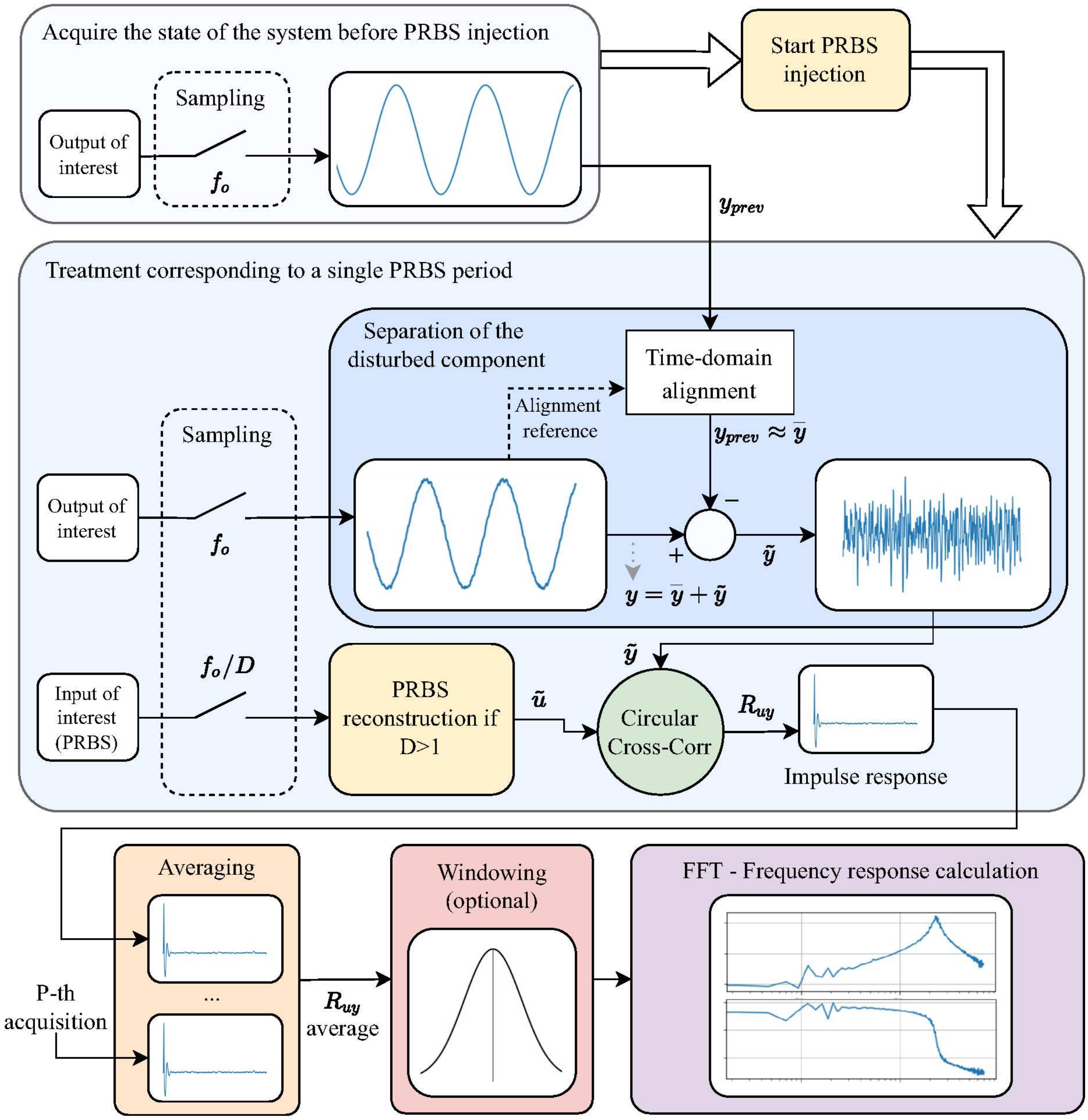

Figure 3.5 – Post-treatment steps for the time-alignment method.

output has to be known for the fact that each sample of the PRBS has to precisely correspond to a specific sample of the output. The simplest solution is to simultaneously sample the PRBS so the synchronism with the output is ensured. Nevertheless, a less memory-consuming alternative is possible due to a property of the PRBS that states that the sequence can be reconstructed, with no ambiguity, from a reduced set of, at least, N samples (being N the number of bits of the shift register). Hence, the synchronism can be ensured even if the PRBS is sampled at a lower rate; that is why a decimation factor D appears in Figure 3.5.

Once y is acquired, the disturbed component has to be isolated. As explained, it is done through a time domain subtraction; therefore, the samples corresponding to the previous state, y_{prev}, have to be aligned with respect to the fundamental component of

y. This is necessary since the PRBS length (M) is usually not a multiple of the number of samples within a fundamental period, so y_{prev} is not inherently aligned with y. The alignment is done by finding the phase shift in y_{prev} that minimizes the quadratic error between y_{prev} and y. Note that the number of fundamental periods acquired before the PRBS injection does not need to be the same as for the signal y. Actually, this number is a design choice. If the user opts for acquiring only one fundamental period, the samples can be replicated in order to generate a M-length signal, which is the approach utilized in this work.

After subtraction, the disturbed component $\tilde{y}$ is finally isolated and is ready to be cross-correlated with the PRBS. As shown in (ROINILA *et al.*, 2009), it is better to use the circular version of the cross-correlation instead of the classical one, which pads the signals with zeros, in order to eliminate imperfections in the results. After this operation, R_{uy} is obtained, which is the impulse response relating the selected output to the PRBS. The procedure until here is executed for the data-set corresponding to a single period of the PRBS. If P periods are used, the P impulse responses obtained can be vertically averaged—improving the SNR of the identification—so an average response $R_{uy,avg}$ is obtained. Optionally, this response can undergo a windowing process, through which, in the time domain, $R_{uy,avg}$ is multiplied by a Gaussian window of certain width. The windowing improves the identification results at high-frequencies (BARKLEY; SANTI, 2009), yet it may introduce undesired effects, such as the damping of eventual resonances. Hence, the recommended use of this tool depends on the application. The last step of the treatment consists of applying the FFT to the processed impulse response in order to get the frequency response of the system.

It is worthy pointing out that the process herein discussed allows to identify the transfer function $H(j\omega)$ relating the input $U(j\omega) = \{PRBS\}$ with the output $Y(j\omega)$. Nevertheless, if one must identify the frequency response between two other arbitrary signals, namely W and X, the time-alignment method can be employed in a two-step fashion—first, the relation between W and the PRBS (U) is obtained, then the same is done for X. From the division of the two transfer functions, the final response that relates W and X is derived, as follows

$$\frac{W(j\omega)}{X(j\omega)} = \frac{W(j\omega)/U(j\omega)}{X(j\omega)/U(j\omega)}. \tag{3.6}$$

This is particularly useful for the impedance identification using PECs. In this case, the PRBS is injected in the controller and what is sought is not the relation between one output and the PRBS, but the relation between the voltage and the current at the PCC. Hence, the Time-Alignment method can be applied first considering the voltage as the output, and then considering the current. The impedance is finally calculated by dividing

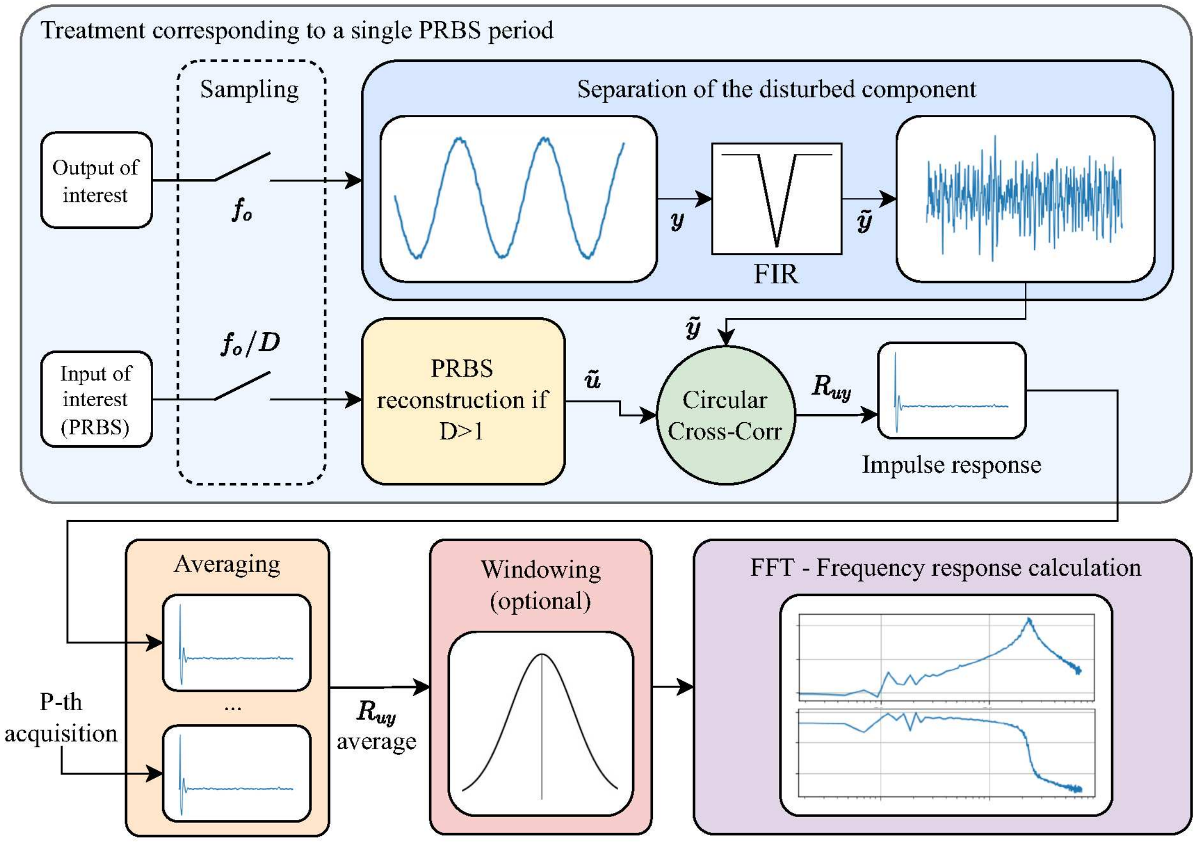

Figure 3.6 – Post-treatment steps for the FIR method.

the results. Note that, although the data treatment is performed sequentially, the voltage and the current should be simultaneously sampled in order to ensure a single point of operation for both treatment steps.

3.4.2 FIR Method

The FIR method, shown in Figure 3.6 essentially follows the same basis of the Time-Alignment method, diverging only on how the output disturbed component is isolated. Instead of using the previous state of the system, this method filters out the steady-state component using a finite impulse response (FIR) notch-filter tuned to the fundamental frequency (and harmonics if needed). The choice for the FIR filter is motivated by the fact that it does not introduce any kind of distortion to the signal; due to its linear-phase characteristics, it will only delay the signal as a whole. This effect, however, as well as the transient due to initialization, can be easily compensated within the data-processing. The design of the FIR filter is described in the following.

Finite impulse response (FIR) filters are characterized by the absence of feedback of the output signal, i.e. the output is constructed only as a linear combination of the input and its delayed versions. The transfer function of a FIR is given by

$$H(z) = \frac{Y(z)}{X(z)} = \sum_{k=0}^{L} b_k z^{-k}, \tag{3.7}$$

where the coefficients b_k and the order $n = L - 1$ of the filter are design variables.

In this post-treatment method, the filter is used to eliminate the fundamental and the harmonic frequencies of the output steady-state component. The "notch" behavior can be accomplished through the operations shown in the diagram in Figure 3.7.

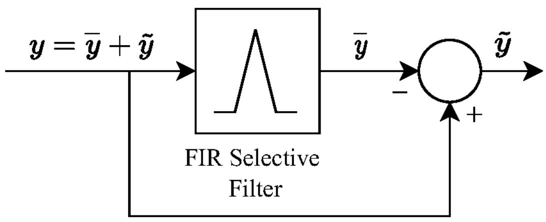

Figure 3.7 – Steady-state component suppression using a FIR filter.

Therefore, the filter to be designed is actually a selective filter. As demonstrated in (SIMÕES; FARRET, 2016), the FIR filter coefficients can be calculated based on the fundamental component of the Discrete Fourier Series in its cosine form, given by

$$y(k) = \frac{2}{N} \sum_{j=0}^{N-1} x(k-j) \cdot cos\left(\frac{2\pi}{N} j\right), \tag{3.8}$$

where N is the number of samples in a fundamental cycle. The coefficients of the filter can be calculated as shown in the code snippet below, written in Python.

```python

import numpy as np

def fir_filter(samp_freq: float,
               fund_freq: float,
               harmonics: list) -> list:
'''
Parameters
----------
samp_freq : float
    Signal's sampling frequency.
fund_freq : float
    Fundamental frequency.
harmonics : list
    List of harmonics to be suppressed.

Returns
-------
```

```
    list
        FIR filter coefficients.
    '''
    num_samples = int(samp_freq/fund_freq)

    fir = [0] * num_samples
    for harm in harmonics:
        for idx, coef in enumerate(fir):
            fir[idx] = fir[idx] + 2/num_samples * np.cos(harm*idx/num_samples*2*np.pi)

    return fir
```

Listing 3.1 – Code for FIR coefficients calculation.

Compared to the Time-Alignment method, this method simplifies the post-treatment since it does not require the output to be sampled before the PRBS injection begins; however, any information contained in the frequencies rejected by the FIR filter will be lost. Other advantages or disadvantages of the methods will be discussed later.

3.5 Data Acquisition Hardware Topology

This section describes the hardware topology that is used in all identification experiments performed in this work. The PECs used for experimental validations utilize a Texas Instruments® F28335 for the controller, which is a broadly used Digital Signal Processor (DSP) in power electronics applications. The F28335, however, is not performing enough to run the identification post-treatment. To do so, a BeagleBone Black (BBB) board can be used, following the topology depicted in Figure 3.8. The data sampled via F28335 is sent to the BBB board through an asynchronous serial communication—the UART (Universal Asynchronous Receiver/Transmitter). Once the data is received by the BBB, it can either undergo the post-treatment in the BBB itself, or be transferred to another platform in which the post-treatment is executed. This communication system[1] allows the BBB to write to and read variables from the F28335, as required for the impedance identification. In the beginning of the identifications process, the BBB send a command to the F28335 to start the PRBS injection. At the same time, the sampled signals are asynchronously sent to the BBB through a buffer of the F28335. At the end of the acquisition, the data is available in the BBB to be processed. This communication and data-processing topology also enables for applications in which the information of the

[1] The communication system was developed in the context of another project by PhD Hildo Guillardi Júnior and PhD Joel Filipe Guerreiro.

identification is used to act over the PEC's controller. These adaptive control techniques will be explored in future work.

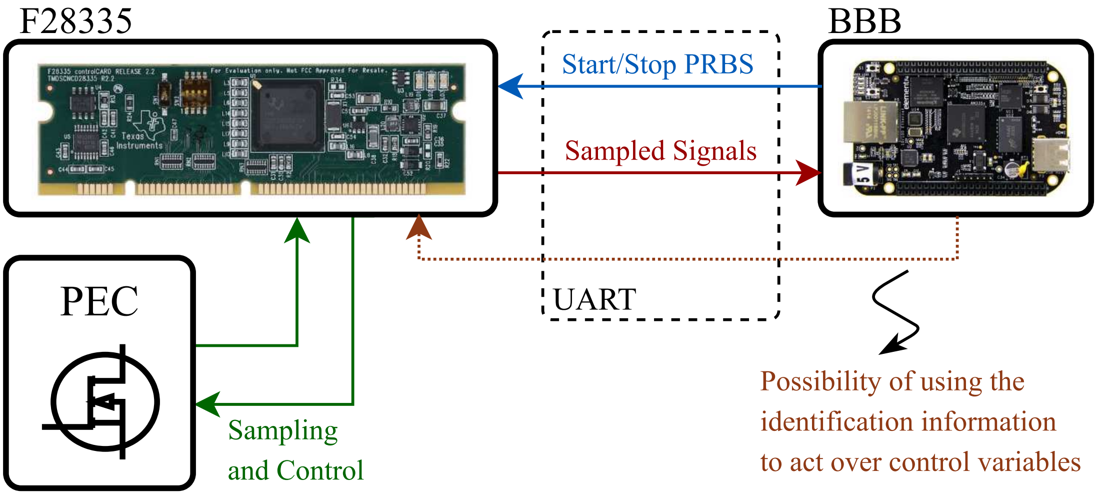

Figure 3.8 – Communication topology for data acquisition.

Although the hardware configuration in this work is composed by a high-level processor in addition to the DSP, it might represent a cost constraint for practical applications. It is worthy pointing out, however, that the used DSP is not the most powerful one in the market. Cutting-edge DSPs may be capable of handling both control and identification routines.

3.6 Case Study: Impedance Identification Using an Active Rectifier

This section presents a case study with the goal of analyzing and comparing the proposed methods. These are preliminary results concerning the identification technique only, which will be useful for a better understanding of the identification outcome when applied to the stability analysis in Chapter 6. In this case study, a PEC operating in the grid-following mode as an Active Front Rectifier (AFR) is utilized to identify a test impedance. Such converter is capable of draining power from the grid with high power factor, as detailed in the following. Both simulation and experimental results will be discussed.

3.6.1 System Description

Figure 3.9 presents a simplified scheme of the system considered in this case study. The AFR is connected to a single-phase grid through a LCL filter in cascade with a test impedance (Z_{test})—composed by a 1 µF capacitor and a 1.5 mH inductor—, whose frequency response is to be identified in this case study. In the experimental setup, a programmable voltage source is used to represent the ac grid.

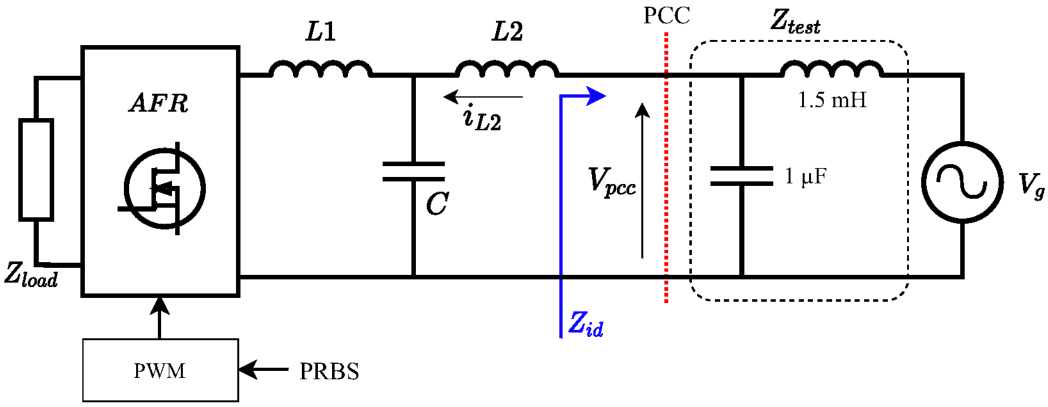

Figure 3.9 – System description for impedance identification using an AFR.

The AFR output current (i_{L2}) is regulated via a proportional-resonant (PR) controller that is capable of compensating odd harmonics up to the 9^{th} order. Thus, within the control limitations, the current drained from the grid is sinusoidal, presenting a satisfactory power factor. It is worth commenting that the AFR was not designed in this project—more details on its hardware and controller can be found in (GUERREIRO, 2020; GUERREIRO *et al.*, 2021; GUERREIRO *et al.*, 2019), and its main parameters are listed in Table 3.1.

Table 3.1 – AFR parameters

AFR	
Power rating	1 kVA
Dc-link voltage	225 V
Switching frequency	24 kHz
Ac voltage (rms)	127 V
Ac voltage frequency	60 Hz
LCL Filter	
Inductance $L1$	1 mH
Inductance $L2$	300 µH
Capacitance C	5 µF
Control System	
Current loop bandwidth	1.2 kHz
Current loop phase margin	60°

In order to excite the system, a PRBS is injected into the PWM. As explained, if the amplitude of the disturbance is properly chosen, the currents and voltages of the system will be excited in a wide range of frequencies, determined by the PRBS spectral content. The generation frequency of the binary sequence is set equal to the AFR switching frequency (24 kHz), which establishes the upper identification limit of 12 kHz. A 10-bit register is used to generate the PRBS, resulting in a sequence length (M) of 1023 values. Therefore, the expected spectral resolution is approximately 23.46 Hz. The amplitude of the PRBS is selected as 3% of the modulator range. Provided that the dc-link voltage is kept at 225 V, this value corresponds to a perturbation of approximately 6.75 V in the switched voltage generated at the inverter bridge of the AFR. As will be shown in the following, this amplitude is sufficient to excite the system above noise levels for a satisfactorily range of frequencies. All the PRBS parameters are listed in Table 3.2.

Table 3.2 – PRBS parameters for the identification of Z_{test}

Generation frequency (f_0)	24 kHz
Number of bits (N)	10
Sequence length (M)	1023
Number of periods/acquisitions (P)	8
Amplitude (e)	3% (with respect to the modulator)

For each identification to be performed, eight periods of the PRBS are utilized in order to apply the averaging process explained in section 3.4, improving the SNR. In each acquisition, three signals are simultaneously sampled in synchronism with the PWM—the current through $L2$ (i_{L2}), the PCC voltage (V_{pcc}), and the PRBS. The current and the voltage are sampled at 24 kHz whereas the PRBS is sampled at a rate one hundred times slower. By doing so, in a single acquisition, corresponding to a whole PRBS period of 1023 values, at least ten PRBS values are acquired, which enables the reconstruction of the sequence with no ambiguity during the post-treatment phase, saving memory.

Concerning the duration of the injection, one 10-bit PRBS period is 42.6 ms long for $f_0 = 24$ kHz. Thus, the total experiment duration, including all 8 acquisitions, is only 341 ms, or 20.46 cycles of the grid voltage.

The impedance establishing a relation between V_{pcc} and i_{L2} is represented in Figure 3.9 by Z_{id}, which readily corresponds to the test impedance (Z_{test}) to be identified.

3.6.2 Simulation Results

The system is simulated using PSIM, and both Time-Alignment and FIR methods are employed using the same data-set. Figure 3.10 presents V_{pcc} and i_{L2} before and after the beginning of the PRBS injection for the AFR operating at approximately 25% of the rated power. At instant 0.5 s, the PRBS is turned on, and the PCC voltage and cur-

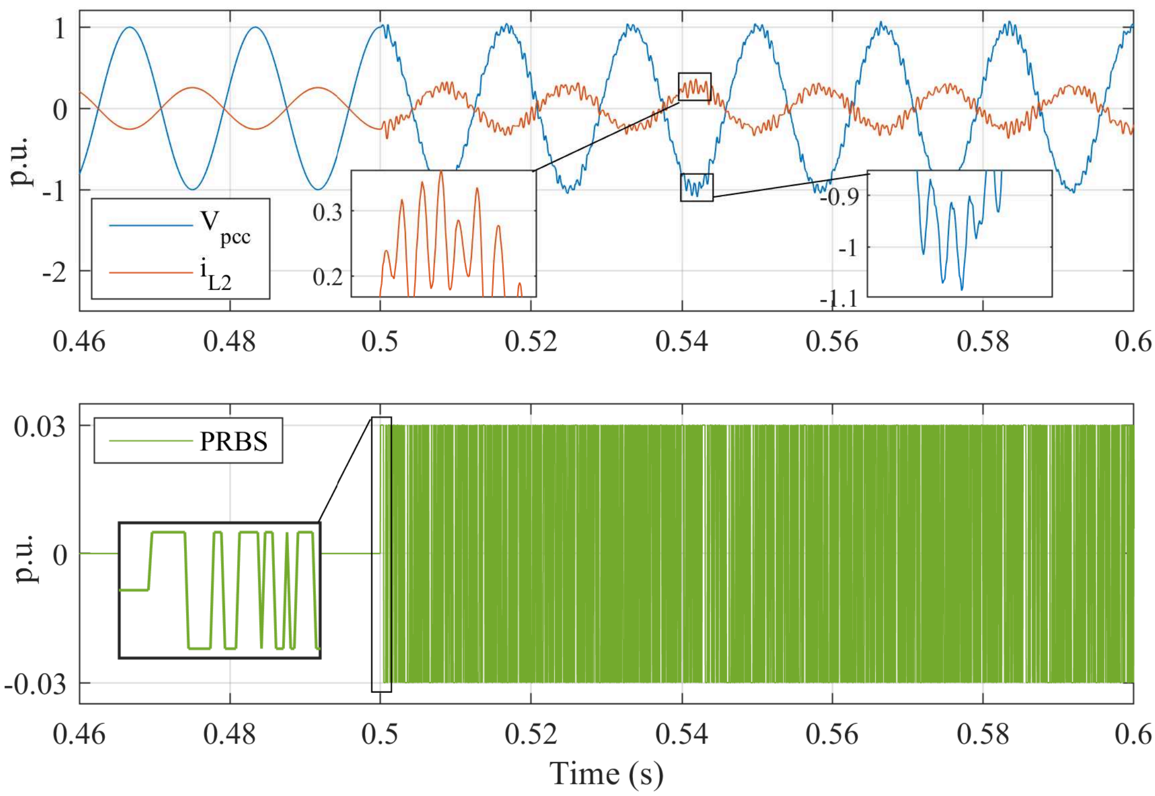

Figure 3.10 – PCC voltage (V_{pcc}), current through $L2$ (i_{L2}), and the PRBS signal from PSIM simulation. At instant 0.5 s, the PRBS is turned on.

rent do become disturbed. Note that, despite the fact that the perturbation level reaches almost 0.2 p.u for both current and voltage, the inverter manages to keep the point of operation around the 60 Hz current reference.

Some details on the post-treatment steps are given in Figures 3.11 and 3.13 for the Time-Alignment and the FIR methods, respectively. As discussed before, in order to obtain the impedance, the post-treatment needs to be performed in a two-step manner—one for finding the transfer function between the voltage and the PRBS point of injection, and the other for the current. For the sake of clarity, only the waveforms corresponding to the voltage post-treatment will be shown in this section.

Starting with the Time-Alignment method, Figure 3.11a shows the sampled output before (y_{prev}) and during (y) the PRBS injection. Whereas the number of samples of y is equal to the length of a single PRBS period, 1023, only 400 samples are acquired for y_{prev}, which corresponds to a single fundamental period of the grid voltage. This set of samples for y_{prev} will be used to remove the steady-state component ($\overline{y}$) from y for all 8 acquisitions. Since one PRBS period comprises more than one grid fundamental cycle, y_{prev} has to be extended, as shown in Figure 3.11b. This is done by sequentially repeating the signal as many times as needed. The next step consists of finding the phase shift that

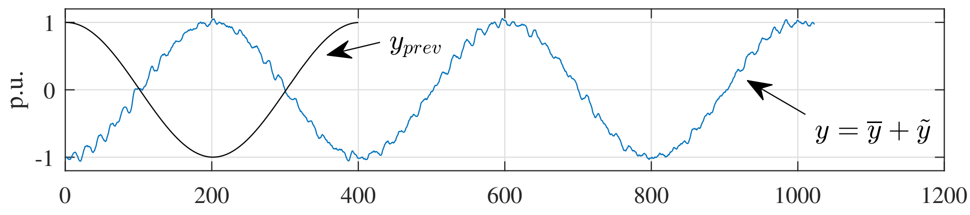

(a)

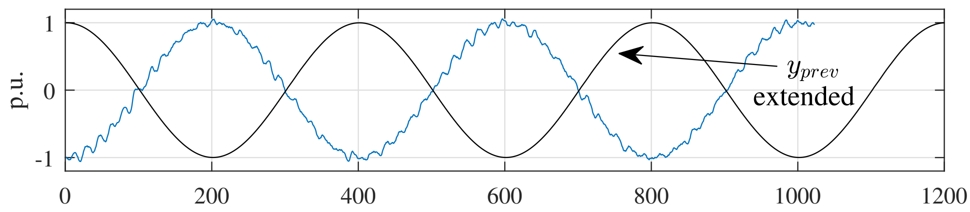

(b)

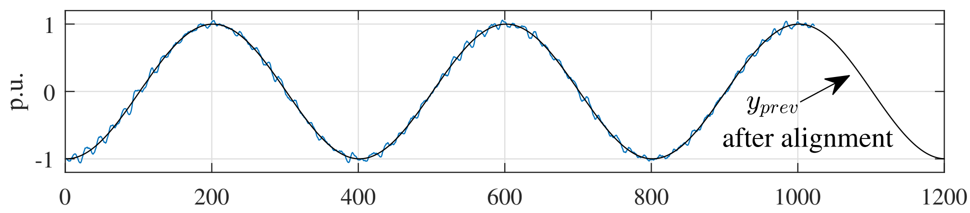

(c)

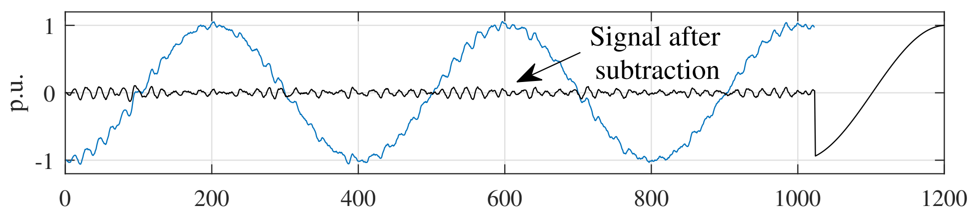

(d)

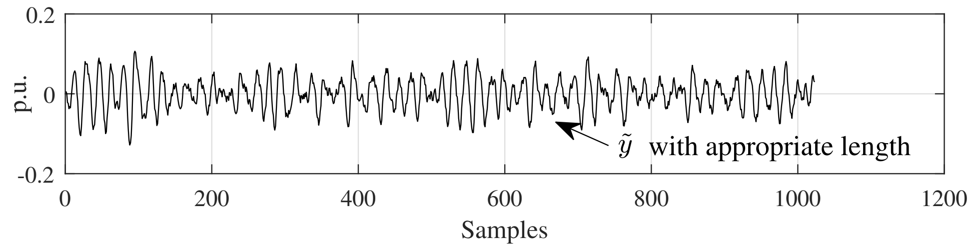

(e)

Figure 3.11 – Details on the Time-Alignment method for a single PRBS period with $y = V_{pcc}$. (a) Disturbed output (y) and output prior to the PRBS injection (y_{prev}), (b) y_{prev} is extended to cover the PRBS length, (c) y_{prev} is aligned with respect to y, (d) Subtraction of y_{prev} from y, and (e) Disturbed component ($\tilde{y}$) is obtained at the end of the process.

minimizes the quadratic error between y_{prev} and y in order to get both signals aligned (see Figure 3.11c). Once the signals are properly aligned, y_{prev} can be subtracted from y (Figure 3.11d) to obtain the disturbed component of the output ($\tilde{y}$). In the last step, the result of the subtraction is clipped to the appropriate length (1023) at one end, ignoring the spurious data due to the extension of y_{prev}. It is worthy emphasizing that this process is repeated for each period P used.

The signal presented in Figure 3.11e is the system's response to the PRBS only, with the influence of the steady-state point of operation suppressed. By cross-correlating it with the PRBS, the system's impulse response can be obtained. The auto-correlation of the PRBS, and the cross-correlation between $\tilde{y}$ and the PRBS are shown in Figures 3.12a and 3.12b, respectively. Remark that, as expected by the theoretical formulation, the auto-correlation is an impulse at the origin of magnitude $e^2 = (0.03)^2 = 0.0009$ followed by a constant value of $-e^2/M = -8.798 \cdot 10^{-7}$, while the cross-correlation is the response of the system to this impulse. By applying the FFT to the impulse response, the frequency response can be obtained.

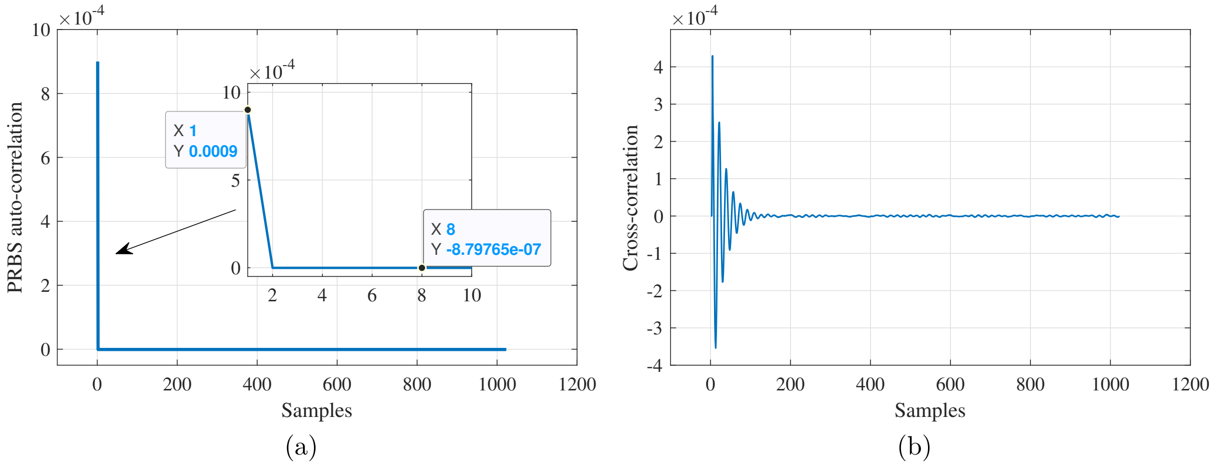

Figure 3.12 – (a) PRBS auto-correlation function and (b) cross-correlation between $\tilde{y}$ and the PRBS.

Before presenting the final identification result, the steps of the FIR method will be analyzed. For the following results, the filter is tuned to the fundamental frequency only (unless otherwise mentioned). As any digital filter depending on previous values of the input, the FIR filter exhibit an initial transient while not enough samples are fed in. This is shown in Figure 3.13a, in which both y and its filtered version are depicted. If this transient is not discarded before extracting the disturbed component, the identification will be compromised. The data-set of y can be extended by one (or more) fundamental periods so the transient can be discarded, as shown in Figure 3.13b. After subtracting both signals, and clipping the result to the appropriate length, the disturbed component is obtained (see Figure 3.13c). As for the Time-Alignment method, this signal is then cross-correlated with the PRBS to get the system's impulse response.

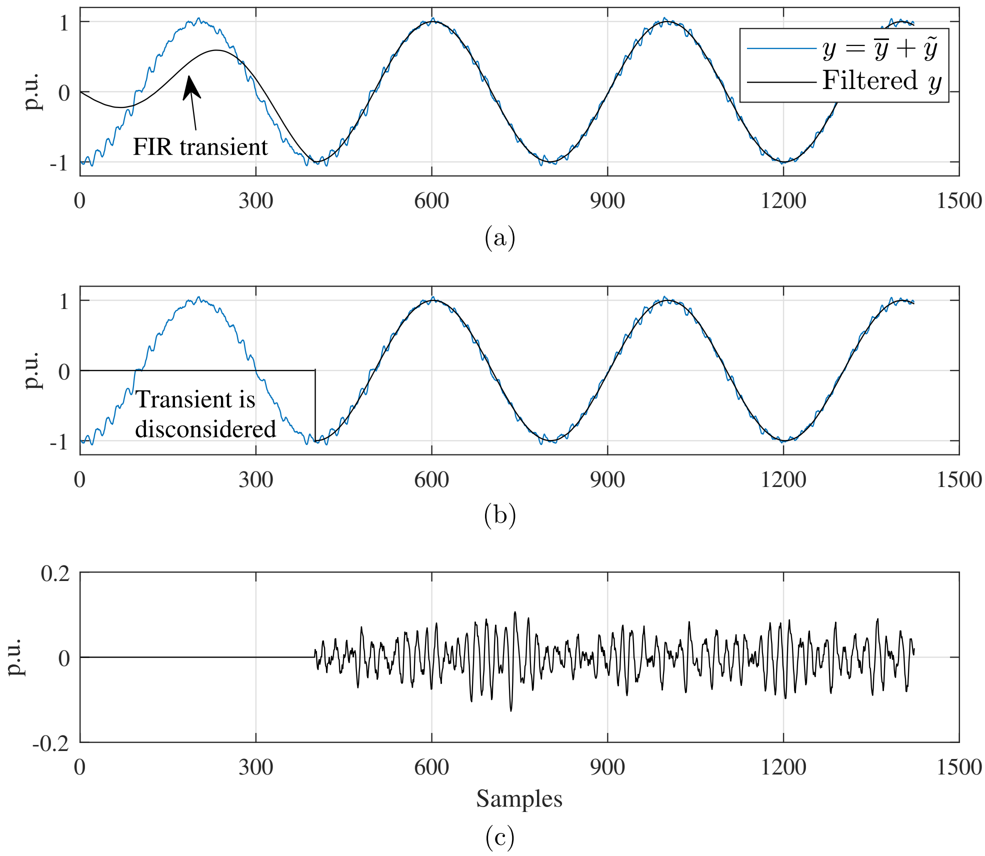

Figure 3.13 – Details on the FIR method for a single PRBS period with $y = V_{pcc}$. (a) Disturbed output (y) and its filtered version, (b) FIR filter transient is neglected, and (c) disturbed component ($\tilde{y}$) is obtained at the end of the process.

Figure 3.14 presents the frequency response of Z_{id} obtained via both post-treatment methods and through the analytical model. The impedance is inductive at low frequencies, as expected due to the 1.5 mH inductor. A resonance appears at approximately 4 kHz as a result of the 1 µF capacitor. On the whole, both methods match well the expected result for the magnitude and the phase. The most noticeable difference occurs around the fundamental frequency of the signals, 60 Hz—while the FIR method managed to completely suppress the influence of the steady-state component ($\overline{y}$), the Time-Alignment method could not eliminate all its vestiges. In the next section, these results will be compared with the experimental ones.

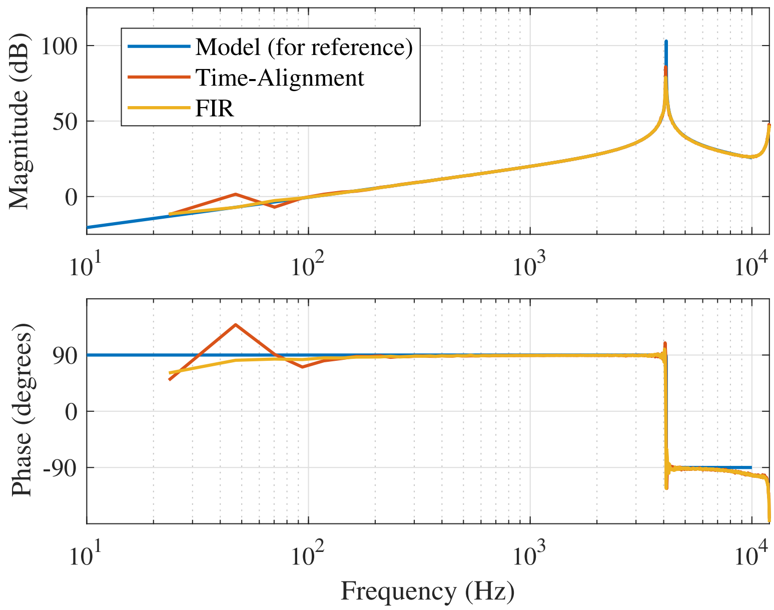

Figure 3.14 – Z_{id} identification result using PSIM for the Time-Alignment method (in orange) and the FIR method (in yellow), and the expected model result (in blue).

3.6.3 Experimental Results

The voltage at the PCC and the current through the inductor $L2$ during the PRBS injection are shown in Figure 3.15. Despite the disturbance, the AFR controller keeps the operating point. Comparing with the simulation waveforms (Figure 3.10), both voltage and current are less affected by the disturbance in the experimental setup, even though the same PRBS amplitude is used.

The Z_{id} frequency response obtained experimentally is presented in Figure 3.16, in which both post-treatment methods are compared with the expected result. Note that, differently from the simulation results, a more significant mismatch between the identification and the analytical model is observed, specially in the impedance phase for higher frequencies. Both Time-Alignment and FIR methods present a great response for the magnitude identification, specially for frequencies ranging from 100 Hz to 4 kHz, where the resonance can be identified. At low frequencies, the FIR method exhibit a better performance than the Time-Alignment one—the magnitude and the phase points of the latter are more dispersed and present a higher deviation from the expected result.

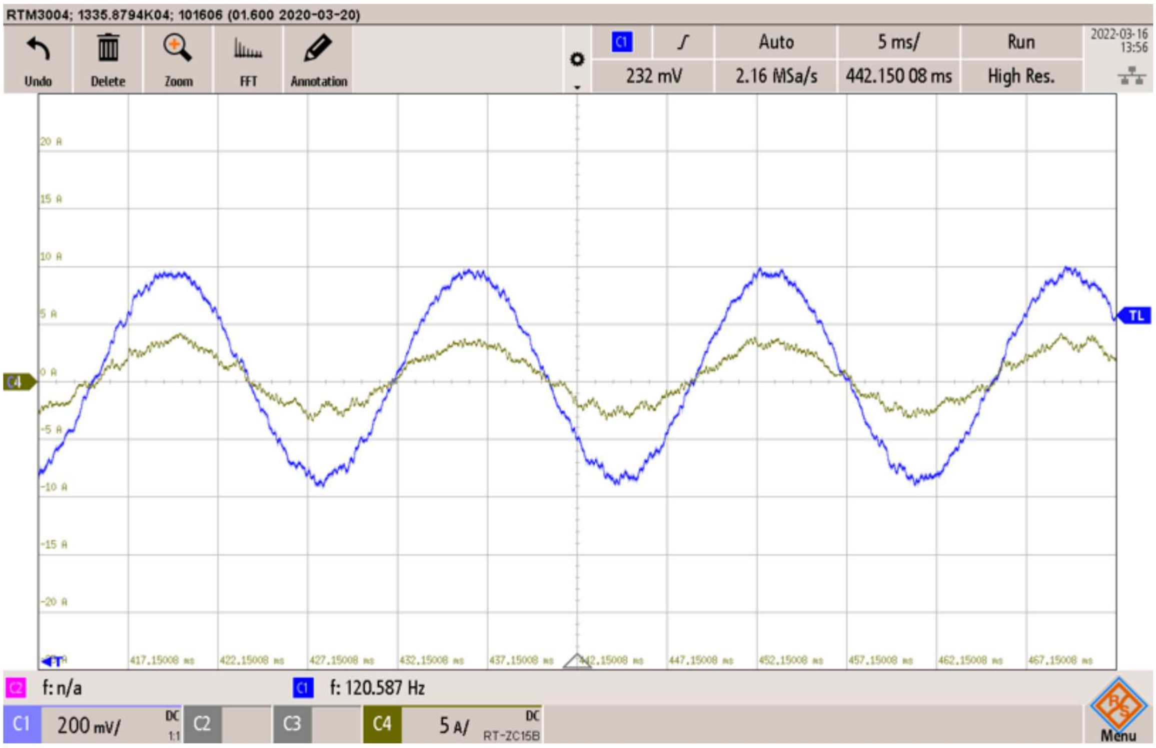

Figure 3.15 – PCC voltage (in blue) and current through $L2$ (in yellow) during the PRBS injection. The voltage was measured with a 1:500 probe, so 1 mV in the figure corresponds to 0.5 V in the experimental setup.

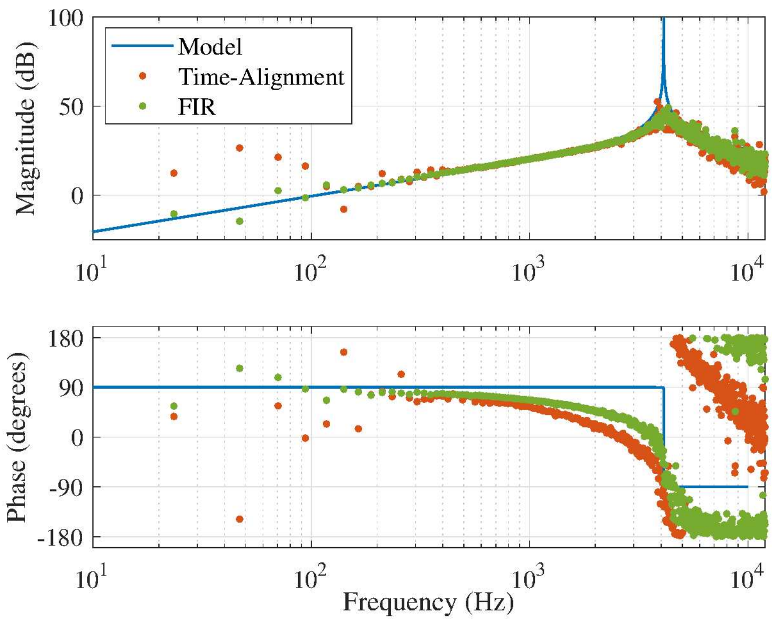

Figure 3.16 – Experimental Z_{id} identification result for the Time-Alignment method (in orange) and the FIR method (in green), and the expected model result (in blue).

Concerning the phase, both methods diverge from the model for high frequencies, specially above the resonant frequency. Nevertheless, the phase response obtained via

FIR method correlates better with the expected result—whereas the Time-Alignment's phase keeps a negative slope after crossing 180°, the FIR method's phase levels off around 180°. This high-frequency error is expected since the PRBS spectrum has less power when compared with lower frequencies. Also, it is important to have in mind that some unmodeled effect may be present in the experimental setup, contributing to the divergence between the identification and the expected results.

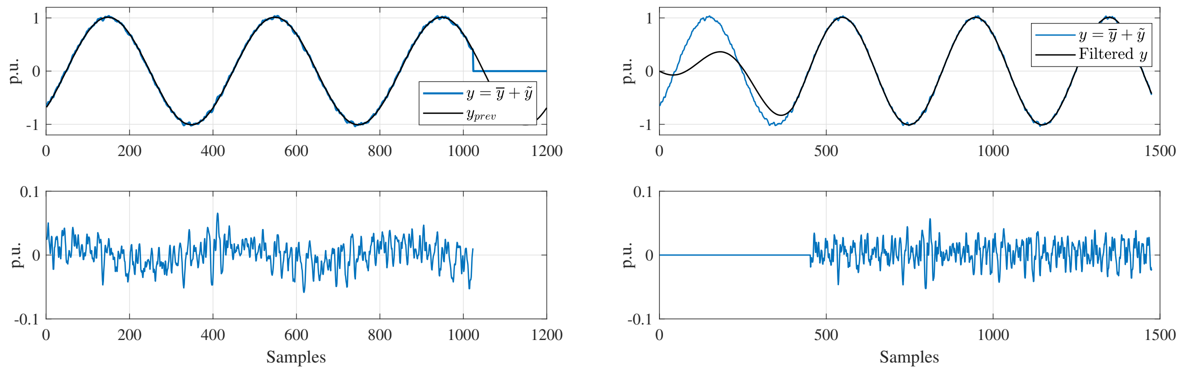

(a) (b)

Figure 3.17 – Example of disturbed component isolation using the experimental data for (a) the Time-Alignment method and (b) the FIR method.

The low-frequency error—which is more pronounced in the Time-Alignment method—can be better understood by looking at Figure 3.17, in which an example of the output disturbed component obtained through both methods is presented. For the Time-Alignment method shown in Figure 3.17a, observe that a 60 Hz component is still present in the isolated disturbance although y and y_{prev} seem to be well aligned in time. The FIR method, however, manages to better suppress the steady-state component, as shown in Figure 3.17b. Note that this residual 60 Hz component does impact on the identified impulse response, as can be seen in Figure 3.18, which presents the cross-correlation for both methods. For the FIR method (Figure 3.18b), the impulse response is less affected by the low frequency component compared to the Time-Alignment one (Figure 3.18a).

Another interesting effect that can be inferred from the impulse responses in Figure 3.18 is that the Time-Alignment method introduces a small delay when isolating the disturbed component. Note that the impulse response (Figure 3.18a) takes approximately 40 samples to start to grow. This delay would explain the high-frequency phase shift in Z_{id} obtained through this method.

In the simulation, no measurement noise was modeled, thus using one or all eight PRBS periods would lead to the same result. In the experimental setup, however, noise is inherently present. A comparison between using only a single PRBS period ($P = 1$) and eight periods ($P = 8$) in the post-treatment is shown in Figure 3.19 for both

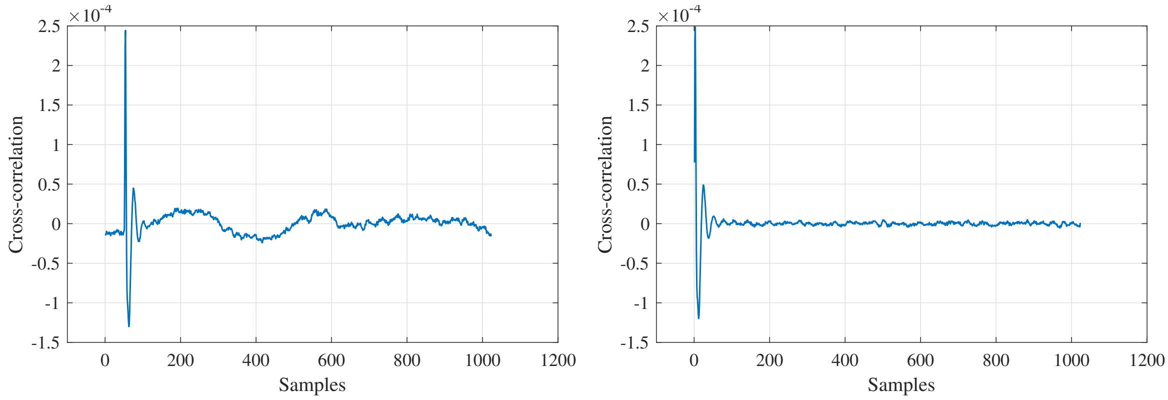

(a) (b)

Figure 3.18 – Cross-correlation between $\tilde{y}$ and the PRBS for (a) the Time-Alignment method and (b) the FIR method obtained experimentally.

methods. In both cases, using more periods led to more accurate results not only at high-frequencies—where a lower SNR is expected—, but also for low-frequencies.

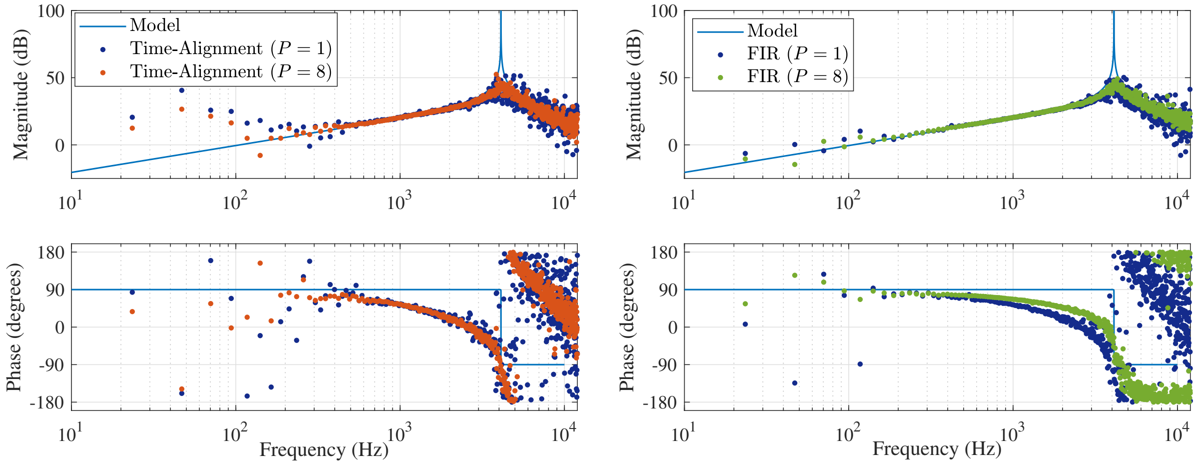

(a) (b)

Figure 3.19 – Comparison between the experimental Z_{id} identification using a single ($P = 1$) and eight ($P = 8$) PRBS periods for (a) the Time-Alignment method and (b) the FIR method.

3.6.3.1 Effect of Voltage and Current Distortion

In the previous tests, the voltages and currents in the system were sinusoidal. In order to evaluate the performance of the post-treatment methods under voltage and current distortions, a nonlinear load is connected in parallel with the test impedance at the PCC. The nonlinear load is a diode-bridge with LC filter at the dc side.

Figure 3.20a shows the PCC voltage, the current through $L2$, and the current drained by the nonlinear load prior to the PRBS injection. Note that the current drained by the AFR presents a low distortion level, maintaining the sinusoidal shape, due to the resonant controller action, which is capable of compensating odd harmonics up to the 9th order. This effect can be better understood by looking at the spectrum of i_{L2} presented in Figure 3.21. It can be seen that the current exhibits lower magnitude for the harmonic frequencies located up to the 9th order (540 Hz) whereas, for higher orders, the magnitude is more pronounced. The voltage, in turn, presents significant harmonic content even for the frequencies that are compensated by the controller. Indeed, since the AFR rejects these harmonics, they flow through the 1.5 mH inductor towards the grid, distorting the PCC voltage. For the harmonic components that are not rejected, the current flows through both the AFR and the grid.

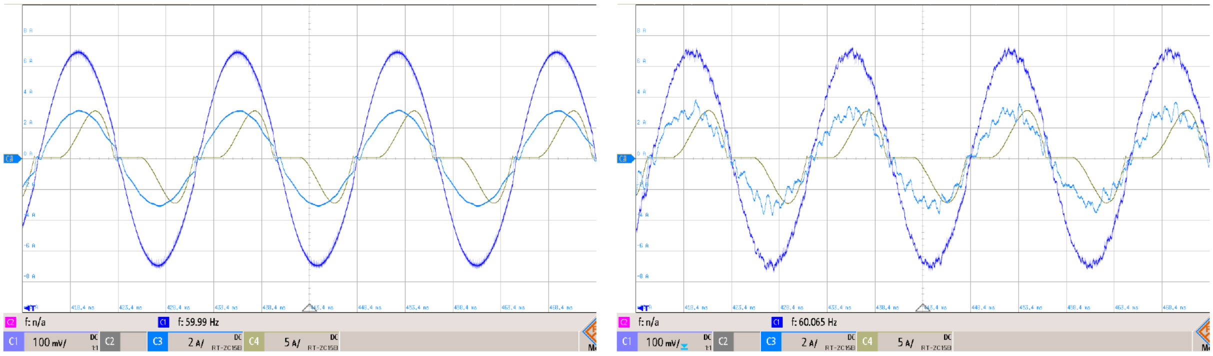

(a) (b)

Figure 3.20 – PCC voltage (in dark blue), current through $L2$ (in light blue), and current drained by the nonlinear load (in yellow) (a) prior to and (b) during the PRBS injection.

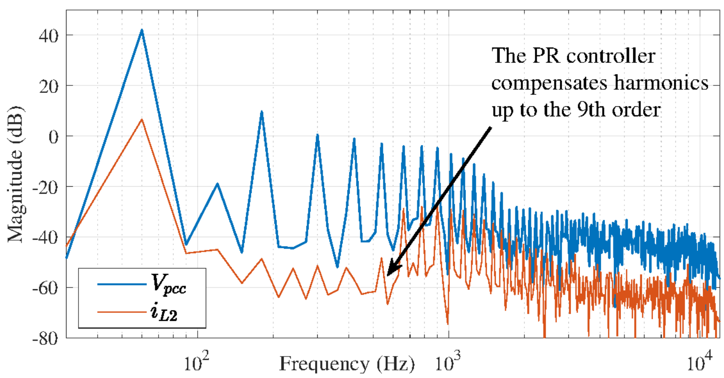

Figure 3.21 – V_{pcc} and i_{L2} spectrum before PRBS injection.

In this scenario, the identification is performed using the same PRBS parameters (see Table 3.2). The effect of the PRBS over the circuit is depicted in Figure 3.20b, in which the perturbed voltage and currents can be observed. The identification result is contrasted with the expected model in Figure 3.22 for three different post-treatment settings, using

- the Time-Alignment method,
- the FIR method with the FIR tuned only to the fundamental frequency (referred to as FIR_{fund}),
- and the FIR method with the FIR tuned to the fundamental frequency and to odd harmonics up to the 11th order (referred to as FIR_h).

Above 1 kHz, no effect due to the distortion is noticeable; up to this frequency, however, the identification is affected, as shown in detail in Figure 3.22b. Note that, for all three strategies, the harmonic content introduced magnitude and phase deviations. The Time-Alignment method exhibited better distortion immunity when compared with the FIR_{fund} result, specially for the phase and for the magnitude in the harmonic range. It is interesting to notice that, even around the fundamental frequency, the FIR_{fund} did not manage to accurately identify the impedance. Indeed, the harmonic distortion—if not correctly eliminated from the voltage and the current—worsens the frequency leakage effect. The leakage occurs whenever the FFT is applied to a non-integer number of periods of the signal. This effect is already present even with no harmonic distortion, since the 1023-sample PRBS does not correspond to an integer number of fundamental periods. When harmonics exist, however, the PRBS number of samples does not match any of the respective harmonic periods, which aggravates the leakage, compromising the identification accuracy.

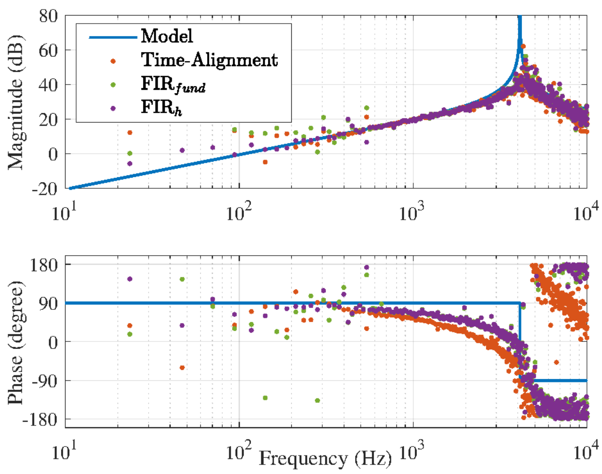

(a)

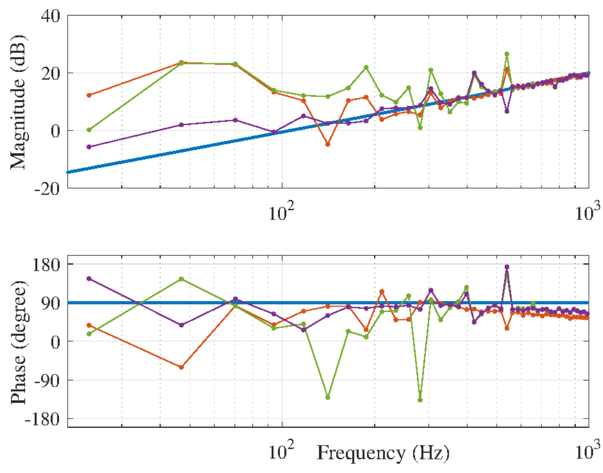

(b) Detail

Figure 3.22 – Identification results for the nonlinear load case considering three post-treatment methods (Time-Alignment, FIR, and FIR with harmonic compensation). Details between 20 Hz and 1 kHz are shown in (b).

By including some harmonics in the FIR filter, improved results were obtained. As shown in the FIR_h response in Figure 3.22b, a better magnitude and phase accuracy is achieved through this method, although some harmonic content is still present.

Figure 3.23 compares the identification performance in the nonlinear load scenario with the previous one, without the diode rectifier. The comparison for the Time-Alignment method is presented in Figure 3.23a. Roughly speaking, no considerable difference is noticed, which implies that the performance of this method is not critically affected by voltage and current distortions. This is due to the fact that the information of the system prior to the PRBS injection, used to suppress the steady-state component of the disturbed signals, comprises the harmonic frequencies. In Figure 3.23b, the FIR$_h$ method is contrasted with the scenario without nonlinear load. Note that both results are similar, which denotes that tuning the FIR to harmonic frequencies as well is important in the presence of distorting loads.

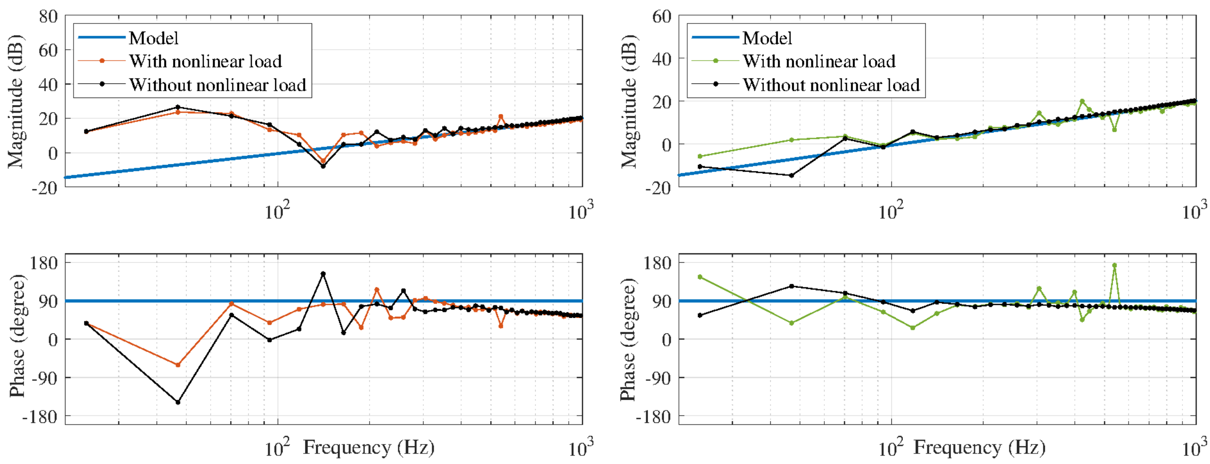

(a) Time-Alignment (b) FIR$_h$

Figure 3.23 – Comparison between the scenarios with and without the nonlinear load for (a) the Time-Alignment method and (b) the FIR method with harmonic compensation.

3.7 Partial Conclusions

For the tested scenarios, the FIR method provided better results. Even though both methods had a similar performance in simulation, the steady-state component attenuation and the high-frequency resolution were better achieved by the FIR method in the experiment.

In the Time-Alignment method, the previous output state, y_{prev}, is only an approximation of the steady-state component that it is intended to represent. In the simulation, the signals are well-behaved and the system's operating point does not arbitrarily vary from cycle to cycle; hence, y_{prev} manages to satisfactorily represent $\overline{y}$, which leads to a good identification result at low frequencies. In a real system, however, the point of operation may fluctuate from one fundamental cycle to another, which makes y_{prev} deviate from $\overline{y}$. If a voltage sag or swell occurs during the identification process, for instance, the resulted frequency response will be affected. Depending on the magnitude of the event, completely compromised. Moreover, the noise in y_{prev} also undermines the steady-state component suppression. As observed in Figure 3.17a, part of $\overline{y}$ remains in the disturbed component, $\tilde{y}$, leading to an accentuated low-frequency error in the identified impedance.

For the fact that the FIR method does not use the system's previous state to isolate the disturbed component, it is more resistant to voltage and current changes, as sags and swells, during the identification. As a consequence, it has outperformed the Time-Alignment method in the experiment. Nevertheless, it is important to point out the drawbacks of this method. First of all, the information in the filtered frequencies are lost. In the tested scenarios, for instance, if the impedance at 60 Hz, or at the filtered harmonics, were to be known, this method could not be employed. In some situations, this can be particularly detrimental—if the impedance of a converter regulated through resonant controllers is to be measured, for instance, filtering out the harmonic frequencies may not be interesting.

Another drawback concerns voltage and current distortions. Even though good results were obtained with the FIR_h version, if the FIR filter is not appropriately tuned to all harmonic frequencies to be suppressed, they may interfere in the identification response. Although the most prominent component is usually the fundamental one, in some cases, the harmonic components may have amplitudes as high as the PRBS'. If not properly eliminated, the identification accuracy is compromised, as observed in Figure 3.22. Therefore, in order to apply the FIR method, the distortion levels of the system must be known beforehand for tuning the filter.

The results presented in this section are crucial for a better understanding of the identification process when applied to more complex systems, as for the measurement of the impedance of another PEC, which will be presented in Chapter 5. Before that, however, the DB-GFI will be introduced in the next chapter.

4 Deadbeat-Controlled GFI

In this chapter, the deadbeat-controlled grid-forming inverter is introduced. The chapter starts by presenting the GFI topology and then the details on the deadbeat controller. At the end, experimental results are presented to evaluate the GFI performance in different scenarios.

4.1 GFI Topology

In this work, the GFI is a single-phase, full-bridge voltage-source inverter with LC output filter, as depicted in Figure 4.1. The dc-link voltage (V_{dc}) represents any energy storage system, as a battery or a fuel cell. As aforementioned, the role of the GFI is to maintain the ac-output voltage (v_o) with low distortion regardless of the load (Z_l) connected at its terminals. For doing so, the inverter should be able to produce a current i_L that ensures a sinusoidal current i_c through the capacitor (C), i.e. i_L should compensate all the distorting components that may be present in the load current (i_o).

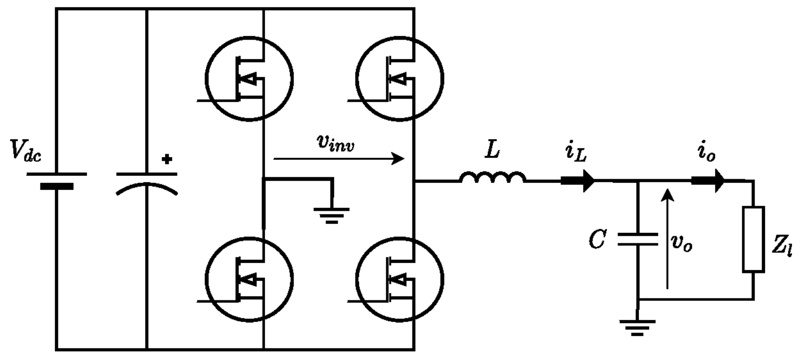

Figure 4.1 – Topology of a GFI with LC-output filter

Two-level SPWM is utilized, and the sampling is synchronized with the PWM so that the mean value of the inductor current (within a switching cycle) is directly sampled. The carrier wave is a symmetric, triangular signal having unitary amplitude. More details on the hardware used for the experimental tests will be given in section 4.4.

4.2 The Deadbeat Predictive Controller

Different schemes can be used to control an inverter in the grid-forming mode. Proportional, proportional-integral, resonant-proportional, repetitive, and deadbeat (DB) controllers are just some examples of control strategies managing to regulate the output voltage of an inverter. Besides, these controllers can be organized and associated in different forms, composing—for instance—cascaded or parallel control structures (LIU *et al.*, 2020), which increases even further the number of possibilities. In this work, the DB was selected not only due to its great dynamic performance, but also because it represents an interesting research object concerning its impedance model. Moreover, the DB stability is usually analyzed in the literature only in terms of parameter mismatches, and not via the IBSC, as will be done throughout this work.

A digital controller is said to exhibit a *deadbeat* behavior when the regulated signal is capable of reaching the reference value in a finite number of sampling periods. That is possible because the DB acts allocating all the poles of the system at the origin so that the closed-loop transfer function is—ideally—composed only by sample delays. Some authors refer to the DB as a *predictive* controller since its operating principle consists of using the dynamic equations describing the system to obtain the control laws (BUSO; MATTAVELLI, 2006).

In this work, the DB controller is implemented in a nested, two-loop structure, similar to the one presented in (BUSO *et al.*, 2001), as depicted in Figure 4.2. The inner loop regulates the current i_L through the LC-filter inductor and the outer one regulates the output voltage v_o. Also, capacitor-current feedforward is utilized in the voltage loop in order to improve controller's performance. The details are explained hereinafter.

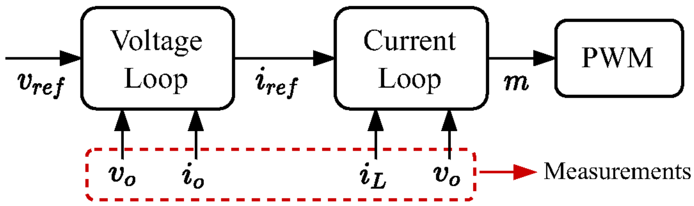

Figure 4.2 – Simplified controller topology.

4.2.1 Current Loop

The objective of the inner loop is to determine the voltage that the inverter has to produce in order for the inductor current to reach its reference value in a predetermined number of sampling periods. In other words, the current loop is responsible for calculating the value of the duty-cycle that, during a switching period, would generate the required average voltage at the inverter terminals. Consider the following reasoning.

The discretization of the equation describing the current through the inductor L over a switching period leads to

$$i_L(k+1) = i_L(k) + \frac{1}{L \cdot f_{sw}}[v_{inv}(k) - v_o(k)], \tag{4.1}$$

where v_{inv} is the average voltage generated at the inverter output before filtering (see Figure 4.1) and f_{sw} is the switching frequency, which is equivalent to the PWM carrier frequency. The samples are acquired once a switching cycle, synchronously with the PWM, such that $i_L(k)$ is the average value of the inductor current within a switching period. Using (4.1), one could determine the voltage $v_{inv}(k)$ that would lead the current $i_L(k+1)$ to the desired value at instant $k+1$. In practical terms, though, it is crucial to consider the computational delays involved, since the calculations take a finite amount of time to execute. A conservative but effective way of doing so is to reserve a whole sampling period for calculations. Thus, (4.1) should be delayed by one sampling period, resulting in

$$i_L(k+2) = i_L(k+1) + \frac{1}{L \cdot f_{sw}}[v_{inv}(k+1) - v_o(k+1)]. \tag{4.2}$$

Substituting (4.1) into (4.2),

$$i_L(k+2) = i_L(k) + \frac{1}{L \cdot f_{sw}}[v_{inv}(k+1) + v_{inv}(k) - v_o(k+1) - v_o(k)]. \tag{4.3}$$

Considering that the filtered voltage v_o does not vary very much between two consecutive samples, i.e. $v_o(k+1) \approx v_o(k)$, the following expression is obtained

$$v_{inv}(k+1) = -v_{inv}(k) + 2v_o(k) + Lf_{sw}[i_L(k+2) - i_L(k)]. \tag{4.4}$$

Finally, knowing the relation between v_{inv} and the modulating signal (m) (see Appendix A), one can deduce

$$m(k+1) = -m(k) + \frac{L^m \cdot f_{sw}}{V_{dc}^m}[i_{ref}(k) - i_L(k)] + \frac{2}{V_{dc}^m}v_o(k), \tag{4.5}$$

where $i_L(k+2)$ was replaced by its reference value i_{ref} at instant k, and V_{dc}^m is the dc-link voltage. Note that both V_{dc}^m and L^m now carry a superscript, indicating that they are considered as *model quantities* used for calculations, which might differ from the values present in the real setup. In case of parameter mismatch, the controller performance is degraded and, in case of strong mismatch, the controller becomes unstable (BUSO *et al.*, 2019), as will be detailed in section 4.2.3. In this work, the model quantities are considered to be matched with the real setup unless otherwise mentioned.

By means of (4.5), it is possible to derive the modulation signal to be applied at instant $k+1$ based on the information about the system quantities at instant k. Hence, from instant $k+1$ to $k+2$, the desired average voltage will be produced by the inverter such that the inductor current reaches the reference at instant $k+2$. Thus, the closed-loop transfer function between i_L and i_{ref} is simply given by a two-sample delay. This reasoning is summarized in Figure 4.3. Since the calculation results are applied at every switching cycle, the current loop is said to operate at a rate equal to f_{sw}.

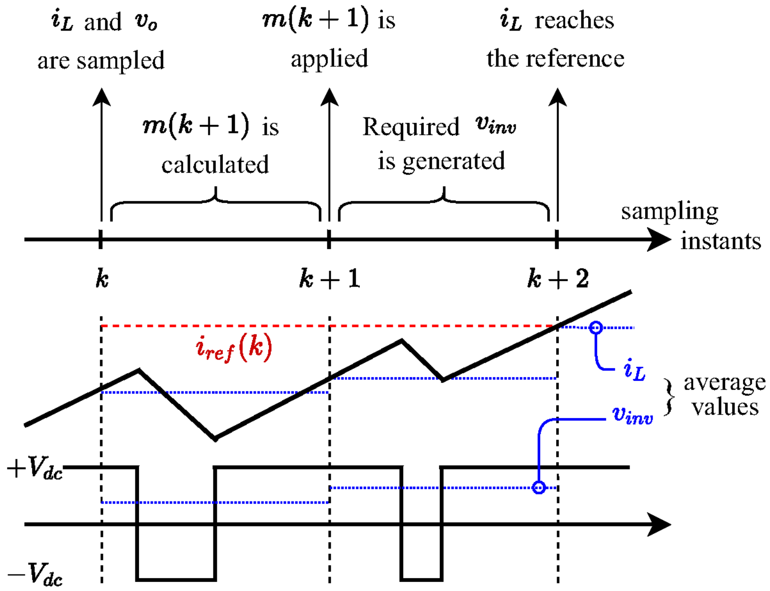

Figure 4.3 – Timeline for DB current control.

4.2.2 Voltage Loop

The voltage loop can be understood in terms of the dynamic equation characterizing the output capacitor, and in terms of the Kirchhoff's current law for the node connecting the load to the LC filter. A DB control law could be derived to determine the appropriate current i_c that leads v_o to its reference value. Hence, the outer loop could use the calculated i_c and the load current (i_o) to generate the reference to be used by the inductor-current controller. Thus, the output of the voltage loop can be written as

$$i_{ref} = i_c + i_o = \Delta i_c + i_{c,FF} + i_o, \tag{4.6}$$

where the capacitor current was split into two different components: $i_{c,FF}$ is a portion that is feedforwarded and Δi_c corresponds to the deviations that have to be regulated by the DB voltage control.

The reasoning behind the use of the feedforward strategy is worth commenting: since the relation between the capacitor's voltage and current is well-known, i_c can be directly estimated from the voltage reference via any discrete-derivative technique, as

$$i_{c,FF}(k) = C^m f_{sw} \cdot [v_{ref}(k) - v_{ref}(k-1)]\,, \tag{4.7}$$

where C^m is the capacitor value used in the computations, and v_{ref} is the voltage reference. Of course, if this feedforward estimate were used alone, the system would not operate in closed-loop. Consequently, the voltage controller must work alongside in order to generate the portion Δi_c, which compensates any deviation. The expression for Δi_c that exhibits a DB behavior (BUSO *et al.*, 2001) is given by

$$\Delta i_c(n) = -\Delta i_c(n-1) + \frac{C^m \cdot f_{sw}}{2} \cdot [v_{ref}(n) - v_o(n)]. \tag{4.8}$$

As demonstrated in Appendix B, (4.8) is constructed in such a way that the voltage reaches its reference value in a single control cycle. However, in order not to deteriorate system's phase margin and to avoid instabilities, Δi_c should not be updated at the same rate as the current loop (BUSO *et al.*, 2001). Instead, (4.8) must be computed only at every two switching periods since the current loop introduces a two-cycle delay. By doing so, the delay introduced by the inner loop becomes negligible from the voltage loop point of view (BUSO; MATTAVELLI, 2006). That is why the independent variable k was replaced by n in (4.8), indicating that the sampling instants occur at every $n \cdot 2/f_{sw}$. For this reason, the voltage loop is said to operate at a rate equal to $f_{sw}/2$ even though the components $i_{c,FF}$ and i_o, which constitute the current reference as well, are updated every switching period.

The timeline in Figure 4.4 shows the sequence of events of the voltage controller with respect to the inner loop. Once v_o and i_o are sampled, i_{ref} is calculated using (4.6)–(4.8) and the measured load current (i_o). With the result, the next modulation index can be obtained through (4.5). Note that, differently from the current loop, no extra delays need to be deliberately introduced to take into account the computational delay. This is only possible for the fact that the voltage loop operates at a slower rate. The only constraint is that the total time for calculating both i_{ref} and m does not take longer than a switching period.

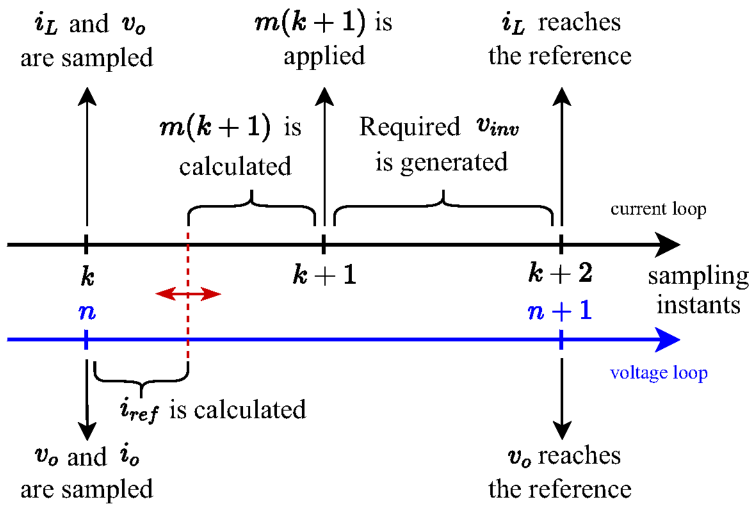

Figure 4.4 – Timeline for complete DB control.

The complete control diagram, including both control loops, is depicted in Figure 4.5. Note that a distinction is made between the different operation rate domains. The block $T_{comp}(z)$ in the current loop represents the computational delay, which corresponds to the one-sample delay (z^{-1}) that was reserved for calculations when developing (4.5). Following the $T_{comp}(z)$ block, there is the PWM model, which will be detailed in the next chapter. The inverter itself is represented by the gain V_{dc}, while $Z_L(z)$ and $Z_C(z)$ account for the discrete impedances of the LC-filter inductor and capacitor, respectively. All gains and filters related to signal conditioning were omitted for the sake of simplicity.

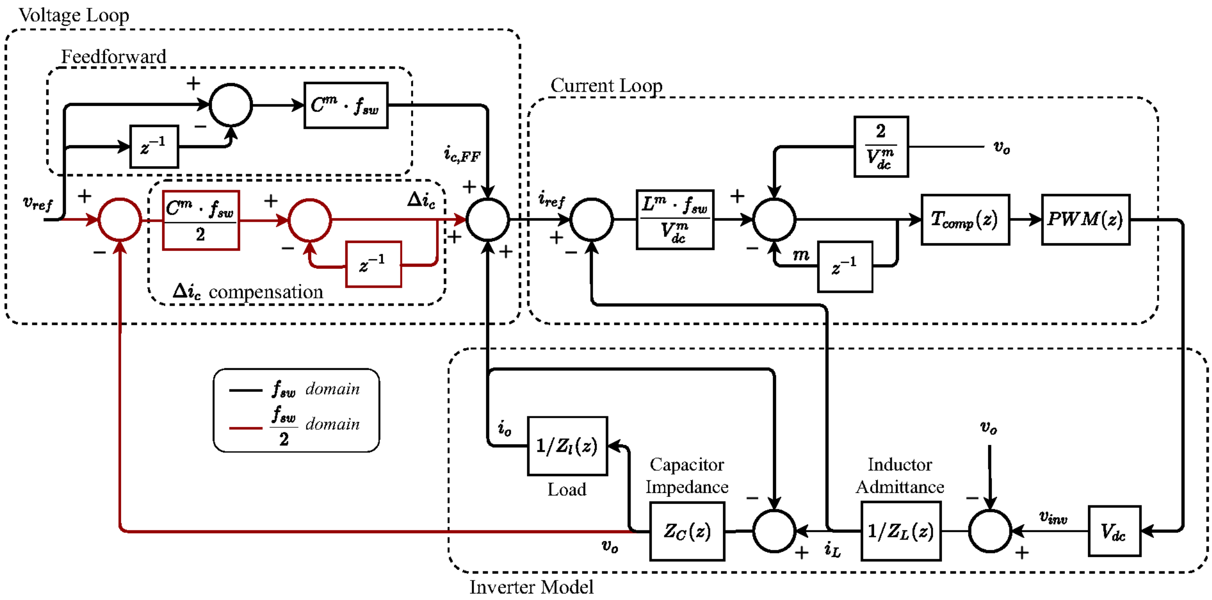

Figure 4.5 – Complete control diagram.

4.2.3 Internal Stability Analysis

The stability of a DB controller is typically analyzed regarding the behavior of its closed-loop poles upon parameter mismatches, which is one of the most important concerns related to the DB—whose mitigation has been sought by many works (BODE *et al.*, 2005; MARTIN; SANTI, 2014). In this paper, this approach is referred to as the analysis of the DB *internal stability* since no external influence is taken into account. By external influence, one should understand as any output that is fed back into a loop but that is not directly controlled by it.

For example, from Figure 4.5, the current-loop can be simplified into the diagram shown in Figure 4.6 if the influence of v_o is neglected. In this analysis, the digital PWM model is not taken into account as well. From this diagram, the open-loop transfer function $H_i(z)$ of the inner loop can be written as

$$H_i(z) = \frac{L^m \cdot f_{sw}}{V_{dc}^m} \cdot \frac{1}{1+z^{-1}} \cdot z^{-1} \cdot V_{dc} \cdot \frac{1}{Z_L(z)}. \tag{4.9}$$

If the forward-Euler discretization method is applied, $Z_L(z)$ can be written as

$$Z_L(z) = L f_{sw} \cdot \frac{1-z^{-1}}{z^{-1}}. \tag{4.10}$$

Although any other discretization method could be applied, the forward-Euler was utilized to ensure consistency since the DB equations are also obtained through this method.

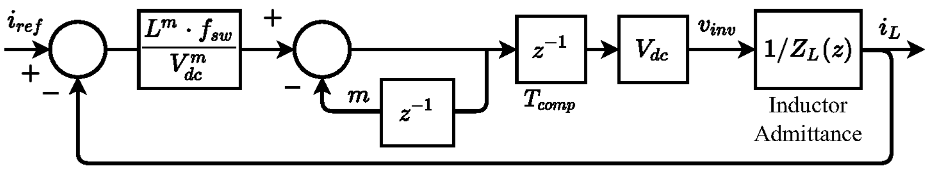

Figure 4.6 – Current-loop direct path considering $v_o \equiv 0$.

From (4.9) and (4.10), the closed-loop transfer function $G_i(z)$ can be determined as

$$G_i(z) = \left[\frac{L}{L^m}\frac{V_{dc}^m}{V_{dc}}z^2 + \left(1 - \frac{L}{L^m}\frac{V_{dc}^m}{V_{dc}}\right)\right]^{-1}, \tag{4.11}$$

whose poles are given by

$$z = \pm\sqrt{\left[1 - \frac{L}{L^m}\frac{V_{dc}^m}{V_{dc}}\right]\left[\frac{L}{L^m}\frac{V_{dc}^m}{V_{dc}}\right]}. \tag{4.12}$$

If no parameter mismatch is present, i.e. $L^m = L$ and $V_{dc}^m = V_{dc}$, the pole pair remains at the origin of the z-plane as desired, resulting in $G_i(z) = z^{-2}$. Figure 4.7, however, shows the behavior of the poles upon inductance and dc-link voltage mismatch. For the inductor case, considering that there is no error regarding V_{dc}^m, the internal stability is ensured as long as L^m does not go beyond twice the value of the real inductor, since the poles remain within the unit circle (see Figure 4.7a). For an error on the other direction, with $L^m < L$, the system stability is not at risk. It is worth remarking that even if the eventual mismatch is not strong enough to cause instability, the performance of the controller can be deeply degraded inasmuch as the poles move away from the origin.

Similar conclusion holds for mismatches regarding V_{dc}^m. This time, the system becomes unstable if V_{dc}^m is lower than half of the real V_{dc} value (see Figure 4.7b). In practical applications, the inductance parameter is a matter of more concern than the dc voltage one. Whereas the V_{dc} value can be easily measured and dynamically updated in the control equations, the online identification of the inductance may require more advanced techniques (MARTIN; SANTI, 2014).

Figure 4.8 shows the step response of the current controller obtained through simulation using a switched model in PSIM. The step responses are acquired for different levels of mismatch of the parameter L. Remark that the sampled inductor current reaches the reference value in two samples when $L^m = L$, as desired by the DB formulation. When the mismatch is present, however, the control performance diverges from the expected one. For $L^m < L$, the response is overdamped, whereas it becomes undamped for $L^m > L$. Note that an oscillatory, unstable response is obtained when $L^m = 2L$, as expected. It is worth commenting that this simulation includes a digital PWM block; hence, despite the fact that it had been neglected during the aforedescribed analysis, the conclusions still hold.

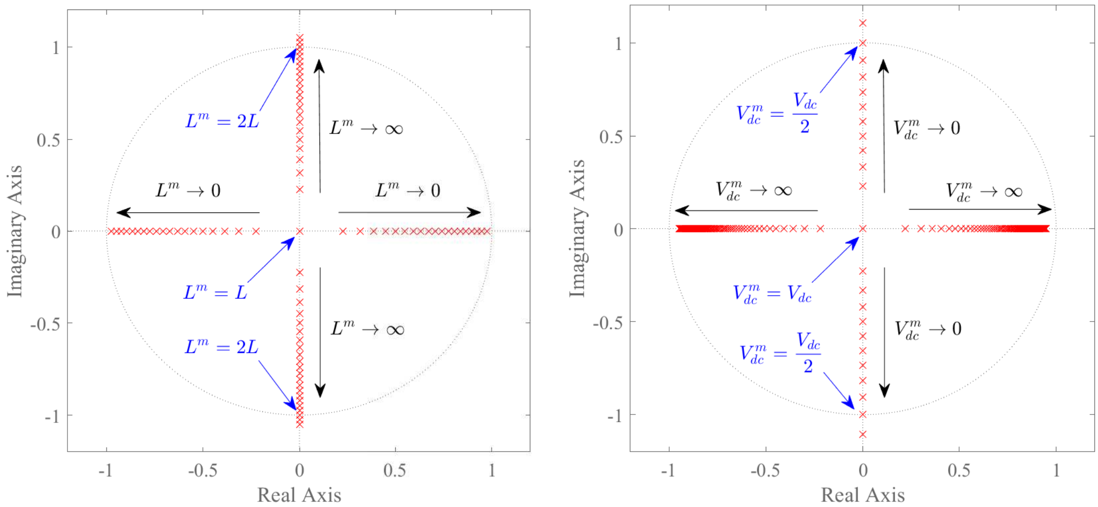

(a) (b)

Figure 4.7 – Influence of parameter mismatches on the closed-loop poles of the current controller with respect to (a) L^m, with $V_{dc}^m = V_{dc}$, and (b) V_{dc}^m, with $L^m = L$.

For the voltage loop, the simplified diagram is presented in Figure 4.9, where the influence of the load current was neglected. Also, the feedforward component was not considered since the poles and zeros that it introduces are not affected by parameter uncertainties. Recalling that the voltage loop operates at half the rate of the current loop, the analysis would not be possible if both parts of the system were not represented in a single-rate fashion. For that purpose, the two-sample delay introduced by the current loop—with respect to a sampling frequency equal to f_{sw}—was considered as a pure unit delay so that it becomes consistent with the voltage-loop rate. That is why $G_i(z)$ appears as z^{-1} in Figure 4.9.

Following the same reasoning as for the current loop, the closed-loop transfer function $G_v(z)$ that represents the voltage controller is

$$G_v(z) = \frac{C^m}{C} \cdot \left[z^2 + (\frac{C^m}{C} - 1) \right]^{-1}. \tag{4.13}$$

It can be shown that the poles of $G_v(z)$ respond to a mismatch regarding C^m in the same way the poles of $G_i(z)$ do for the parameter L^m. Hence, if $C^m > 2C$, the voltage loop becomes unstable. The voltage loop internal analysis is not as straightforward as for the current loop, since the rate domain transition, the load current feedback, and the use of feedforward introduce certain dynamics that are not taken into account. For this reason, the voltage loop performance upon parameter mismatches will be discussed based on the experimental results that will be presented in the next section.

It is worth emphasizing that the analysis of the herein-called internal stability considers both the feedback of v_o in the current-loop and the feedback of i_o in the voltage

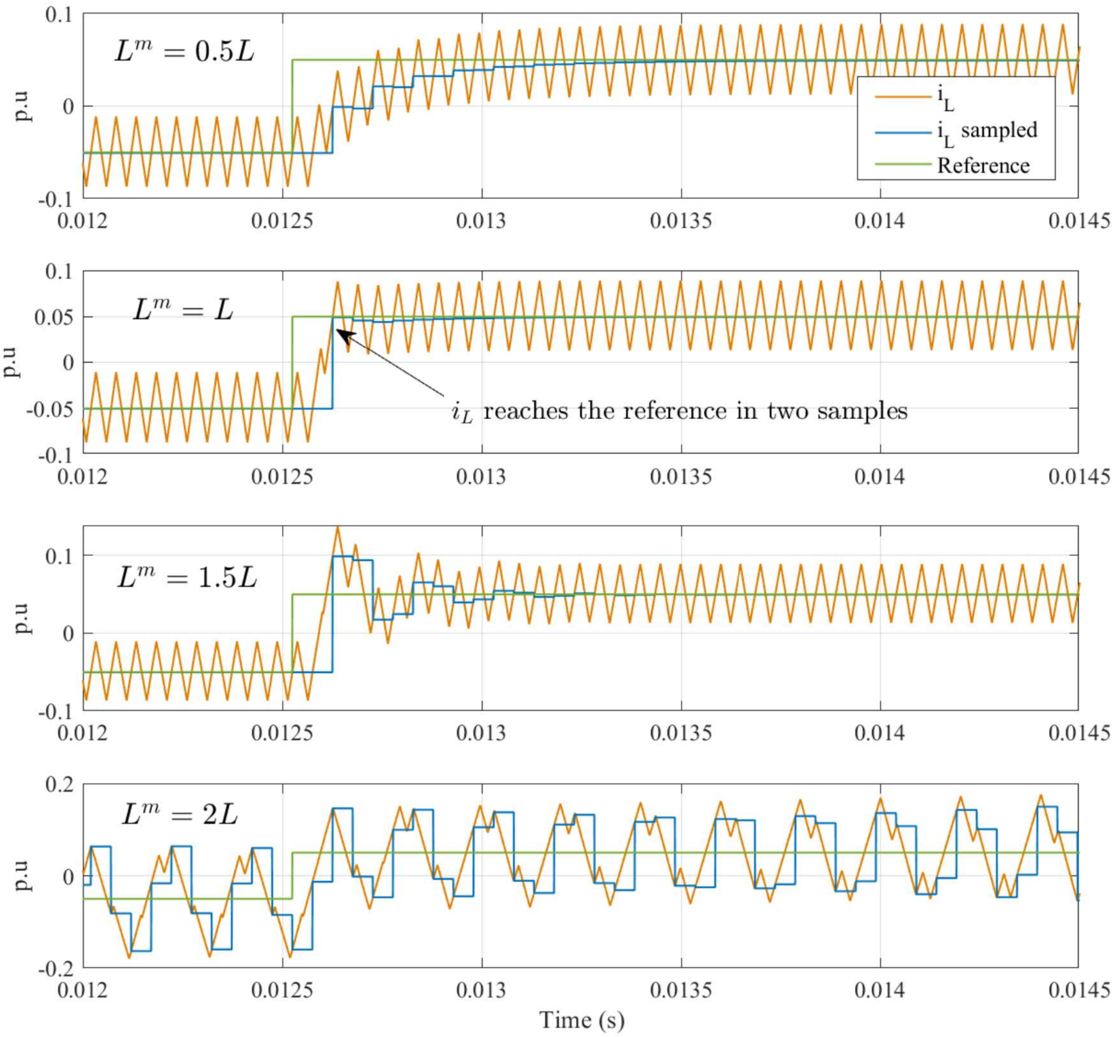

Figure 4.8 – DB current controller step response upon inductance parameter mismatch.

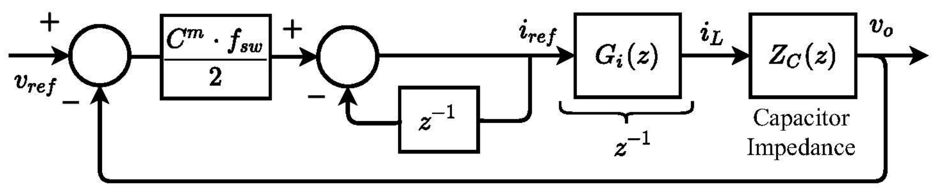

Figure 4.9 – Voltage-loop direct path considering $i_o \equiv 0$.

loop as disturbing signals; by doing so, these quantities are treated as if they were independent inputs of the system—yet they are affected by the controller itself and also by the load. Even if all parameters match perfectly the real values, the system might become unstable upon certain conditions from the IBSC point of view. As explained in Chapter 2, even if the controller is stable by design, interactions between the converter and the network may engender instabilities.

4.3 Hardware Description

In this work, the experiments are realized using a three-phase, four-leg Supplier® inverter assemblage (Figure 4.10) configured as shown in Figure 4.11, with the main parameters presented in Table 4.1. The neutral point is connected to the middle point of the split-capacitor dc link. The fourth transistor leg is used as a buck-boost converter with constant 50% duty-cycle to balance the dc voltages. Even though the hardware is for three phases, it is important to emphasize that the focus of this dissertation is the analysis of a single-phase GFI. Due to the access to the neutral point, the single-phase DB controller herein discussed can be straightforwardly extended to a three-phase version, since each phase can be independently controlled. The only precaution that must be taken is to consider the V_{dc}^{m} parameter as half the total dc-link voltage, since this is the effective voltage applied to one phase with respect to the neutral point. With this in mind, the analysis of the single- and the three-phase versions are equivalent. In future applications, this hardware will be used as a three-phase, four-wire GFI in the microgrid of the Laboratory of Microgrids (LabREI) at Unicamp.

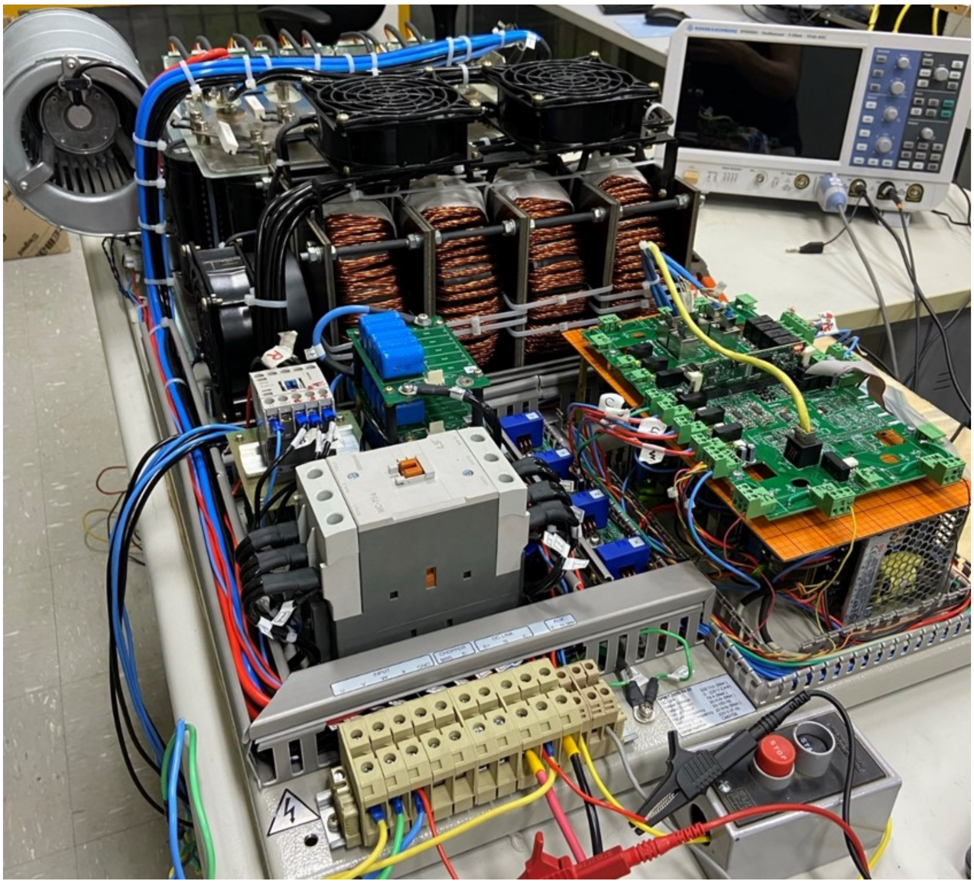

Figure 4.10 – GFI hardware.

The controller is implemented in a F28335 DSP using PSIM's SimCoder library for code generation. The currents are measured using LA 100-P LEM ® Hall-effect sensors,

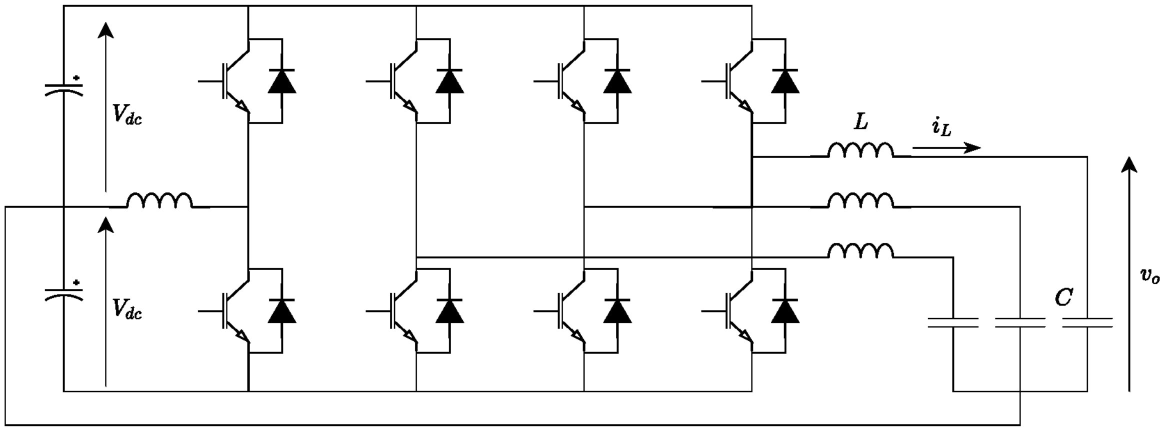

Figure 4.11 – GFI hardware configuration.

Table 4.1 – Setup parameters

GFI	
Power (S)	10 kVA (single-phase)
Output voltage (v_o)	127 V_{rms}
Output frequency	60 Hz
Dc-link voltage	600 V (V_{dc} = 300 V)
Switching frequency (f_{sw})	19.8 kHz
LC filter	
Inductance (L)	625 µH
Capacitance (C)	105 µF
Cut-off frequency	~620 Hz

whereas the Agilent® HCPL-7510 sensor is used for voltage sensing. The measured signals are conditioned and filtered through second-order Butterworth analog filters. For the inductor current (i_L) the cut-off frequency is set at 50 kHz, while the load current (i_o) and the output voltage (v_o) are filtered at 19.8 kHz. These values are summarized in Table 4.2. Note that, in this application, these filters work as denoising filters, and not as anti-aliasing, since the switching and sampling frequencies are set at 19.8 kHz as well. Specially for the inductor current, no anti-aliasing filter is needed due to the synchronism between sampling and PWM, since what is to be reconstructed by the samples is the instantaneous average value of the current, and not the entire current itself (BUSO; MATTAVELLI, 2006). An anti-aliasing filter would introduce delays, compromising the synchronism and thus affecting the control performance. That is why a higher cut-off frequency is used for this current. Moreover, the inductor current is more immune to alias produced by external sources due to the filtering provided by the LC filter. For v_o and i_o, delays are of less concern due to the slower dynamics of the outer loop.

Table 4.2 – Cut-off frequencies of the denoising filters.

i_L	50 kHz
v_o	19.8 kHz
i_o	19.8 kHz

4.3.1 LC Filter Design

The LC filter is designed based on a standard methodology (Guerreiro *et al.*, 2018). The inductor is calculated to limit the current ripple (Δi_L) to 15% of the rated current. Based on

$$L > \frac{V_{dc}}{2 \cdot \Delta i_L \cdot f_{sw}}, \tag{4.14}$$

a lower limit of approximately 452 µH for the inductance can be found.

The capacitor is chosen to set a predetermined filter's cutoff frequency. Recall that all the operation principle of the DB controller is based on the average, within a switching period, of the regulated quantities, specially i_L and v_o. Thus, it is crucial that the samples represent, with small error, their average values. For the current i_L, this is ensured by the PWM and sampling synchronization. However, the same is not valid for the v_o samples. Thus, the cutoff frequency of the LC filter should be located many times below the switching frequency in order to ensure a small enough voltage ripple, and consequently a small error between the sampled and the average values. Previous simulations showed that a cutoff frequency approximately 30 times smaller than f_{sw} produced good results (BUSO *et al.*, 2001). The values of L and C that represent a good trade-off between the constraints imposed by (4.14) and the cutoff frequency are listed in Table 4.1.

4.4 Experimental Results

The performance of the DB-GFI was verified upon different scenarios, for both linear and nonlinear loads. Moreover, experiments were realized in order to analyze the effect of parameter mismatches on the generated output voltage.

4.4.1 Resistive Load Test

Before adding the resistive load, the GFI was tested unloaded, as shown in Figure 4.12a. All the voltages presented in this section where measured using a 1 V:1000 V probe, such that 1 mV in the figures correspond to 1 V in the setup unless otherwise mentioned. As confirmed by the spectral content presented in Figure 4.12b, the voltage generated by the converter is sinusoidal, with no significant harmonic content. The RMS value measured by the oscilloscope (125.7 V) is slightly different (≈1%) from the expected one of 127 V.

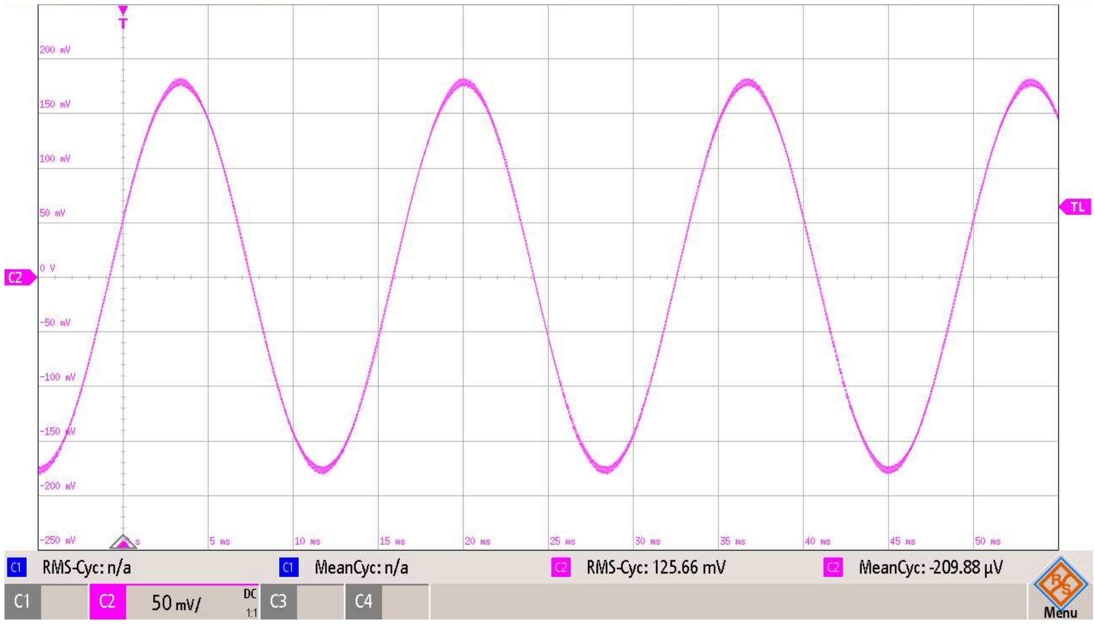

(a)

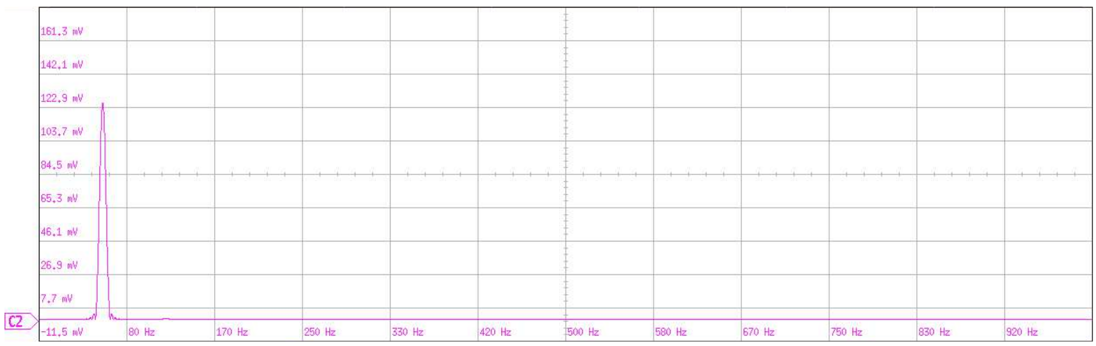

(b)

Figure 4.12 – (a) Output voltage (v_o) for the no-load condition, and (b) its FFT.

Figure 4.13[1] shows the waveforms for the converter supplying three levels of resistive load—approximately 400 W, 750 W, and 1 kW, which represent 4%, 7.5%, and 10% of the rated power, respectively. A voltage drop is observed with respect to the unloaded case. This is due to the non-null value of the converter's impedance at 60 Hz. Even though the controller is designed so the converter behaves as close as possible to an ideal voltage source, with low impedance, this is not achieved in practice. As will be detailed in Chapter 5, the impedance of the DB-GFI presents a low—but finite—value at 60 Hz, which causes a voltage drop when a current passes through. The values of the voltage drops for all three tested cases are listed in Table 4.3, with the corresponding percent variation with respect to the unloaded case (125.7 V). Although not really accurate due to the lack of extra data points, it is possible to estimate an impedance of roughly

[1] Current dc level due to measurement probe.

$0.5\,\Omega$ at 60 Hz for the GFI using the values in Table 4.3. This result will be contrasted with the ones obtained through the PRBS identification in Chapter 5.

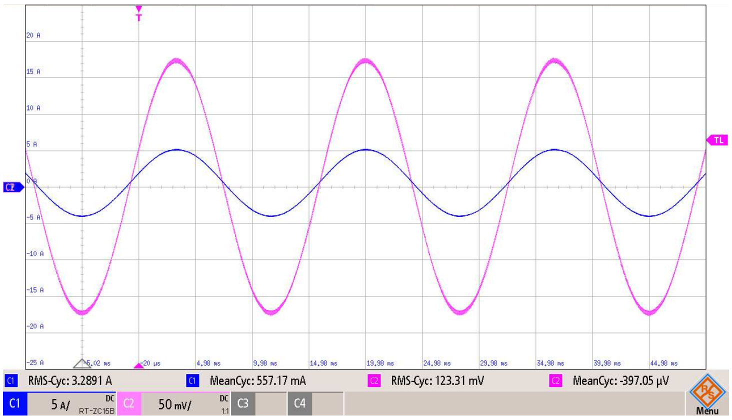

(a) $v_o = 123.31\,\mathrm{V}_{rms}$

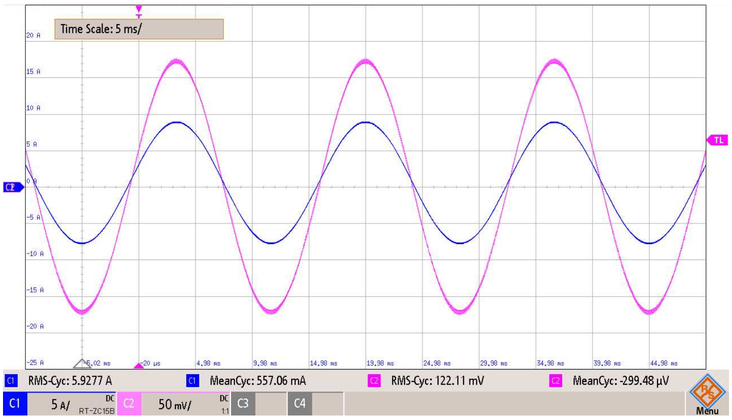

(b) $v_o = 122.11\,\mathrm{V}_{rms}$

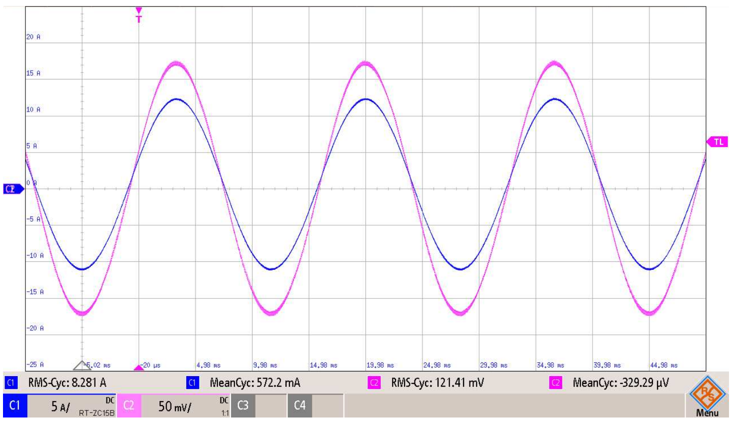

(c) $v_o = 121.41\,\mathrm{V}_{rms}$

Figure 4.13 – Output voltage (v_o) and load current (i_o) for (a) 400 W, (b) 750 W, and (c) 1 kW resistive loads.

Figure 4.14a shows the controller behavior upon the connection of a 1 kW resistive load. The connection occurs at the peak of the voltage, which is the worst point for the converter to respond. A voltage transient of approximately 15 V is observed, which is quickly extinguished by the controller in less than 0.5 ms. At this point, it is important

Table 4.3 – Voltage drop due to resistive load (with respect to 125.7 V).

Load	ΔV (V_{rms})	ΔV (%)
400 W	2.4	1.9%
750 W	3.6	2.9%
1 kW	4.3	3.4%

to separate two different effects involved in the transient—the controller response and the converter's physical limitations. A converter's capacity of delivering current is limited by the dc voltage and by the ac-filter inductance, since the allowed current variation through the inductor is given by

$$\Delta i_L = \frac{\Delta t}{L}(V_{dc} - v_o), \tag{4.15}$$

which varies depending on the instantaneous value of v_o. When v_o is at its peak, the GFI can deliver a maximum of 9.7 A (or 0.09 p.u.) in a switching cycle considering the parameters in Table 4.1. This value increases to 24.2 A (or 0.22 p.u.) when v_o is at the zero-cross. Thus, even if the controller were able to instantly respond to a load transient, the converter would be physically constrained in the case the current load variation exceeded these limits.

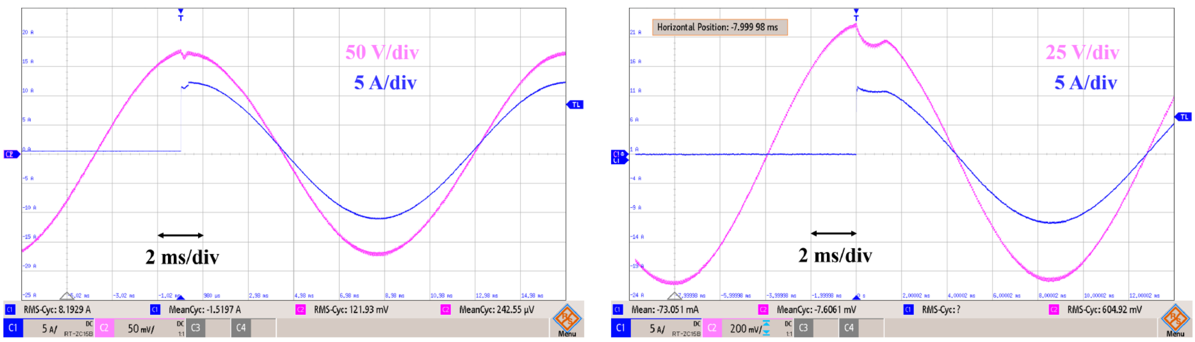

(a) (b)

Figure 4.14 – Output voltage (v_o) and load current (i_o) for a 1 kW load step for (a) V_{dc} = 300 V and (b)V_{dc} = 210 V.

Actually, the current step shown in Figure 4.14a represents a current variation that is above the hardware capacity. The current raises from zero to approximately 12 A almost instantly. Thus, the magnitude of the current step provoked by the load connection takes the controller out of the linear region of operation, making the modulating signal (m) reach the saturation ceiling of 1. Nonetheless, the DB controller manages to quickly extinguish the transient.

To illustrate the influence of the dc-link voltage on the GFI's dynamical performance, another test was carried out for a reduced value of V_{dc} (210 V), whose results are presented in Figure 4.14b. In this situation, the voltage delta over the inductor when v_o is at its maximum is of only 30 V in lieu of 120 V for the precedent case. This implies a decrease in the current delivery capacity, which drops to 2.5 A per switching cycle. The impact of this reduction is noticeable in the voltage transient shown in Figure 4.14b. Not only the voltage transient increases (to almost 25 V), but so does the time needed to suppress the transient (to approximately 1.5 ms).

4.4.2 Nonlinear Load Test

The DB performance was also tested for the nonlinear load depicted in Figure 4.15. It is a 650 W, single-phase diode rectifier with a dc-side LC filter, whose cutoff frequency is set at approximately 30 Hz.

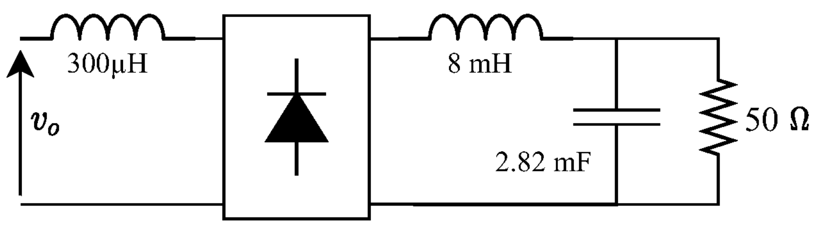

Figure 4.15 – Nonlinear load topology and parameters.

The voltage formed by the GFI and the current drained by the load are shown in Figure 4.16a with the respective FFT. According to the oscilloscope measurement, the power drained by the load is of approximately 490 VA. The harmonic values can be found in Table 4.4. The current presents a Total Harmonic Distortion (THD) of 48.68% (calculated up to the 40^{th} harmonic), with a crest factor of approximately 2. Despite the current distortion, the voltage remains almost unaffected, with a THD of 1.13%.

In order to test the GFI performance further, the 8 mH inductor was taken off the nonlinear load. With the capacitive filter only, the current crest factor increases to roughly 2.7, and the apparent power reaches 870 VA. Figure 4.17a presents the voltage and current waveforms as well as their spectral contents. A voltage peak flattening can be observed during the current pulses. The current distortion now reaches 114.7% while the voltage THD raised to 2.37%. The values for each harmonic component can be found in Table 4.5. It is worthy highlighting that the maximum load current variation is of approximately 0.4 A per switching cycle, which is comfortably within the GFI physical limitations, implying that the observed distortion regards only the controller performance.

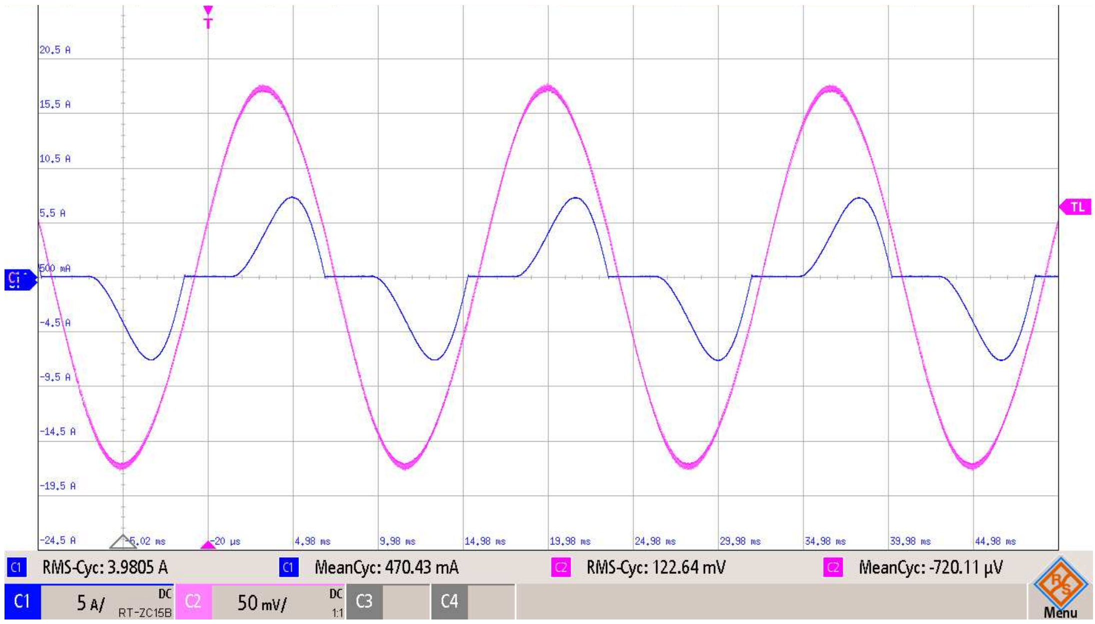

(a)

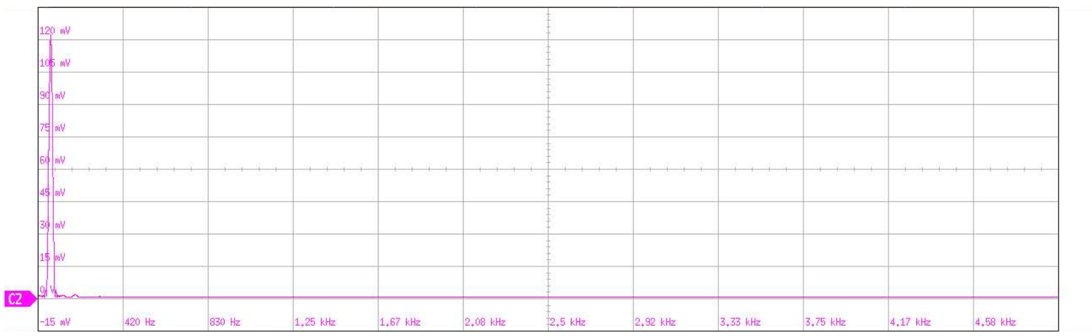

(b)

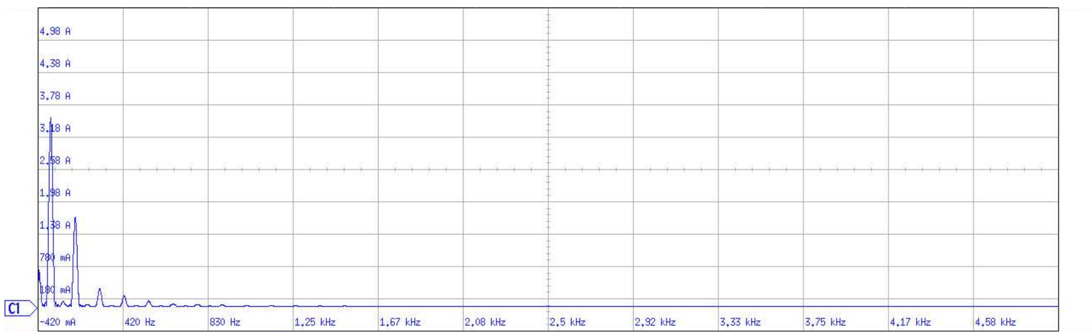

(c)

Figure 4.16 – (a) v_o and i_o waveforms and their and their respective FFT in (b) and (c) for the nonlinear load case.

4.4.3 Operation Upon Parameter Mismatch

As explained in section 4.2.3, the performance—and even the stability—of the DB controller may be compromised in case of parameter uncertainties. The steady-state performance of the DB-GFI was tested for mismatches in the parameters L^m and C^m aiming.

Table 4.4 – Voltage and current harmonics for the nonlinear load (with LC filter) test.

Harmonic order	v_o (V_{rms})	i_o (A_{rms})	Harmonic order	v_o (V_{rms})	i_o (A_{rms})
1	122.3	3.543	2	0.00003	0.099
3	1.213	1.668	4	–	0.044
5	0.258	0.339	6	–	0.026
7	0.074	0.203	8	–	0.022
9	0.074	0.114	10	–	0.011
11	0.074	0.062	12	–	0.014
13	0.074	0.051	14	–	0.011
15	0.037	0.037	16	–	0.007
17	0.037	0.022	18	–	0.007

Table 4.5 – Voltage and current harmonics for the nonlinear load (with C filter) test.

Harmonic order	v_o (V_{rms})	i_o (A_{rms})	Harmonic order	v_o (V_{rms})	i_o (A_{rms})
1	122.9	4.622	2	0.700	0.298
3	2.173	3.981	4	0.111	0.192
5	1.547	2.913	6	0.074	0.070
7	0.810	1.709	8	–	0.022
9	0.258	0.700	10	–	0.062
11	0.074	0.192	12	–	0.044
13	0.258	0.295	14	–	0.004
15	0.184	0.247	16	–	0.026
17	0.037	0.107	18	–	0.037

The model parameters were shifted from the nominal values in order to emulate mismatches ranging from 50% to 120%. Figure 4.18 presents the GFI output voltage contrasted with the voltage reference for different cases. The voltage reference was read from the DSP using a 12-bit digital-to-analog converter (MCP4921/4922) through the serial peripheral interface (SPI) with a sampling rate of 1.2 kHz. That is why this signal is stepwise in the figure.

It is worthy pointing out that the mismatches are relative to the values the inductance and the capacitance are *supposed* to have—625 µH and 105 µF—, which may differ from the real values. Indeed, there will always be parameter uncertainties accounted for several reasons, as the components' manufacture and assemblage, the system's point of operation—the inductance, for instance, may vary depending on the current level—,

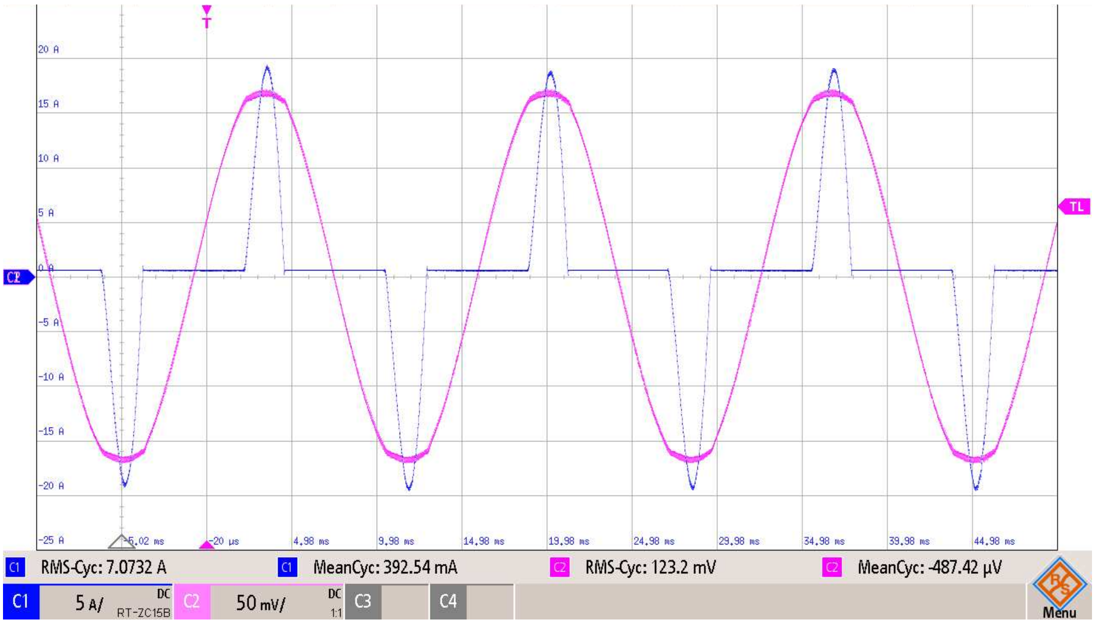

(a)

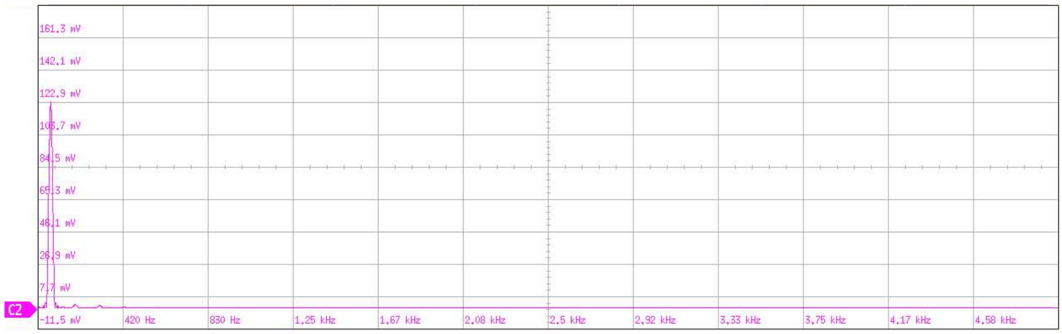

(b)

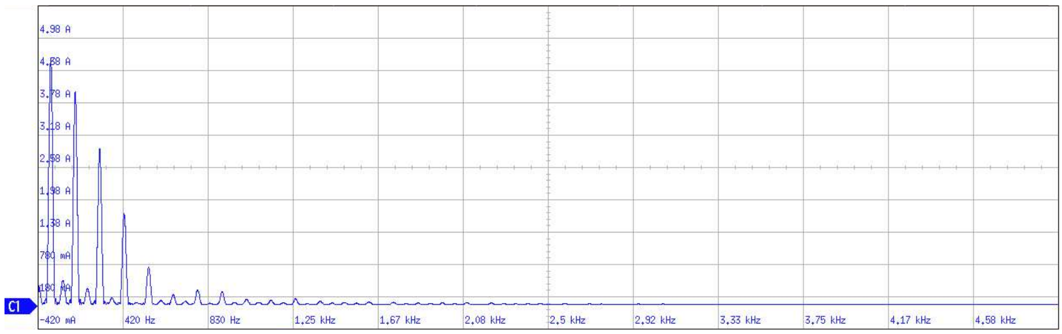

(c)

Figure 4.17 – (a) v_o and i_o waveforms and their and their respective FFT in (b) and (c) for the nonlinear load case with capacitive filter only.

unmodeled effects, etc. Thus, the real mismatch present in the tested cases may be slightly different from the expected one.

From the results in Figure 4.18, no severe issue was observed for the tested cases, specially for the mismatches in L^m. The most noticeable performance degradation concerns the test for $C^m = 0.5C$ (Figure 4.18b), in which v_o remarkably lags behind the reference, specially when v_o is increasing in value.

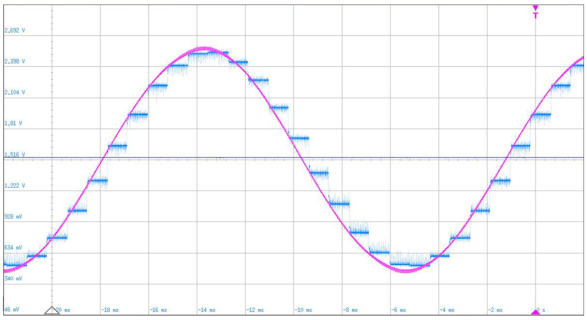

(a) $L^m = 0.5L$

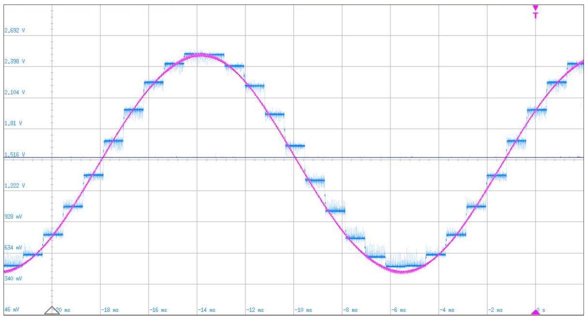

(b) $C^m = 0.5C$

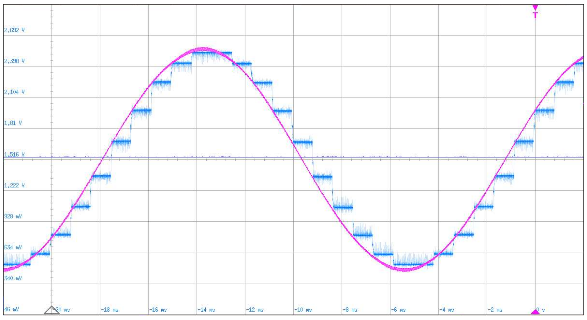

(c) $L^m = 0.8L$

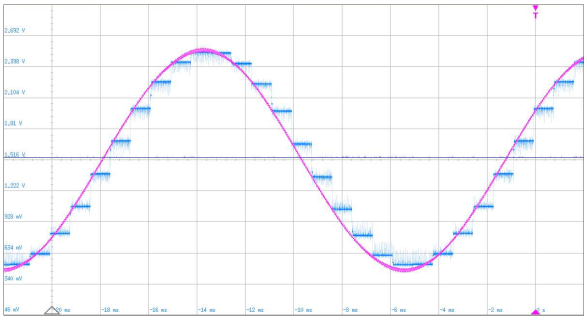

(d) $C^m = 0.8C$

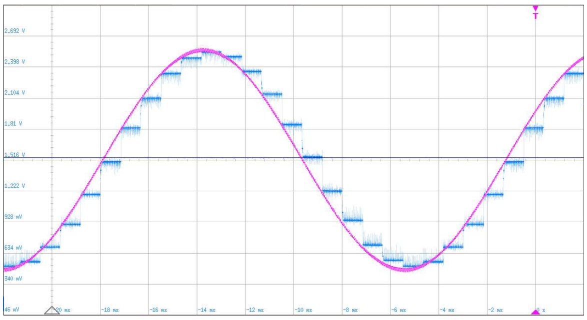

(e) $L^m = 1.2L$

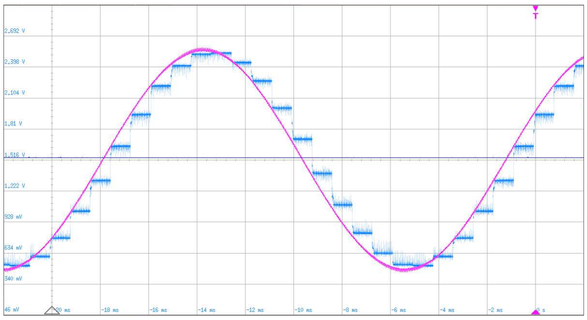

(f) $C^m = 1.2C$

Figure 4.18 – Output voltage v_o (in pink), and voltage reference (in light blue) for different mismatches between model (L^m, C^m) and setup parameters (L, C).

4.5 Partial Conclusions

The DB-GFI operation was verified for different scenarios. The controller was able to satisfactorily follow the 60 Hz sinusoidal reference, specially for the unloaded case. When supplying the resistive loads, voltage drops were observed in v_o due to the converter impedance at 60 Hz, roughly estimated as $0.5\,\Omega$. For the nonlinear load tests, the current distortion affected the output voltage within acceptable limits, reaching a THD of 2.37% when supplying the rectifier with capacitive filter only. This value is reasonable considering the elevated magnitude of the current THD (114.7%). It is important to note, however, that the load level was not the nominal one in any of the tested scenarios. In the nonlinear load case, the voltage distortion would increase for higher power levels if the current shapes were kept the same.

Concerning parameter mismatches, no major issues were verified for the tested scenarios. However, it is worthy pointing out that the mismatches were kept within the theoretical stability limits. The tested range comprises mismatch values that would occur in practice, though.

The 60 Hz voltage drop and the distortion upon nonlinear load suggest that the DB-GFI impedance in the harmonic range is not negligible—and may not be as negligible as expected by the ideal DB performance. In the next chapter, the impedance model of the GFI will be presented and measured. With the theoretical model and the measurement at hand, the effects influencing the converter impedance and dynamics will be further explored, contrasting the analysis with the results presented in this chapter. Also, an improvement on the DB controller will be discussed.

5 Grid-Forming Inverter Impedance Model and Measurement

In this chapter, the DB-GFI impedance model is presented. Initially, a model is derived for the inverter operating as a current source, with only the current loop closed. Then the complete model, including the outer voltage loop, is derived. The effect of the parameter mismatches on the inverter's impedance is analyzed as well. The method exposed in Chapter 3 is employed to identify the DB-GFI impedance experimentally. From the comparison between the measured impedance and its analytical model, a possible improvement for the DB controller is identified and tested.

5.1 DB-GFI Impedance Model

5.1.1 Inverter as a Current Source

The impedance model for the current loop can be obtained from the controller scheme after some block-diagram algebra, as depicted in Figure 5.1. The result of the manipulations is a Norton equivalent circuit with an ideal current source of value $G_i \cdot i_{ref}$

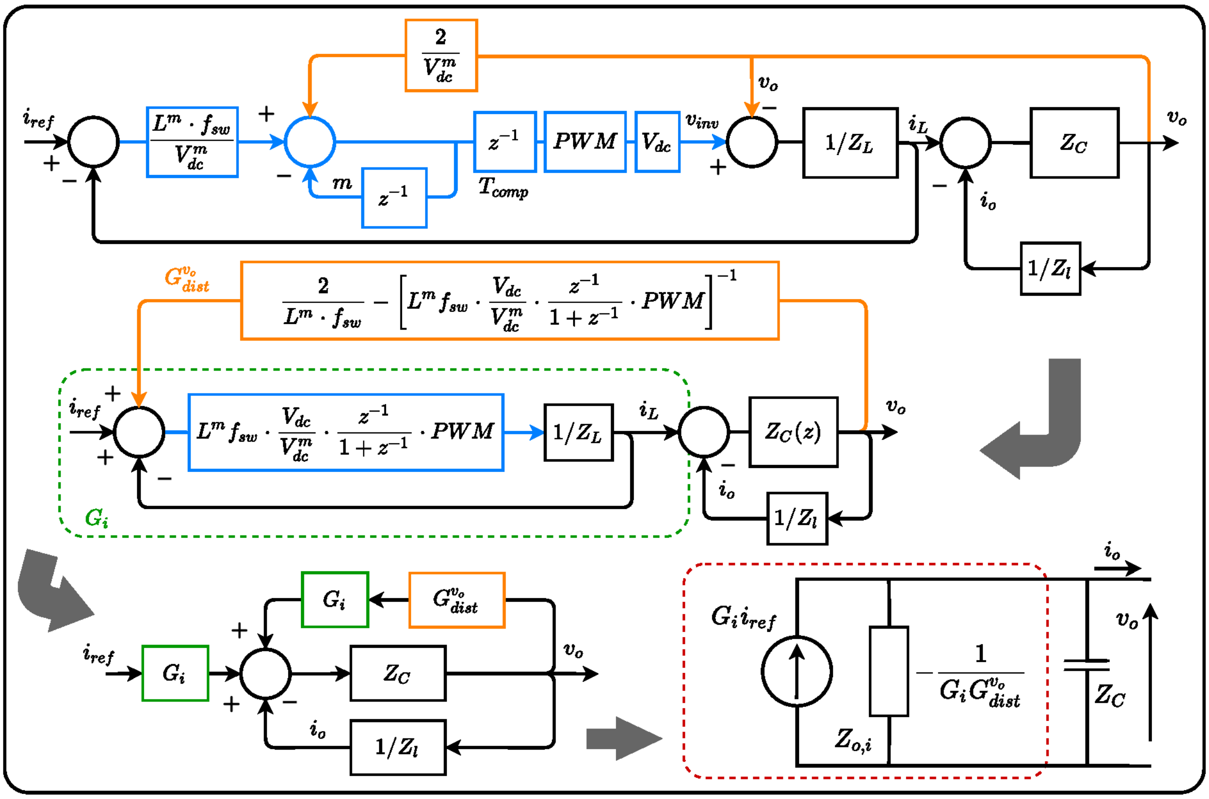

Figure 5.1 – Impedance model for the inverter operating as a current source.

in parallel with an impedance given by

$$Z_{o,i} = -\frac{1}{G_i G_{dist}^{v_o}}. \tag{5.1}$$

G_i represents the closed-loop transfer function of the inner loop, which is equal to the one derived during the internal stability analysis, except that, now, the PWM model is not neglected. As will be shown, neglecting the delay introduced by the PWM may result in an overestimation of the impedance value. The transfer function denoted by $G_{dist}^{v_o}$—where *dist* is for *disturbance*—accounts for the influence of the voltage feedback over $Z_{o,i}$.

The digital PWM small-signal representation for a triangular carrier is given by

$$PWM(s) = \frac{1}{2}\left[exp\left(-s\frac{(1-D)}{2f_s}\right) + exp\left(-s\frac{(1+D)}{2f_s}\right)\right] \tag{5.2}$$

in the s-domain (SYPE *et al.*,), where f_s is the sampling frequency and D is the duty-cycle at a certain point of operation. This equation is valid when the PWM is synchronized with the sampling process, and the samples are acquired once per switching cycle, during the modulator on-time. For ac operation, the average duty-cycle is equal to 0.5. By making $D = 0.5$ in (5.2), the equation reduces to

$$PWM(s) = exp\left(-\frac{s}{2f_s}\right), \tag{5.3}$$

which is equivalent to a half-sample delay. When the system is modeled in the discrete domain, the PWM is typically considered as a pure unit delay since it is not possible to readily represent a half-sample delay in the z-domain. Two options to work around this difficulty are 1) rewrite the control equations in the s-domain and model the entire system in s, or 2) rewrite (5.3) with a Padé approximant and discretize it, so that the entire system can be written in the z-domain. As it will be shown, both approaches lead to similar results.

For the continuous impedance model, $Z_{o,i}(s)$, the DB transfer functions in z, $G_i(z)$ and $G_{dist}^{v_o}(z)$, can be taken to the s-domain through the inverse transform of any discretization method. Again, the forward-Euler method is employed since the DB equations are derived using the forward-Euler integral. The relation between z and s is given by

$$z = \frac{s}{f_s} + 1. \tag{5.4}$$

For the discrete impedance, $Z_{o,i}(z)$, the DB equations are naturally in the z-domain—only the LC-filter and the PWM model have to be discretized. For the former, simple forward-Euler discretization technique is employed; for the latter, (5.3) is first written as its second-order Padé[1] form

$$exp\left(-\frac{s}{2f_s}\right) \approx \frac{1 - \frac{1}{4f_s}s + \frac{1}{24f_s^2}s^2}{1 + \frac{1}{4f_s}s + \frac{1}{24f_s^2}s^2}, \tag{5.6}$$

and then the forward-Euler discretization is applied.

Figure 5.2 presents the frequency response obtained for both continuous and discrete models of $Z_{o,i}$ for the setup parameters presented in Table 4.1. Both of them are compared with their respective versions that do not include the PWM half-sample delay. The figures also present, for reference, the frequency response identified in PSIM simulation through PRBS injection. In the simulation, a switching model of the converter was utilized and all components were considered ideal. Note that not taking the PWM model into account led to a 6 dB gap between the model and the PRBS reference. Even though a 6 dB difference may not be significant depending on the final purpose of the model, it still represents a factor-two error. It is interesting to notice that the PWM dynamics affect all the frequency range, which may compromise the accuracy of the outer loop impedance if not taken into account. A similar result was shown in (BUSO *et al.*, 2019). In this dissertation, the models that will be further derived from $Z_{o,i}$ will include the PWM effect.

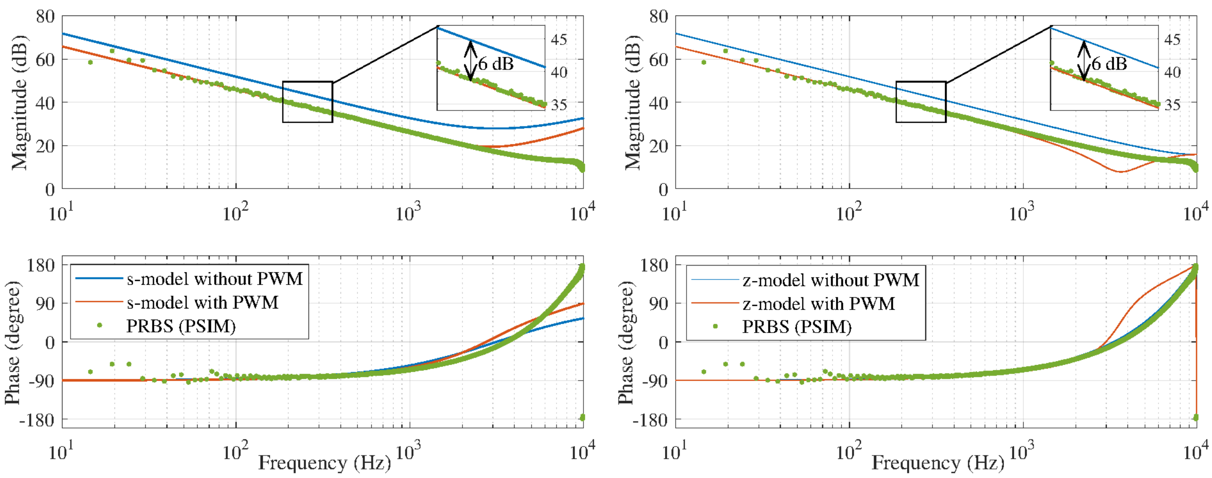

(a) s-domain

(b) z-domain

Figure 5.2 – Continuous (a) and discrete (b) impedance models for the current loop ($Z_{o,i}$), highlighting the effect of the PWM half-sample delay.

Comparing the continuous model in Figure 5.2a with its discrete version in Figure 5.2b, no meaningful difference is observed for frequencies lower than 1 kHz. For

[1] The second-order Padé approximant for a general delay function $exp(-\theta s)$ is given by

$$exp\,(-\theta s) \approx \frac{1 - \frac{\theta}{2}s + \frac{\theta^2}{12}s^2}{1 + \frac{\theta}{2}s + \frac{\theta^2}{12}s^2}. \tag{5.5}$$

higher frequencies, however, some small differences are spotted. Concerning the phase, the discrete model matches better the reference, presenting no noticeable error up to around 3 kHz, whereas a light mismatch is found for the continuous model from 1 kHz to 3 kHz. For the magnitude, the discrete model also outperform the continuous one for high frequencies—while $Z_{o,i}(s)$ diverges from the reference for frequencies above 3 kHz, $Z_{o,i}(z)$ response tends to keep track of the reference. Actually, $Z_{o,i}(z)$ without the PWM model matches perfectly the identified phase, and the same would occur for the magnitude if it were not for the 6 dB shift. The magnitude and phase high-frequency deviation regarding the z-model with PWM is assumed to be due to the approximation using the Padé form followed by discretization.

All models converge for the fact that the impedance acts as an integrator for lower frequencies, corresponding to a capacitive behavior. Considering no parameter mismatch, and neglecting the PWM effect, $Z_{o,i}(z)$ reduces to

$$Z_{o,i}(z) = \frac{L^m f_{sw} \cdot z^2}{z-1}, \tag{5.7}$$

in the discrete domain, from which it is possible to derive the equivalent capacitance as $1/(L^m f_{sw}^2)$. Since the PWM acts reducing the impedance by a factor of two, the equivalent impedance considering this effect is given by two times the latter, $2/(L^m f_{sw}^2)$.

In the following, the results herein presented will be used to derive the complete impedance model of the DB-GFI.

5.1.2 Inverter as a Voltage Source

Similar procedure can be applied to the outer loop. When including the voltage controller, however, some new challenges arise since the current and the voltage loops operate at different rates, as will be discussed.

The control diagram can be redrawn with the current loop represented in terms of the impedance model, as shown in Figure 5.3. Indeed, from the Norton equivalent circuit derived in the last section, the following equation holds

$$G_i i_{ref} - Z_{o,i} v_o = i_o + i_c. \tag{5.8}$$

As suggested in Figure 5.3, the system can be represented by a Thévenin equivalent circuit composed by an ideal voltage source of value $G_v v_{ref}$ with a series impedance $Z_{o,v}$. The transfer functions $G_{i_c,FF}$ and $G_{\Delta i_c}$ accounts for the capacitor-current feedforward and the voltage loop DB equation, respectively. The term G_v represents the voltage controller closed-loop transfer function, which can be found as the relation between v_o and v_{ref} when i_o is zero, as

$$G_v = \left.\frac{v_o}{v_{ref}}\right|_{i_o=0}. \tag{5.9}$$

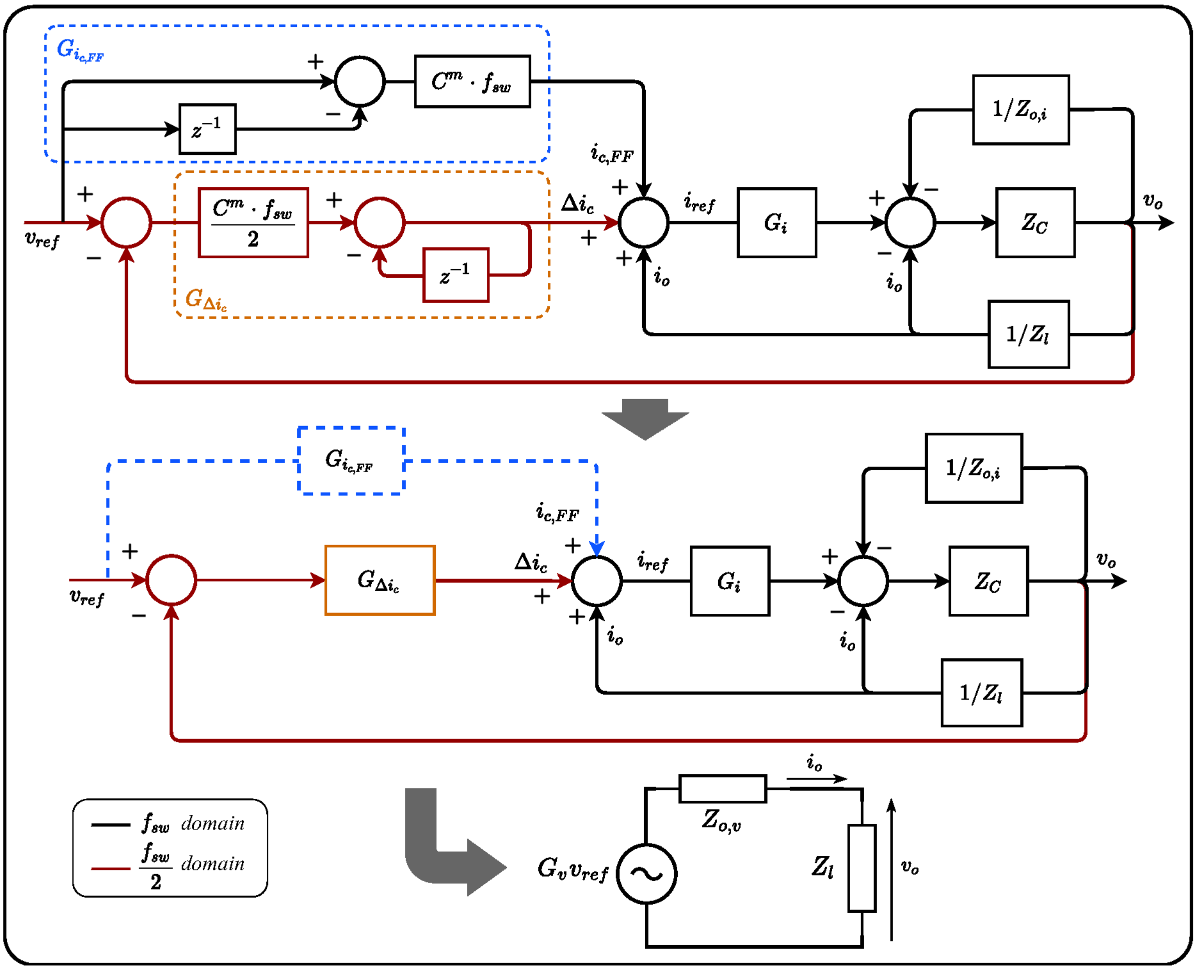

Figure 5.3 – Impedance model for the inverter operating as a voltage source.

Similarly, the impedance $Z_{o,v}$ corresponds to the relation between v_o and i_o when the voltage reference is zero, as in

$$Z_{o,v} = -\frac{v_o}{i_o}\bigg|_{v_{ref}=0}, \tag{5.10}$$

where the negative sign is for the adopted current direction convention. Note that the feedforward has no impact on the impedance since it only has the voltage reference as input.

All the elements corresponding to the current loop have been modeled in the previous section for both continuous and discrete domains. The next step consists of correctly integrating $G_{i_c,FF}$ and $G_{\Delta i_c}$ into the model, recalling that $G_{\Delta i_c}$ operates at half the frequency of the inner loop. To deal with this issue, two of the possible procedures are 1) resample $G_{\Delta i_c}$ at the same rate of the current loop in order to obtain the complete model in the z-domain, and 2) convert $G_{i_c,FF}$ and $G_{\Delta i_c}$ to the continuous domain and integrate them into the s-domain current-loop model. Both options require some sort of approximations, each one with its own advantages and disadvantages.

5.1.2.1 Discrete Model

For applying the z-domain approach, the DB transfer function

$$G_{\Delta i_c}(z)\Big|_{f_{sw}/2} = \frac{C^m f_{sw}}{2}(1 - z^{-1}), \tag{5.11}$$

can be written as if it were to be executed at twice the rate,

$$G_{\Delta i_c}^{f_{sw}}(z)\Big|_{f_{sw}} = \frac{C^m f_{sw}}{2}(1 - z^{-2}). \tag{5.12}$$

The only difference between (5.11) and (5.12) is that the unit delay was substituted by a two-sample delay in order to compensate for the rate change. Of course that this is just an approximation, since—in the real controller—$G_{\Delta i_c}(z)$ only changes its output (Δi_c) each two switching cycles. For the samples in between, the inner loop sees Δi_c as if it was under a holder effect.

Once this approximation is done, a single-rate diagram can be obtained so the discrete impedance model can be derived as

$$Z_{o,v}(z) = \frac{1 - G_i}{G_i G_{\Delta i_c}^{f_{sw}} + 1/Z_{o,i} + Z_C}, \tag{5.13}$$

whereas the closed-loop transfer function, including the feedforward effect, is given by

$$G_v(z) = \left[1 + \frac{G_{i_c,FF}}{G_{\Delta i_c}^{f_{sw}}}\right] \frac{G_{\Delta i_c}^{f_{sw}} G_i Z_C Z_{o,i}}{Z_{o,i} + Z_C + G_{\Delta i_c}^{f_{sw}} G_i Z_C Z_{o,i}}. \tag{5.14}$$

5.1.2.2 Continuous Model

Concerning the continuous model, it can be obtained in a more straightforward way by applying the forward-Euler transform to $G_{i_c,FF}$ and $G_{\Delta i_c}$ using the corresponding sampling rates. Similar procedure is adopted in (PETRIC *et al.*, 2022), in which a multi-rate discrete system is modeled in the continuous domain by utilizing another z-to-s transform. It is important to recall that, in our case, a zero-order holder (ZOH) effect exist at the interface between both rate domains. Thus, a ZOH,

$$ZOH(s) = \frac{1 - exp(-sT_s)}{sT_s} = \frac{1 - exp(-s\frac{2}{f_{sw}})}{s\frac{2}{f_{sw}}}, \tag{5.15}$$

written with respect to the outer loop sampling rate ($1/T_s = f_{sw}/2$), is added in series with $G_{\Delta i_c}$, as shown in Figure 5.4.

The presence of this ZOH can be understood from another standpoint. In digital-controlled systems, the sample-and-hold effect is usually modeled as a ZOH with T_s corresponding to the sampling frequency of the system. By doing so, both continuous-to-discrete and discrete-to-continuous conversions are taken into account—the former regarding the sampling process, and the latter, the holding effect. In digital-controlled power

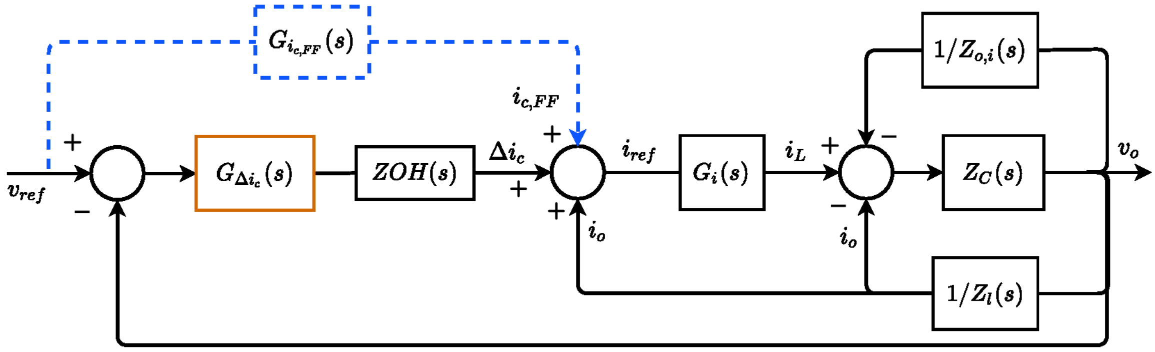

Figure 5.4 – Continuous domain diagram for impedance model derivation.

electronics systems, the PWM itself plays the role of the discrete-to-continuous converter; therefore, by including the PWM model, the ZOH effect is already taken into account. In our two-rate system, the PWM does play this role—only for the part of the system that operates at f_{sw}, though. Hence, for modeling the sample-and-hold effect regarding the signals that are sampled at half the switching frequency, the ZOH must be added. In the end, the equivalent continuous system becomes the one depicted in Figure 5.4, from which the s-domain form of $Z_{o,v}$ and G_v are deduced as

$$Z_{o,v}(s) = \frac{1 - G_i}{G_i G_{\Delta i_c}^{f_{sw}} ZOH + 1/Z_{o,i} + Z_C}, \tag{5.16}$$

$$G_v(s) = \left[1 + \frac{G_{i_c,FF}}{G_{\Delta i_c}^{f_{sw}} ZOH}\right] \frac{G_{\Delta i_c}^{f_{sw}} G_i Z_C Z_{o,i} ZOH}{Z_{o,i} + Z_C + G_{\Delta i_c}^{f_{sw}} G_i Z_C Z_{o,i} ZOH}. \tag{5.17}$$

Roughly, the difference between (5.16) and (5.17) and their discrete version is the ZOH term.

5.1.2.3 Model Comparison

The frequency response of $Z_{o,v}$ for both discrete and continuous domains are contrasted in Figure 5.5 with a PRBS identification result obtained via PSIM simulation. As previously done for $Z_{o,i}$, no nonidealities are considered in the simulation. The difference between both models is noticeable, specially for frequencies above 1 kHz. Also, differently from the current-loop impedance, none of the models match perfectly the identified response, even for frequencies lower than 1 kHz, where an approximately constant 2.5 dB mismatch is observed. This is assumed to be due to the approximations needed for obtaining both models. Looking at the PRBS response, an anti-resonance is observed at approximately 5 kHz, which correlates with half the operation frequency of the outer loop (4950 Hz). This effect is also pictured by the z-domain model, but not by the continuous one. The phase of $Z_{o,v}(z)$, however, significantly diverges from the identified response. Besides, there is a considerable mismatch in the magnitude of $Z_{o,v}(z)$. The continuous model, on the other hand, presents a smoother behavior regarding both the magnitude and phase. Even though neither the anti-resonance nor the phase shifts are accurately modeled by $Z_{o,v}(s)$, it represents better the system and will be used for the following analyses.

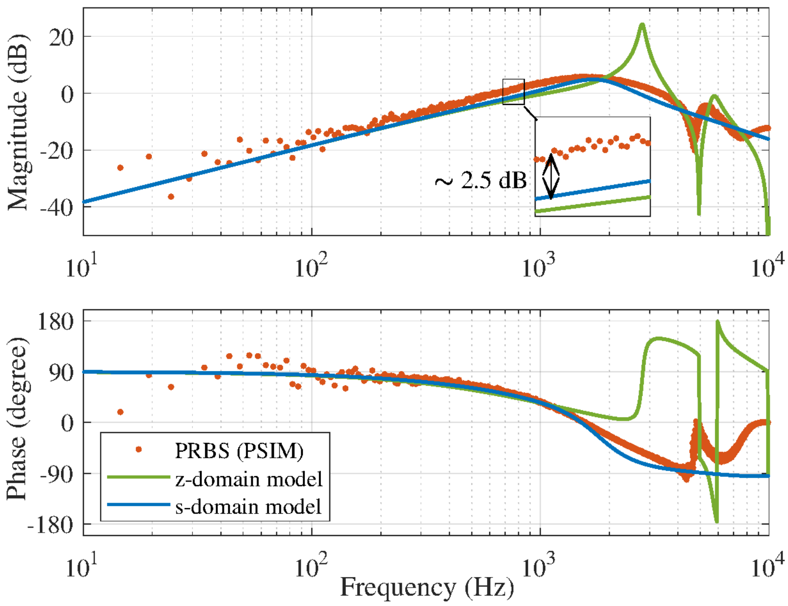

Figure 5.5 – Complete DB-GFI impedance model ($Z_{o,v}$) frequency response.

Generally speaking, the DB-GFI impedance presents an inductive behavior in the low-frequency range, equivalent to an inductance of approximately 200 µH for the converter parameters in Table 4.1. Also, the continuous model suggests that the impedance is passive for all the frequency range, since it is constrained within $-90°$ and $90°$. However, both the PRBS identification and the discrete model suggest the existence of nonpassive regions in the high-frequency region, where the phase jumps are observed.

5.1.3 Effect of Parameter Mismatch

This section explores the effects of parameter mismatches on the DB-GFI impedance models, analyzing the influence of L^m and C^m over both control loops. In all analysis, the continuous models will be used.

Figure 5.6 presents the results concerning the current loop, showing the frequency response of $G_i(s)$ and $Z_{o,i}(s)$ for different mismatch values of L^m with respect to the real inductance value, L. Looking at the closed-loop transfer function (Figure 5.6a), the model indicates a bandwidth of approximately 2.96 kHz when no mismatch is present. For an underestimation of the inductor value ($L > L^m$), the bandwidth reduces, whereas mismatches on the other direction ($L < L^m$) cause a bandwidth increase at the expense of a more accentuated resonance at its vicinity. This result is compatible with the internal stability analysis carried out in section 4.2.3, which concluded that the system moves toward instability when L^m increases with respect to the real value.

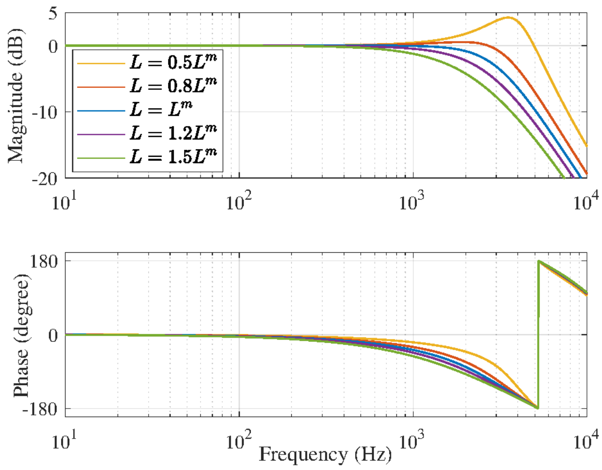

(a) G_i (4.11)

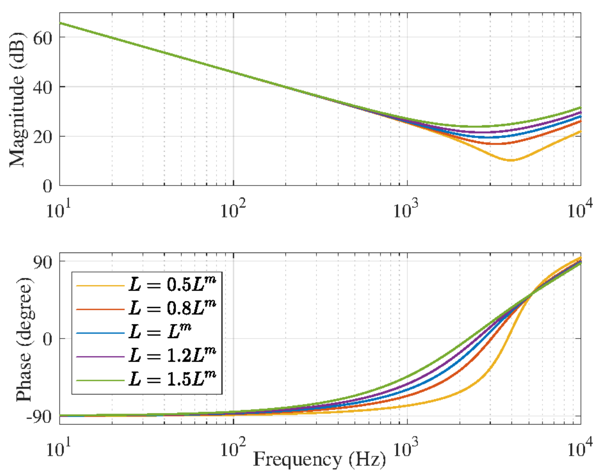

(b) $Z_{o,i}$ (5.1)

Figure 5.6 – Effect of inductance parameter (L^m) mismatch on (a) the closed-loop transfer function and (b) the impedance for the current loop.

The low-frequency impedance shape is not considerably affected by L^m, as shown in Figure 5.6b. Only for frequencies above 1 kHz the mismatch is noticeable on the magnitude although the phase is visibly affected from 100 Hz on. Nevertheless, the impedance remains passive for all the frequency range analyzed, according to this model. Similar to the effect on $G_i(s)$, the impedance is more degraded for overestimations of the inductance value ($L < L^m$), since the magnitude considerably drops for high frequencies, which is not desirable for a current source.

Concerning the voltage loop, both L^m and C^m have to be analyzed. Figure 5.7 presents the influence of the inductance parameter over $G_v(s)$ and $Z_{o,v}(s)$. Even though this parameter regards only the current-loop equations, the mismatch impacts the outer loop as well. As shown in Figure 5.7a, a mismatch in L^m affects G_v in a similar way as it did for G_i—reducing the bandwidth for $L > L^m$, and increasing the bandwidth at the expense of a more undamped system for $L < L^m$. It is important to comment that the voltage reference has only a 60 Hz component, such that the resonant effect starting at approximately 200 Hz is not supposed to represent a problem for the system. Nevertheless, in case of any disturbance fed back into the system having frequencies within the resonance range, oscillations may appear at the output.

Regarding the impedance $Z_{o,v}$, an underestimation of the inductance value ($L > L^m$) shifts the resonance to the left, increasing the impedance magnitude in a wide frequency range—which is not desirable for a voltage source. The opposite occurs for $L < L^m$; however, a misconception must be avoided. Even if the impedance magnitude

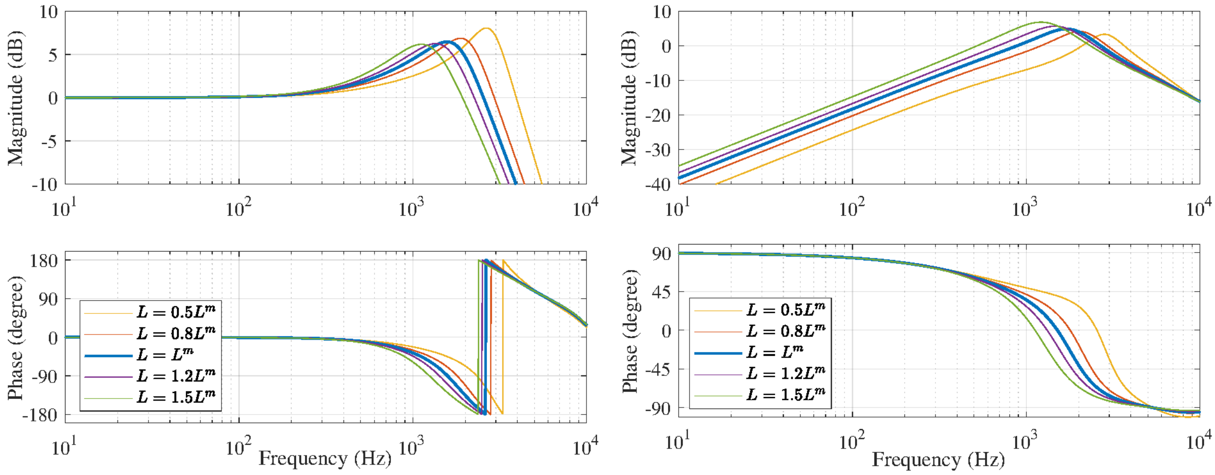

(a) G_v (5.17) (b) $Z_{o,v}$ (5.16)

Figure 5.7 – Effect of inductance parameter (L^m) mismatch on (a) the closed-loop transfer function and (b) the impedance for the voltage loop.

decreases, this is accompanied by an increase of the resonance in G_v. Thus, reducing the output impedance does not necessarily imply a controller performance improvement.

In Figure 5.8, the influence of the parameter C^m is presented. As for the previous cases, an overestimation of the capacitive value reduces the system's damping, as can be visualized in Figure 5.8a. The impedance $Z_{o,v}(s)$ is almost not affected for low frequencies, specially concerning its magnitude. Near the resonance, however, the mismatch effect is more visible. An overestimation of the capacitance leads to a more pronounced resonance as well. It is important to emphasize that—within the mismatch range analyzed—neither L^m nor C^m took the impedance out of the passive region.

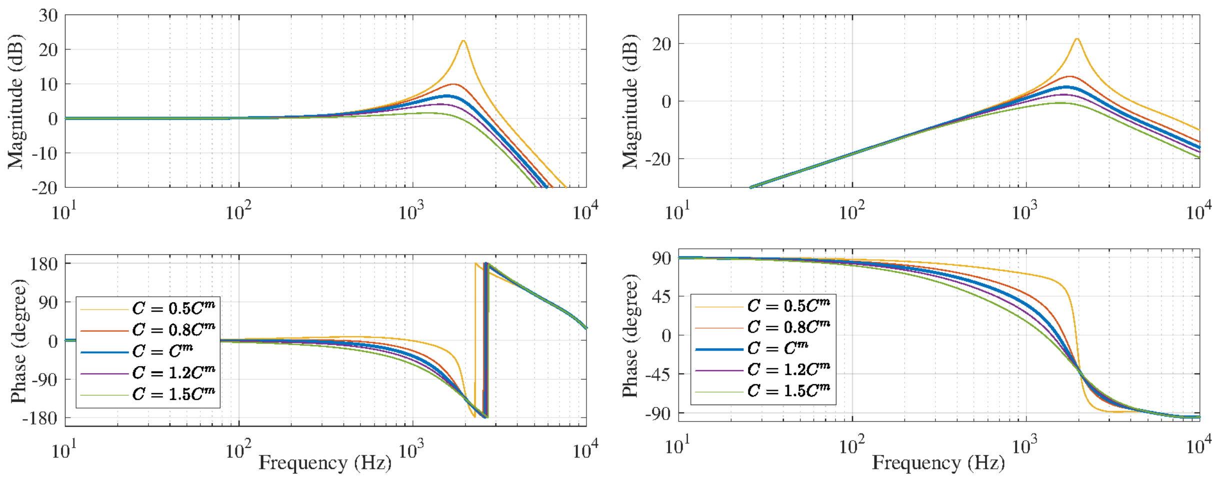

(a) G_v (5.17) (b) $Z_{o,v}$ (5.16)

Figure 5.8 – Effect of capacitance parameter (C^m) mismatch on (a) the closed-loop transfer function and (b) the impedance for the voltage loop.

5.2 Impedance Measurement

The DB-GFI impedance was experimentally measured using the Active Front Rectifier (AFR) presented in section 3.6, following the same procedure as for the identification of Z_{test}. The converters operated as in an islanded system—with the GFI forming the grid for the AFR. For these tests, the AFR's EMI filter was removed, since high-frequency interactions between both converters were observed when the filter was used. More details on that can be found in Appendix C.

Since the GFI impedance is the one to be measured, the disturbance must be injected by the AFR. The PRBS design parameters used in this experiment are listed in Table 5.1. As in Chapter 3, a 10-bit PBRS is generated at the AFR switching frequency, 24 kHz. In this case, however, 100 PRBS periods are used instead of only eight. This choice is for enabling a more accurate measurement, since the GFI impedance magnitude is supposed to be low, which undermine the identification SNR. Indeed, the small impedance makes the GFI voltage more immune to current disturbances. Each PRBS period is 42.63 ms long, so the total injection takes 4.26 s. As this experiment is an *offline* identification in a well-behaved system, whose results will be used only for comparison with the theoretical expectations, the injection duration must not be a matter of concern.

Table 5.1 – PRBS parameters for DB-GFI impedance identification

Generation frequency (f_0)	24 kHz
Number of bits (N)	10
Sequence length (M)	1023
Number of periods/acquisitions (P)	100
Amplitude (e)	10% (with respect to the modulator)

Figure 5.9 shows the interconnected system voltage and current prior to and during the PRBS injection. The AFR operates at approximately half rated power (560 W). When the PRBS is turned on, the current becomes noticeably disturbed, with ripples reaching amplitudes of 5 A. Even though this disturbance may be significant for the AFR, the GFI voltage is barely affected. As explained in Chapter 3, there is a trade-off between the PRBS amplitude and the number of periods in use, since either increasing the amplitude or the number of periods (P) improve the SNR of the process. Hence, more periods could be used, keeping the same identification accuracy with a lower disturbance amplitude. The selected amplitude and P are not necessarily the optimal choice; nevertheless, the values presented in Table 5.1 will be kept for the analysis.

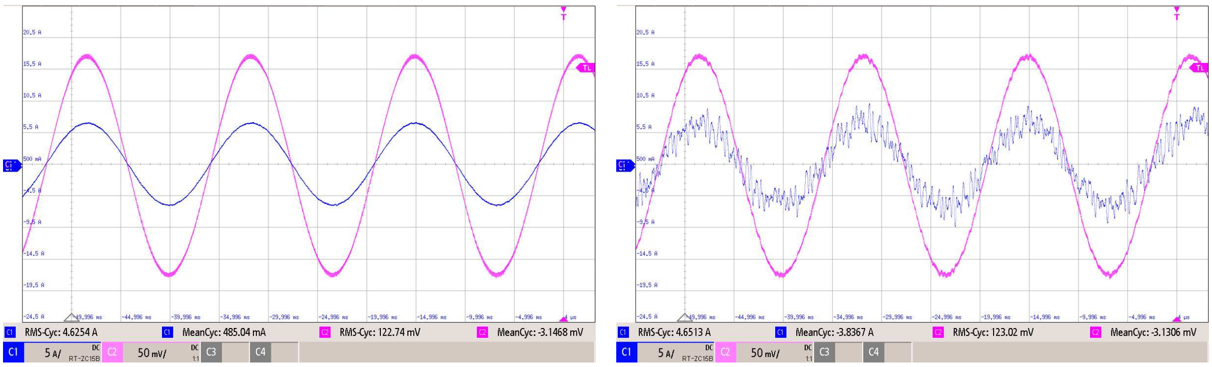

(a) (b)

Figure 5.9 – Voltage (in pink) formed by the GFI and current (in blue) drained by the AFR, (a) without and (b) with PRBS injection.

The identified impedance is contrasted with the model $Z_{o,v}(s)$ in Figure 5.10. For the post-treatment, the FIR method, tuned to the fundamental component only, was used. As can be seen, the experimental result considerably diverges from the model—the resonance presents a higher damping and, for low frequencies, a resistive behavior is dominant in lieu of the expected inductive characteristic, since the phase approaches zero and the magnitude is roughly flat. The identification presents a good resolution up to approximately 5 kHz, where the anti-resonance (previously shown in Figure 5.5) is located. Above this frequency, the PRBS energy was not enough to overcome the noise of the process. This effect was expected based on the results presented in Chapter 3. At 60 Hz, the measured impedance is of approximately -5 dB ($0.56\,\Omega$), which corresponds to the estimated value in section 4.4.1 based on the voltage drop associated with the resistive load.

The gap between the model and the experimental result can be explained by some nonidealities that have not been included in the model so far. As discussed in the previous section, parameters mismatch affect the impedance shape; yet, other characteristics may significantly impact it as well. The low-frequency resistive behavior, for instance, can be explained by the series resistance of the inductor. Figure 5.11a shows what happens to $Z_{o,v}(s)$ when a series resistance (R_L) is included in the inductor impedance (Z_L). Note that the impedance becomes more resistive for higher values of R_L, reaching values similar to what was observed in the experimental result. The capacitor series resistance (R_C) also plays an important role, but for high-frequencies, as shown in Figure 5.11b. Remark that the model suggests that the DB-GFI impedance can even become nonpassive, with the phase exceeding 90°, for high R_C values. The effect due to this resistance was not observed in the identified response, though.

The nonidealities were included into the model in order to approximate its frequency response to the identification result. With $R_L = 1.7\,\Omega$, and mismatches of 20%

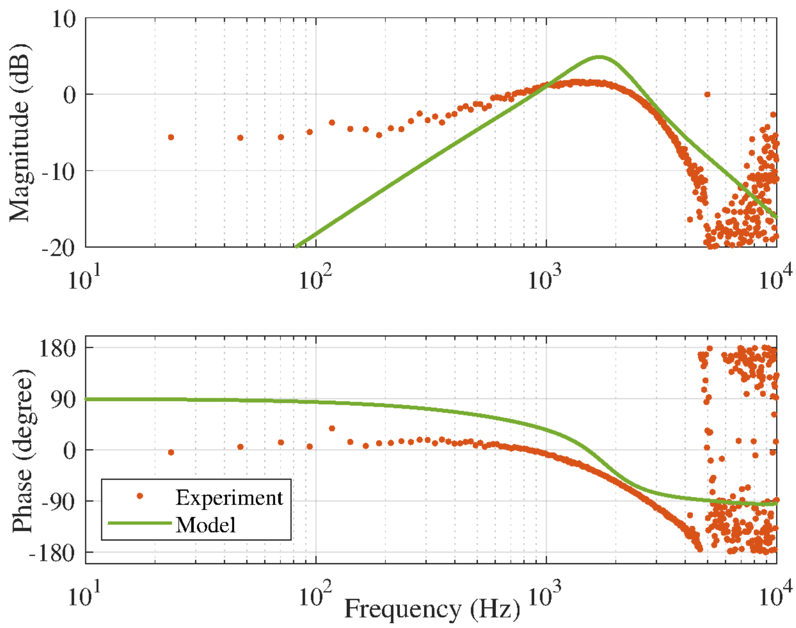

Figure 5.10 – DB-GFI impedance obtained via experimental measurement in contrast with the expected result.

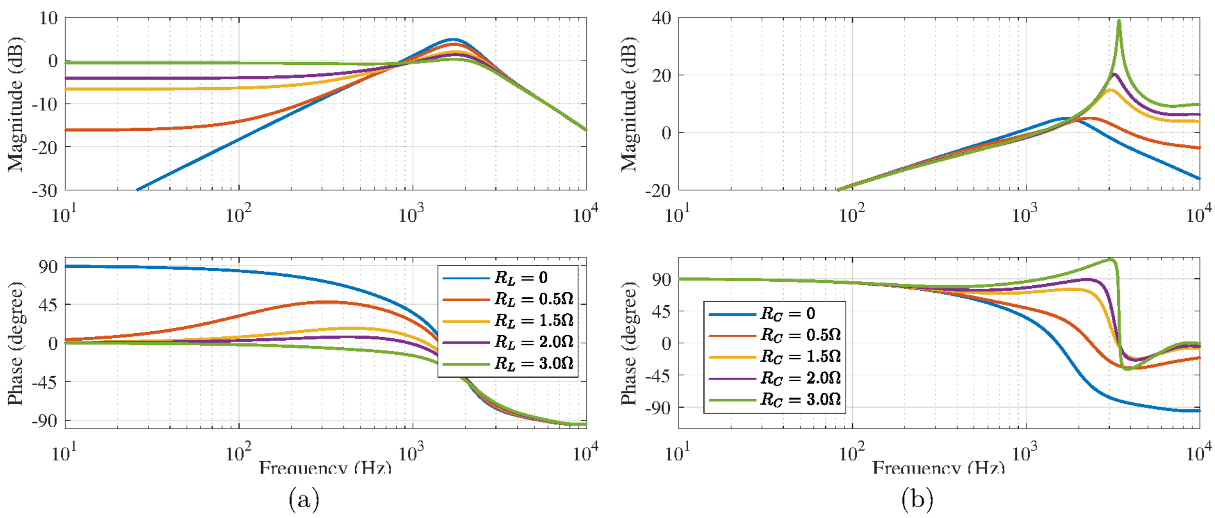

Figure 5.11 – Effect of (a) the inductor series resistance and (b) the capacitor series resistance on the GFI impedance.

in the inductance ($L = 1.2L^m$) and 7% in the capacitance ($C = 1.07C^m$), the model fits satisfactorily the experimental result, as depicted in Figure 5.12. From this results, it is possible to infer that the real inductance value is, approximately, 750 µH instead of 625 µH, and that the capacitor is of 112 µF in lieu of 105 µF. The capacitance and inductance divergence can be explained by the constructive characteristics of the components. It is worthy pointing out that uncertainties concerning the gains of the voltage and current sensors also affect the output impedance as the inductor or capacitance mismatch do. Although these gains have been hidden in the analytical analyses throughout this work, they have to be known for the practical implementation of the controller. If mismatches exist, effects similar to those caused by the inductor and capacitor mismatch would be observed. Thus, part of the 20% and 7% mismatches estimated for the inductance and capacitance, respectively, may be due to the sensing and conditioning system. Anyhow, the most important effect observed is due to the inductor series resistance, estimated as $1.7\,\Omega$. Actually, this resistance could represent not only the inductor series resistance, but any resistive effect in the switching loop, which includes the nonidealities associated with the transistors, wiring, connections, for instance. Indeed, the resistance of the inductor itself was measured as approximately $10\,\mathrm{m}\Omega$, which is far from the $1.7\,\Omega$ estimation. This suggests that the others parasitic effects are of more relevance than the inductor resistance itself. Nevertheless, an inductor series resistance models well the observed effect over the impedance shape. Therefore, the terms R_L and *inductor resistance* will be kept to refer to all parasitic, resistive-like effect in the switching loop.

This parasitic resistance only impacts the GFI impedance because it is not modeled within the DB control equations. In the next section, it will be shown that, if R_L is taken into account, the controller manages to compensate for its effect.

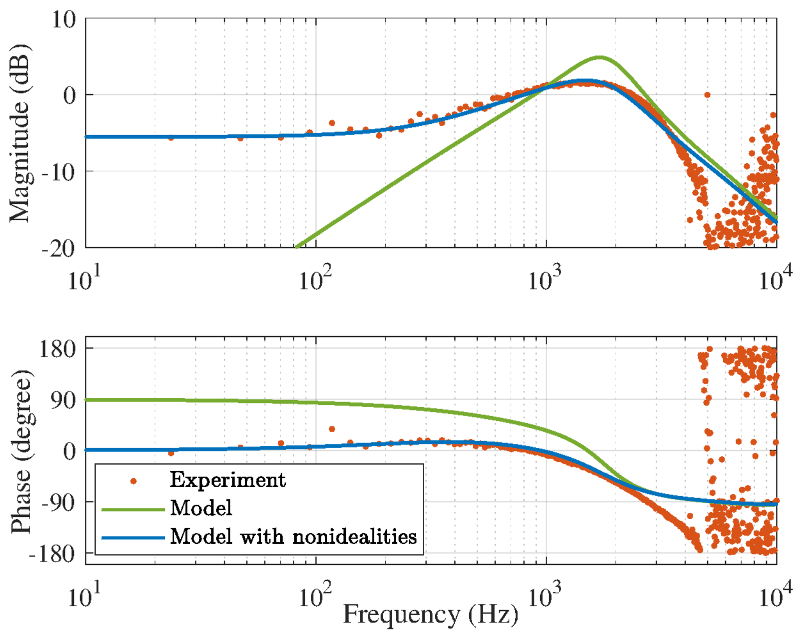

Figure 5.12 – DB-GFI impedance obtained via experimental measurement in contrast with the model including nonidealities ($R_L = 1.7\,\Omega$, $L = 1.2L^m$, and $C = 1.07C^m$).

Before presenting the new controller version, however, the impact of the mismatch of L^m and C^m is experimentally investigated. Figure 5.13 shows the identified DB-GFI impedance for different mismatch scenarios. The frequency content above 5 kHz, in which the identification does not have good resolution, was omitted for clearness. The results are contrasted with the adjusted model, including the nonidealities. Even though, for some cases, the experimental result does not perfectly match the model within certain frequency ranges, the impedance behaves as expected by the results previously presented in section 5.1.3 for both L^m and C^m mismatch types.

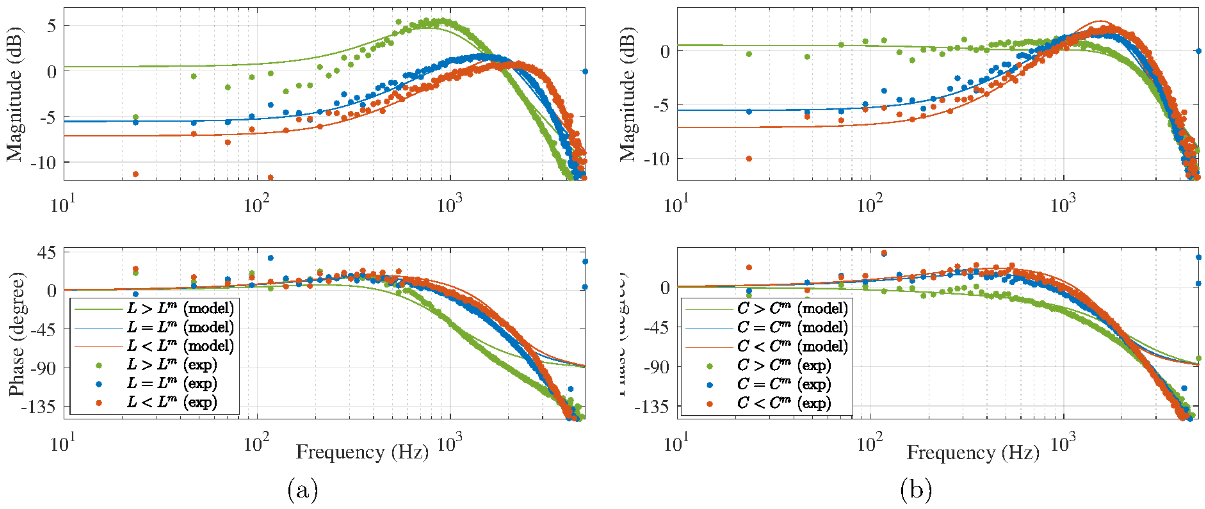

Figure 5.13 – Experimental evaluation of the parameter mismatch effect for (a) L^m and (b) C^m.

5.3 Revisited Deadbeat Control Version

As discussed in the previous section, the inductor series resistance plays an important role in the DB performance. In this section, a revisited version of the DB controller (R-DB), taking into account the presence of R_L, is introduced. Since the inductor impedance only regards the current loop, the outer loop is kept unchanged. As aforementioned, it is important to emphasize that, although it has been considered as the inductor resistance, R_L may represent the effect of any resistance in the switching loop.

Equation (4.1) can be rewritten as

$$i_L(k+1) = \left[1 - \frac{R_L}{L f_{sw}}\right] i_L(k) + \frac{1}{L \cdot f_{sw}} [v_{inv}(k) - v_o(k)], \tag{5.18}$$

such that the new DB equation for the inner loop becomes

$$\begin{aligned} m(k+1) = -\left[1 - \frac{R_L^m}{L f_{sw}}\right] m(k) + \frac{1}{V_{dc}^m} \left[1 - \frac{R_L^m}{L f_{sw}}\right] v_o(k) \\ + \frac{L f_{sw}}{V_{dc}} \left\{ i_{ref}(k) - \left[1 - \frac{R_L^m}{L f_{sw}}\right]^2 i_L(k) \right\}, \end{aligned} \tag{5.19}$$

instead of (4.5). Note that R_L was substituted by R_L^m, indicating that it represents a parameter of the model, which—as for L^m and C^m—may differ from the real resistance value. When $R_L^m = 0$, the traditional DB equation is retrieved.

The new control block-diagram is presented in Figure 5.14. The impedance model of the DB-GFI can be obtained as done in section 5.1, with no additional difficulty, by using the revisited versions of $G^{v_o}_{dist}$ and G_i shown in the diagram.

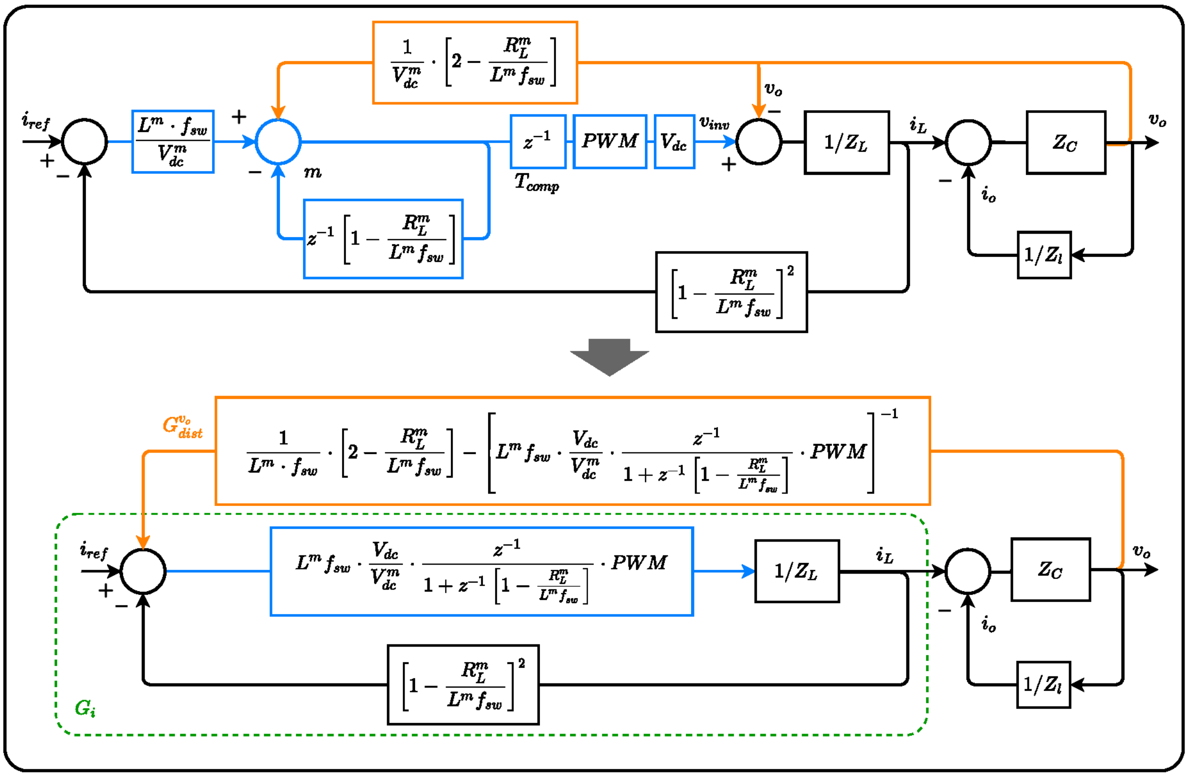

Figure 5.14 – Revisited DB current control diagram.

Since R^m_L represents a new control parameter, it is important to analyze the effect of any mismatch on the final closed-loop transfer function (G_v) and on the R-DB-GFI impedance ($Z_{o,v}$). Figure 5.15 shows the respective frequency responses considering different mismatch levels. It is worthy pointing out that when R^m_L perfectly matches the real R_L value, both G_v and $Z_{o,v}$ correspond to the traditional, ideal DB model, as if the inductor series resistance was null. Thus, as desired, by including R_L in the DB equations, the controller is able to compensate for its influence. Underestimations of the series resistance ($R_L > R^m_L$) dampen the resonance present in G_v while making the impedance more resistive. On the contrary, overestimating R_L ($R_L < R^m_L$) intensifies the resonance in G_v. Also, the magnitude of the impedance increases for low frequencies, becoming similar to a resistive behavior; however, the phase approaches 180° instead of 0°. Therefore, the impedance presents a negative resistance characteristic in this case, out of the passive region. Hence, it is recommended not to use very high values of R^m_L in order to avoid exceeding the real value of R_L. An underestimation is preferable over an overestimation of this parameter.

In comparison with the traditional DB, the revisited version exhibits a lower impedance for lower frequencies even upon R^m_L mismatch. Figure 5.16 presents the ex-

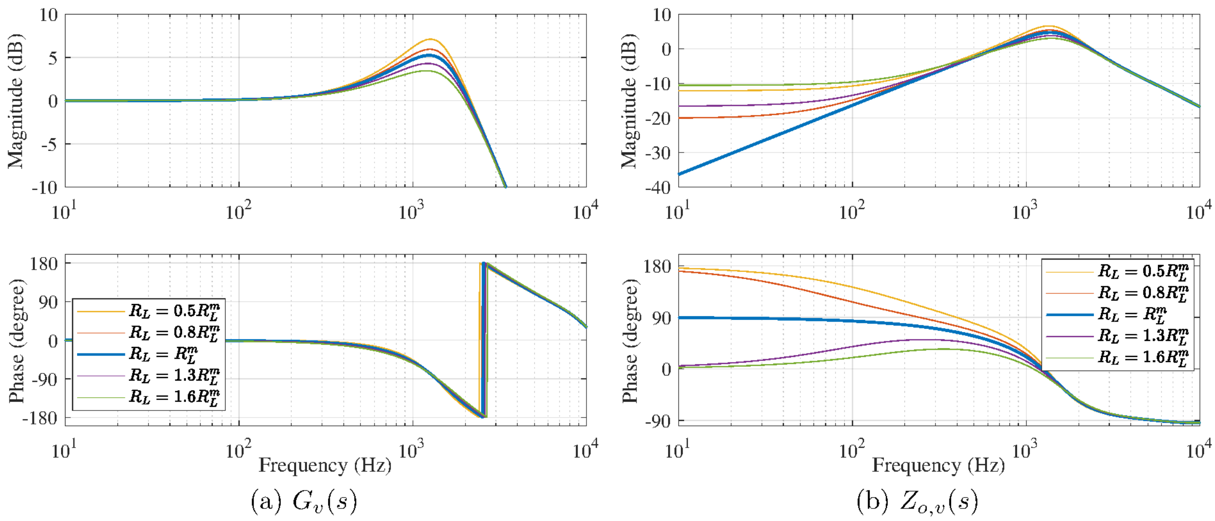

Figure 5.15 – Effect of inductance series resistance parameter (R_L^m) mismatch on the R-DB-GFI (a) closed-loop transfer function and (b) impedance.

perimental measurement of the R-DB-GFI impedance for different values of R_L^m. The case in which $R_L^m = 0$ is equivalent to the traditional DB version. In Figure 5.16a, the impedance for all tested values of R_L^m are plotted together whereas from Figure 5.16b to 5.16d each measurement is compared with the respective response expected by the analytical model. Again, the spectral content above 5 kHz was omitted for clarity. Note that the measured impedance for $R_L^m = 1.7\,\Omega$ satisfactorily correlates with the expected inductive impedance behavior, suggesting that the real value of the series resistance is, indeed, very close to $1.7\,\Omega$. For lower values of R_L^m, the impedance changes in accordance with the R_L^m-mismatch analysis. Even for $R_L^m = 0.5\,\Omega$, which corresponds to approximately one third of the estimated R_L value, the converter's impedance is lower than for the traditional DB ($R_L^m = 0$) in the low-frequency range. Note, however, that from approximately 700 Hz on, the impedance magnitude increases with R_L^m. Thus, for frequencies near the impedance resonance, the magnitude for the tradition DB is lower than for the revisited version. Nevertheless, the impedance reduction for low-frequencies may compensate for this high-frequency increase.

5.3.1 Performance Evaluation

The R-DB-GFI performance was evaluated for the nonlinear load with capacitive filter, as done in section 4.4.2 for the traditional DB. The obtained waveforms are show in Figure 5.17 for R_L^m equal to $0.5\,\Omega$, $1\,\Omega$, $1.7\,\Omega$, and $2.5\,\Omega$. One may notice the asymmetry between the positive and negative current cycles. This sort of phenomena can either be caused by a voltage dc level or by even-order voltage harmonics. Since the voltage mean values measured by the oscilloscope do not exceed 1 V, the asymmetry is

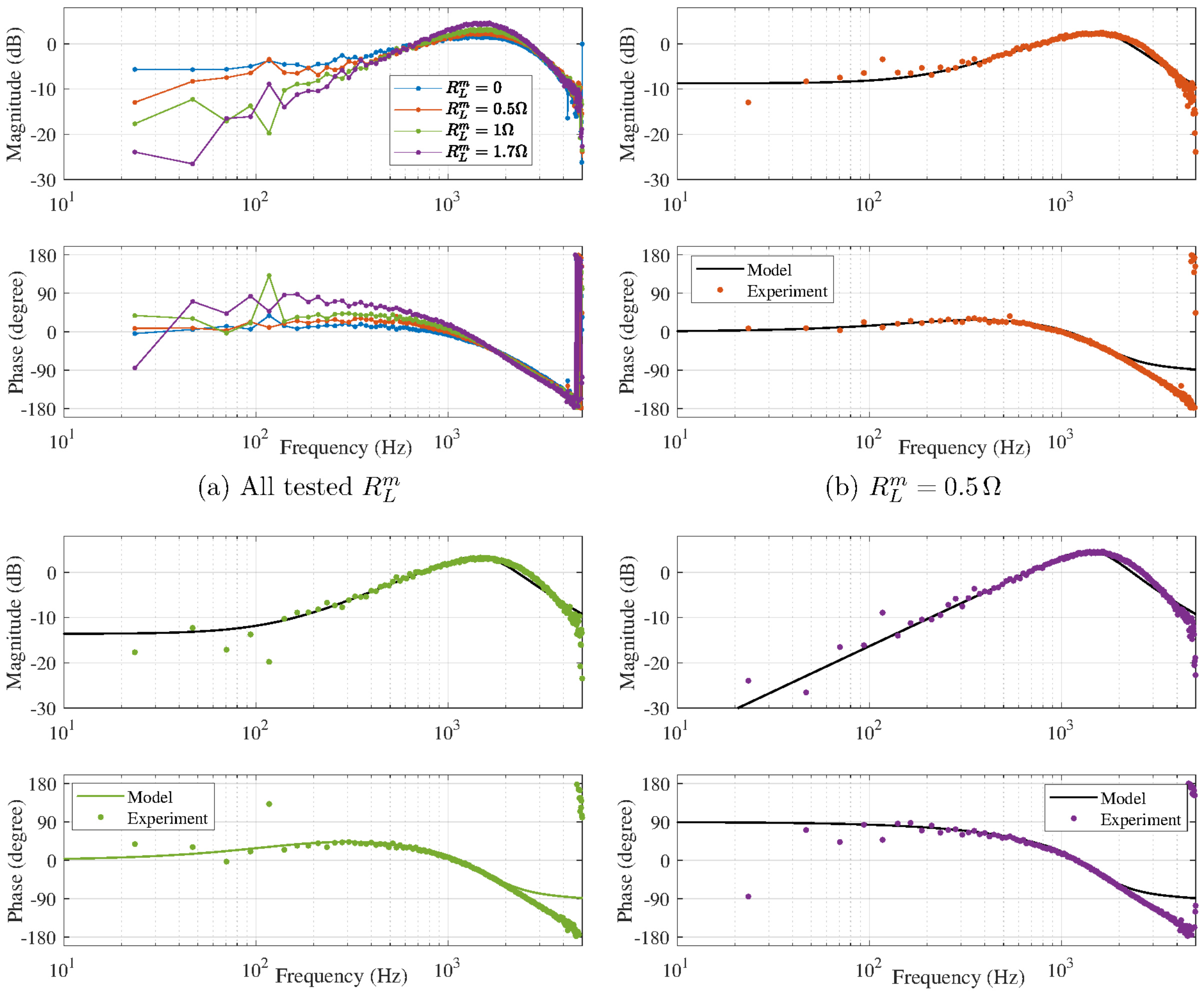

(a) All tested R_L^m (b) $R_L^m = 0.5\,\Omega$

(c) $R_L^m = 1\,\Omega$ (d) $R_L^m = 1.7\,\Omega$

Figure 5.16 – R-DB-GFI impedance measurement for different R_L^m values.

supposed to be due to the even-order harmonics. The diode rectifier with capacitive filter is very sensitive to this kind of asymmetry—even a very low even-harmonic content in the voltage can cause a noticeable current asymmetry, which, in turn, amplify the voltage asymmetry.

For the tested values of R_L^m, the highest asymmetry level was observed for $R_L^m = 2.5\,\Omega$, which is the sole value representing an overestimation of R_L. Similar asymmetry levels were verified for $R_L^m = 1\,\Omega$ and $R_L^m = 1.7\,\Omega$ while, for $R_L^m = 0.5\,\Omega$, it was slightly higher. It is important to comment that this even-order harmonic problem was also present for the traditional DB version in section 4.4.2; yet it appears to be intensified for the R-DB when a high mismatch in R_L^m exist. Nevertheless, the voltage THD for all three cases ($R_L^m = 0.5\,\Omega$, $1\,\Omega$, $1.7\,\Omega$) remained below the 2.37% found for the traditional DB. The new values are listed in Table 5.2, which represented a THD variation of, respectively, -16%, -24%, and -18% with respect to the traditional DB. For $R_L^m = 2.5\,\Omega$ the THD was not even calculated since the controller performance was not considered good

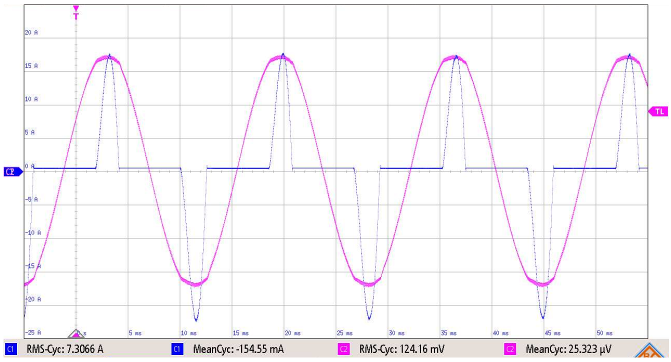

(a) $R_L^m = 0.5\,\Omega$

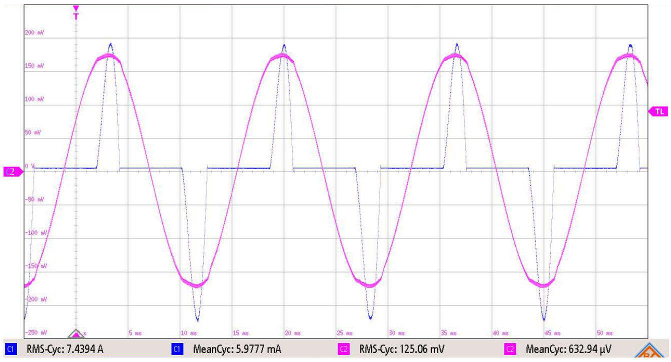

(b) $R_L^m = 1\,\Omega$

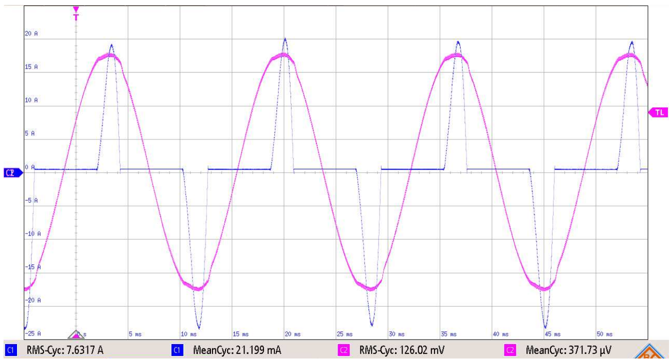

(c) $R_L^m = 1.7\,\Omega$

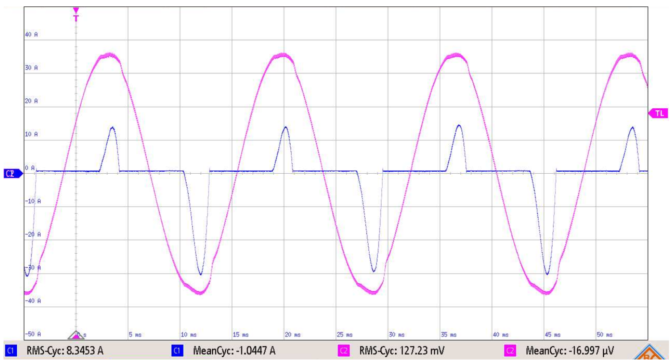

(d) $R_L^m = 2.5\,\Omega$

Figure 5.17 – R-DB-GFI supplying a diode rectifier with capacitive filter for different R_L^m values.

enough due to the pronounced asymmetry.

Table 5.2 – Voltage and current THD for different R_L^m values.

R_L^m	THD v_o	THD i_o
$0.5\,\Omega$	1.99%	118.1%
$1\,\Omega$	1.81%	119.0%
$1.7\,\Omega$	1.93%	121.6%

An interesting results is that the lower THD was not obtained for R_L^m corresponding to the estimated value of $1.7\,\Omega$. Actually, $R_L^m = 1\,\Omega$ represented a better trade-off between the low-frequency impedance reduction and the high-frequency impedance increase provided by the R-DB version. Although the impedance reduces more for low frequencies than it increases near the resonance frequency, the fact that the nonlinear current presented a significant high-frequency content justifies the better performance exhibited by the intermediate R_L^m value. Looking at Table 5.3, in which the harmonic values for all three cases are presented, and comparing with the results previously shown in Table 4.5 (reproduced in Table 5.4) for the traditional version, it is possible to conclude that the R-DB contributed to reducing the distortion mostly up to the fifth harmonic. Remark that the fundamental component increases as R_L^m approaches $1.7\,\Omega$.

It is worthy commenting that this increase in the impedance for high frequencies is expected by the ideal DB controller behavior. When the effect of R_L over the traditional DB was analyzed in Figure 5.11, it could be seen that higher values of R_L increased the low-frequency impedance while reducing it in the region around 2 kHz. Deviating from the DB expected behavior implies reducing the high-frequency impedance at the expense of increasing the low-frequency one. Hence, the R-DB, by trying to retrieve the ideal DB behavior, results in a higher impedance around 2 kHz.

5.4 Partial Conclusions

This section started by presenting the impedance model of the GFI considering only the current-loop and then considering both loops closed. For each case, models were derived in the s- and z-domain. Regarding the current-loop impedance, it was shown that including the half-sample delay due to the PWM was important for improving the model accuracy—avoiding the propagation of the error onto the voltage loop model. The model also revealed the capacitive behavior of the current loop.

For the outer controller, it was demonstrated that the converter ideally presents an inductive behavior up to approximately 1 kHz, with a lower magnitude in the low-frequency range, as desirable for a voltage source. The continuous model, $Z_{o,v}(s)$, repre-

Table 5.3 – R-DB-GFI: Voltage and current harmonics for the nonlinear load test.

Harmonic Order	v_o (V_{rms})	i_o (A_{rms})	Harmonic Order	v_o (V_{rms})	i_o (A_{rms})
$R_L^m = 0.5$					
1	123.979	4.699	2	0.809	0.891
3	1.655	4.058	4	0.184	0.615
5	1.324	2.987	6	0.110	0.284
7	0.772	1.786	8	0.074	0.052
9	0.368	0.781	10	0.074	0.133
11	0.074	0.265	12	0.074	0.125
13	0.257	0.298	14	0.037	0.052
15	0.221	0.254	16	0.000	0.055
17	0.074	0.133	18	0.074	0.085
19	0.074	0.099	20	0.037	0.059
21	0.110	0.114	22	0.000	0.026
23	0.074	0.081	24	0.037	0.044
25	0.037	0.048	26	0.037	0.044
$R_L^m = 1$					
1	124.738	4.758	2	0.737	0.669
3	1.363	4.136	4	0.184	0.467
5	1.252	3.074	6	0.110	0.221
7	0.847	1.886	8	0.037	0.066
9	0.405	0.882	10	0.037	0.114
11	0.110	0.338	12	0.074	0.110
13	0.221	0.327	14	0.000	0.055
15	0.258	0.287	16	0.000	0.048
17	0.110	0.158	18	0.074	0.066
19	0.074	0.110	20	0.037	0.051
21	0.147	0.125	22	0.000	0.029
23	0.110	0.096	24	0.037	0.040
25	0.037	0.059	26	0.037	0.040
$R_L^m = 1.7$					
1	125.732	4.839	2	0.626	0.814
3	1.363	4.224	4	0.221	0.589
5	1.363	3.178	6	0.147	0.317
7	0.994	1.996	8	0.074	0.129
9	0.589	0.994	10	0.037	0.129
11	0.184	0.438	12	0.110	0.125
13	0.258	0.365	14	0.037	0.077
15	0.331	0.309	16	0.037	0.066
17	0.184	0.188	18	0.110	0.081
19	0.110	0.136	20	0.074	0.066
21	0.184	0.144	22	0.037	0.041
23	0.147	0.110	24	0.074	0.048
25	0.074	0.066	26	0.074	0.052

Table 5.4 – Traditional DB: Voltage and current harmonics for the nonlinear load test.

Harmonic order	v_o (V_{rms})	i_o (A_{rms})	Harmonic order	v_o (V_{rms})	i_o (A_{rms})
1	122.9	4.622	2	0.700	0.298
3	2.173	3.981	4	0.111	0.192
5	1.547	2.913	6	0.074	0.070
7	0.810	1.709	8	–	0.022
9	0.258	0.700	10	–	0.062
11	0.074	0.192	12	–	0.044
13	0.258	0.295	14	–	0.004
15	0.184	0.247	16	–	0.026
17	0.037	0.107	18	–	0.037

sented better the converter's impedance although the high-frequency behavior related to the voltage-loop operation rate could not be correctly portrayed.

With the models at hand, the effect of parameter mismatches on the impedance was also explored. Generally speaking, it was seen that overestimating both the inductance and the capacitance values contributes to reducing the damping of the system, which matches the internal stability analysis presented in section 4.2.3. The study of the parameter mismatch impact was also useful in order to adjust the ideal model to the experimentally identified impedance frequency response.

The most important conclusion from this chapter regards the information acquired through the experimental measurement of the DB-GFI impedance. By doing so, it was possible to diagnose and improve the controller. The identification result enlightened the fact that the converter was not operating as it was supposed to—in fact, the measured impedance was dominantly resistive, instead of inductive, for low frequencies. By adding some nonidealities to the impedance model, it was possible to contrast it with the identified response and conclude that the total resistive-like effect in series with the inductor was the major cause of the problem.

From this result, the DB controller was revisited and the inductor series resistance was modeled in the controller equations. The R-DB version is able to completely suppress the influence of R_L as long as the parameter R_L^m perfectly matches the real resistance value. Nevertheless, the experimental results showed that, even upon mismatches, the R-DB-GFI presented a lower impedance magnitude in the low-frequency range when compared to the traditional DB controller, at the expense of a slight increase on the impedance magnitude near the resonance frequency. This improvement could also be noticed through the reduction of the voltage distortion when the GFI was supplying the nonlinear load, reaching a -24% THD reduction with respect to the traditional DB test.

Despite the improvement related to the impedance, it was shown that higher mismatches in R_L^m tend to intensify the even-order harmonics in the output voltage, leading to an asymmetry between the positive and negative cycles. The causes of this issue will be further investigated in future works.

It is also important to highlight the fact that, despite the DB controller being very sensitive regarding noise, the GFI was capable of maintaining a stable voltage even during the PRBS injection. Nevertheless, it is possible that the PRBS itself affects the DB behavior for high frequencies, which may be reflected on the measured impedance as well. This effect may be attenuated, since denoising filters are used; however, it should be further investigated in future work.

6 Stability Analysis of an AFR-GFI System

Until now, the analysis focused on the GFI itself—its control structure and terminal characteristics were thoroughly discussed. In Chapter 5, the GFI impedance was analytically and experimentally explored. This chapter, on the contrary, focus on the stability of an interconnected system composed by two power converters—the R-DB-GFI and the AFR. Such system has appeared in last chapter for the GFI impedance measurement. Now, the focal point is the overall stability assessment of such system applying the IBSC. The chapter starts by the system modeling, presenting a discussion on the analytical MLG. Then the MLG frequency response is experimentally identified, and the results are examined in order to evaluate the feasibility of applying the studied methods to real systems for online stability assessment.

6.1 AFR-GFI System Modeling

As the GFI was modeled in terms of a Thévenin representation, the AFR can be modeled as a Norton equivalent circuit, as shown in Figure 6.1, with a current source in parallel with an output admittance (Y_{AFR}). The interconnection of the AFR and the GFI results in a Z+Y-type system following the reasoning presented in Chapter 2. The stability of such system can be analyzed through the IBSC by looking solely at the MLG, defined as

$$MLG = Z_{o,v} \cdot Y_{AFR} = \frac{Z_{o,v}}{Z_{AFR}}, \tag{6.1}$$

assuming that both converters are individually stable by controller design. Also, as it concerns a Z+Y system, no unstable poles are supposed to be present in the MLG; otherwise, either $Z_{o,v}$ or Y_{AFR} would be unstable, which is not true. This particularity enables the stability to be assessed by applying a simplified version of the NSC—as the one considered by the *forbidden region* criteria (see section 2.1.2)—, which implies that the closed-loop system will be stable if the MLG frequency response avoids encircling the critical point $-1 + j0$ in the complex plane.

Prior to analyzing the MLG, however, the AFR impedance (Z_{AFR}) has to be introduced.

6.1.1 AFR Impedance

As mentioned in previous chapters, the design of the AFR hardware and controller was not done in this project, nor was it developed by the author of this dissertation.

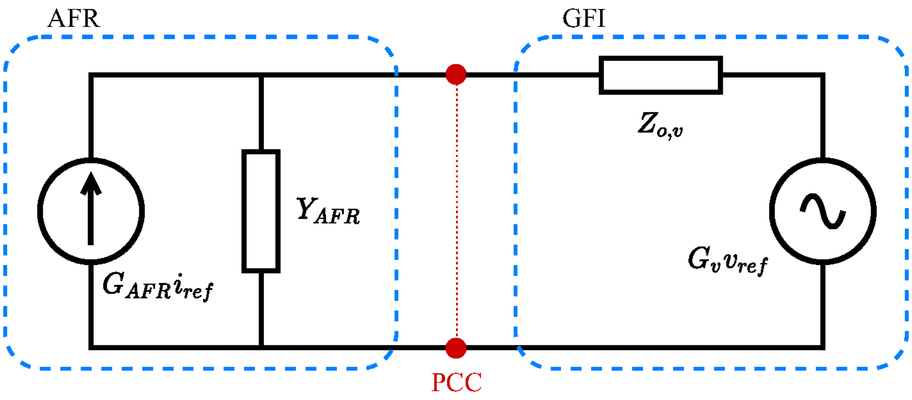

Figure 6.1 – AFR-GFI system representation.

Therefore, only the details about Z_{AFR} that are useful for the present discussion will be given. The reader may find more information in (GUERREIRO, 2020).

Figure 6.2 depicts the analytical frequency response of Z_{AFR}. The effect of the resonant controller—employed for regulating the AFR output current—is noticeable both in the magnitude and the phase. At the resonant frequencies, magnitude peaks are observed, which indicates that the current drained by the AFR presents high immunity against voltage distortions at these frequencies. Similarly, phase jumps occur at the resonant frequencies. It is important to comment that no magnitude peak corresponding to the fundamental component (60 Hz), which is compensated by the resonant controller as well, is observed. This is for the fact that this impedance model includes the effect of the PLL, used by the AFR to generate the current references in phase with the network voltage. Indeed, the PLL establishes a link between the output voltage and the current drained by the AFR at the fundamental frequency, reducing the voltage-immunity of the current. This effect is partly translated as an impedance reduction for low frequencies. Nevertheless, the impedance still exhibits a sufficiently high magnitude—of approximately 35 dB—at 60 Hz, implying a good current regulation at this frequency.

Generally speaking, the impedance presents a capacitive behavior for low frequencies, specially between 100 Hz and 1 kHz, excluding the resonant controller effect. For high frequencies, the LCL filter characteristic is dominant. Figure 6.2 also highlights that Z_{AFR} exhibit a nonpassive behavior for certain frequencies, since the impedance phase tours beyond the passive region delimited by $-90°$ and $90°$. This occurs specially due to the phase jumps caused by the controller in the intermediate frequency range, and due to the PLL dynamics for low frequencies. As discussed in Chapter 2, the impedance passivity is usually sought as it represents a sufficient condition for stability, since the MLG automatically respects the NSC when both impedances composing the ratio are passive. Yet, presenting nonpassive regions does not directly imply instability. Whenever interconnected with other devices in a network having unknown impedance characteris-

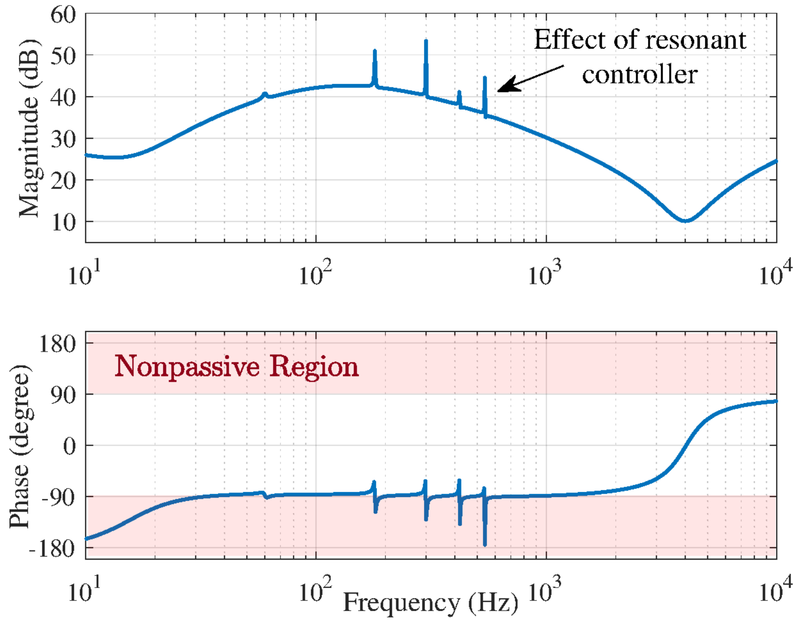

Figure 6.2 – Analytical frequency response of Z_{AFR}.

tics, however, oscillations or even stability issues may arise in these regions, as will be experimentally verified.

6.1.2 Analytical MLG

Figure 6.3 presents the frequency responses of $Z_{o,v}$ and Z_{AFR}. For the GFI, the continuous model of the R-DB version, with no R_L^m mismatch, is considered. The first thing to point out is that the magnitude of the AFR impedance is higher than the GFI one for all the frequency range. This is in accordance with what is expected from a current and a voltage source. Specially for this system, whose one of the impedances exhibits nonpassive regions, having $|Z_{AFR}| >> |Z_{o,v}|$ is of extreme importance. As shown in Figure 6.3b, the MLG phase crosses 180° for the frequencies comprised within the ranges in which Z_{AFR} is not passive. As a matter of fact, if both impedances were completely passive, the MLG would be confined within $-180°$ and 180°, which means that—in the complex plane—the real axis would never be crossed, and, as a consequence, never would be encircled the critical point. In the situation depicted in Figure 6.3b, however, even though the phase crosses 180°, the fact that the MLG magnitude is inferior to 1 (or 0 dB) prevents the critical point from being reached. As the MLG magnitude is considerably far from 0 dB in the 180°-cross, which implies a high gain margin, no undamped oscillations are supposed to be observed at these frequencies. In short, the system is stable.

Figure 6.4 depicts the same curves for another scenario. In this case, the GFI is supplying ten identical AFRs operating in parallel, connected to the same PCC. It is possible since the GFI's power rating is ten times higher than the AFR's. This scenario

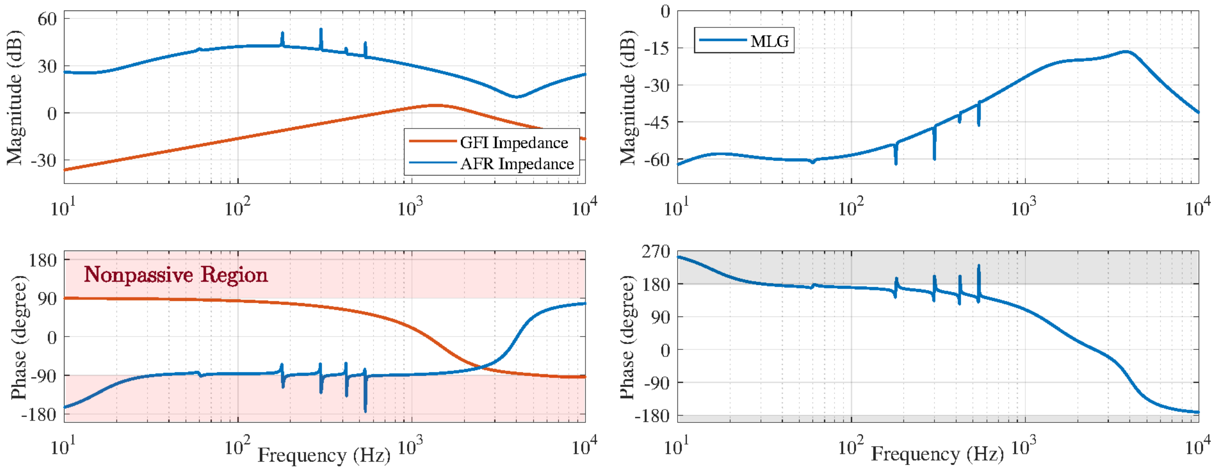

(a) (b)

Figure 6.3 – (a) $Z_{o,v}$ and Z_{AFR}, and (b) MLG frequency responses.

is equivalent to a reduction in $|Z_{AFR}|$ by a factor of ten. As shown in Figure 6.4a, the magnitude of Z_{AFR} was translated $-20\,\mathrm{dB}$ downwards, approaching $Z_{o,v}$ in the region between 1 kHz and 2 kHz. Actually, for certain frequencies, the magnitude of Z_{AFR} even gets lower than the magnitude of the GFI impedance. In terms of MLG, this is translated into a magnitude above 0 dB, as presented in the detail of Figure 6.4b. Nevertheless, note that, when it happens, the MLG phase remains far from $\pm 180°$, which implies a satisfactory phase margin. This is possible for both impedances are passive in this region. Hence, even with a factor-ten reduction in Z_{AFR}, the system remains stable. This example is interesting to illustrate that stability issues are not supposed to arise in frequency ranges within which the impedances are passive, even if the MLG magnitude exceeds 0 dB.

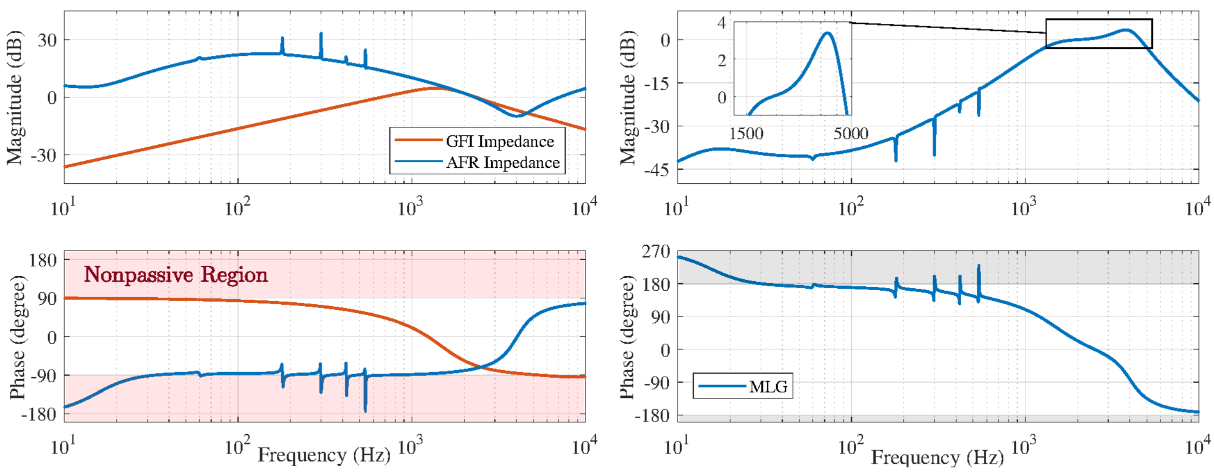

(a) (b)

Figure 6.4 – (a) $Z_{o,v}$ and Z_{AFR}, and (b) MLG frequency responses considering 10 AFRs in parallel

In the next section, it will be shown how the MLG can be experimentally identified, discussing the practical aspects of applying the impedance identification to the stability assessment. Also, the challenges introduced by the presence of extra impedances in the system will be exposed.

6.2 Experimental Stability Assessment

In order for the stability of the AFR-GFI system to be assessed, the MLG frequency response has to be known, which imply knowing the impedances composing it. The most straightforward way of getting this information is using one converter to identify the impedance of the other. As shown in Figure 6.5, the impedance seen by the AFR, herein called Z_{id}^{AFR}, readily corresponds to the GFI impedance $Z_{o,v}$. Similarly, the impedance seen by the GFI, Z_{id}^{GFI}, is given by the AFR impedance Z_{AFR}. Thus, the MLG can be identified as

$$MLG = \frac{Z_{o,v}}{Z_{AFR}} = \frac{Z_{id}^{AFR}}{Z_{id}^{GFI}}. \tag{6.2}$$

Such procedure, however, imposes some requirements for the system if the stability is to be assessed online. First of all, both converters must be able to perform the identification, and only one converter must inject the PRBS at a time in order not to cause spectrum overlap. Moreover, it is desirable that both impedances are identified one just after the other. By doing so, problems related to changes in the system's point of operation are minimized. Therefore, a coordination between the converters is required as well as a communication system enabling the exchange of the identification results so the MLG can be calculated.

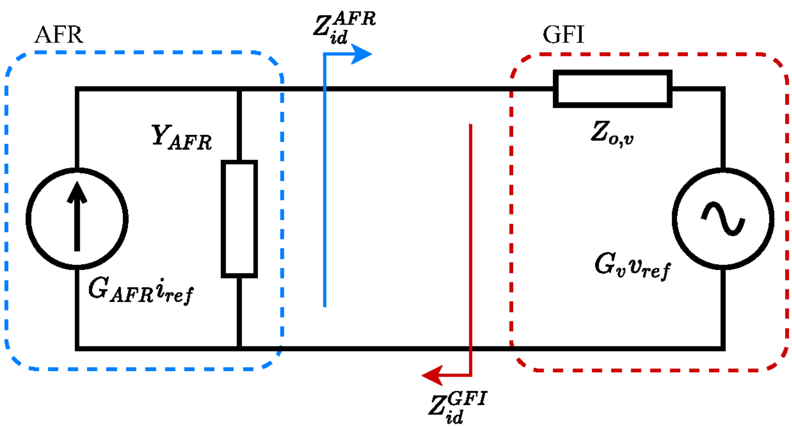

Figure 6.5 – Representation of the impedances that can be identified by the AFR (Z_{id}^{AFR}) and by th GFI (Z_{id}^{GFI}).

In order to reduce the requirements over the system, the stability can be assessed by just one of the converters by making use of impedance models. For instance, one can use the GFI to identify $Z_{id}^{GFI} = Z_{AFR}$ and, instead of obtaining the GFI impedance through the AFR, the analytical model of $Z_{o,v}$ can be used. By doing so, only one converter is in charge of the stability assessment. In lieu of using the analytical model, offline identification results can be utilized as well. In this case, the impedance of the converter in charge of the online identification has to be measured prior to employing it in the application.

The rest of this section is organized as follows. First, the AFR impedance is identified using the GFI and the results are compared with the analytical model. Then the experimental MLG of the AFR-GFI system is calculated using the identified responses. The result is compared with the analytical MLG and with the case in which the impedance model of one of the converters is employed in the MLG calculation. At the end, the impact of impedances located between the GFI and the AFR is investigated.

6.2.1 AFR Impedance Identification

In Chapter 5, the AFR was utilized to identify the GFI impedance. In this section, the opposite is done, following the same procedure. The parameters of the PRBS injected by the GFI are shown in the column "GFI PRBS" of Table 6.1. The generation frequency corresponds to the GFI switching frequency (19.8 kHz), and the number of bits is kept the same as for the previous identifications, producing sequences of same length (1023). Compared to the identification performed by the AFR, the lower generation frequency of the GFI PRBS results in a better frequency resolution (of approximately 19.35 Hz instead of 26.43 Hz), at the expense of a reduced limit up to which the identification is possible. Eight PRBS periods are utilized, which represents a total injection time of approximately 413 ms.

Table 6.1 – PRBS parameters for MLG identification

Parameter	AFR PRBS	GFI PRBS
Generation frequency (f_0)	24 kHz	19.8 kHz
Number of bits (N)	10	10
Sequence length (M)	1023	1023
Number of periods (P)	8	8
Amplitude (e)	10%	15%
Total injection duration	341 ms	413 ms

Figures 6.6a and 6.6b show the voltages and currents during the disturbance injection for two different PRBS amplitude values—6% and 15%, respectively, with respect to the modulator. Note that with 6% the system is not considerably disturbed,

which would imply a poorer SNR. For 15%, the signals are sufficiently excited and the disturbance is kept within safe levels. Hence, $e = 15\%$ is selected.

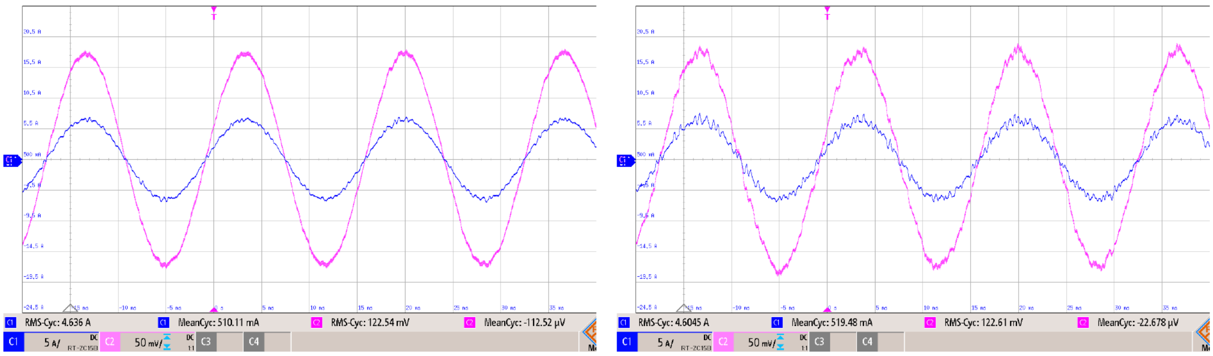

(a) $e = 6\%$ (b) $e = 15\%$

Figure 6.6 – Voltage (in pink) and current (in blue) during PRBS injection via GFI for a disturbance amplitude of (a) 6% and (b) 15% with respect to the modulator.

The identified frequency response is shown in Figure 6.7 along with the analytical model. For data post-treatment, the FIR method tuned at 60 Hz was utilized. As for the results previously presented, the identified response exhibits poor accuracy at high frequencies, specially above 2 kHz. For the decade between 200 Hz and 2 kHz, the identification correlates well with the analytical expectation except for the resonant peaks and phase-jumps. This hides the nonpassive behavior of the impedance at the resonant frequencies and may undermine the stability assessment in certain situations.

When compared to the response in Figure 6.7, the results presented in Chapter 5 for the identification of the DB-GFI impedance exhibited better performance for higher

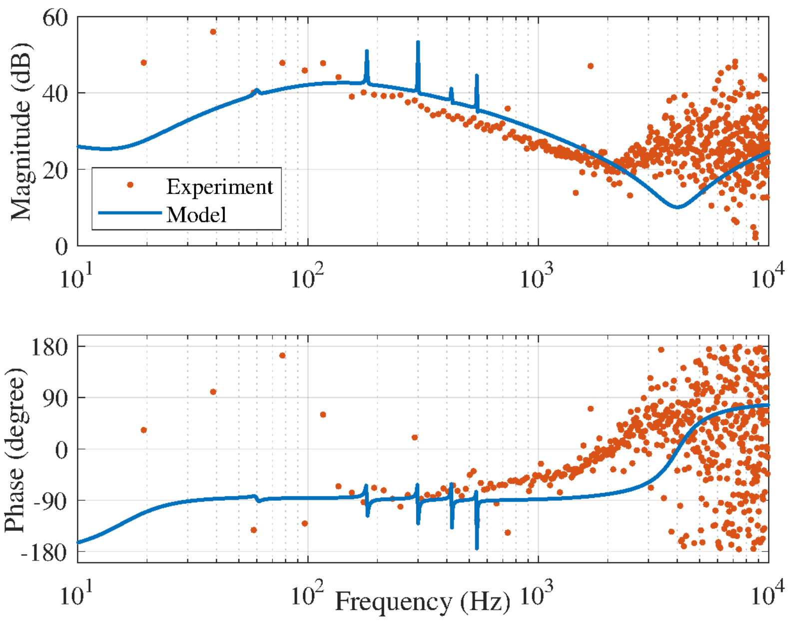

Figure 6.7 – Experimental measurement of Z_{AFR} contrasted with the analytical model.

frequencies, reaching a satisfactory resolution up to approximately 5 kHz. This can be explained as a consequence of two factors—the reduced generation frequency of the GFI PRBS (19.8 kHz against 24 kHz for the AFR), which confines the PRBS energy within a narrower bandwidth, and the controller characteristics. Indeed, part of the energy of the PRBS injected into the modulator will be rejected by the controller itself before reaching the impedance to be identified.

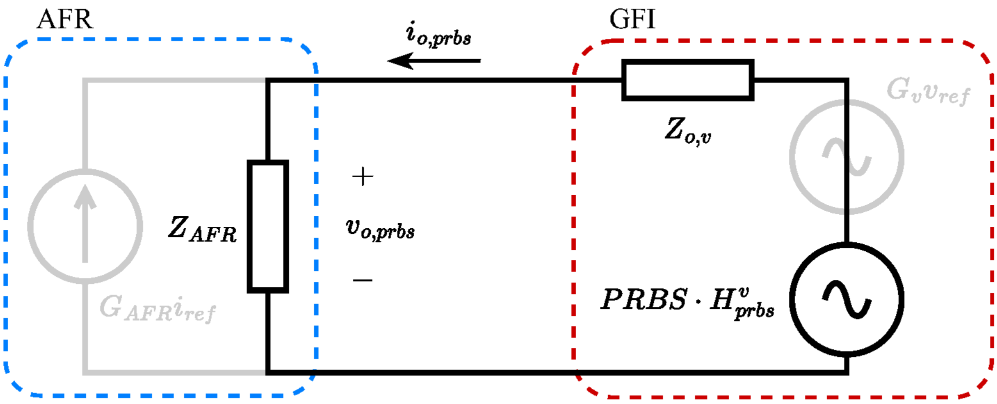

Figure 6.8 – Equivalent circuit for PRBS power analysis.

In order to analyze the influence of the DB controller on the identification, the PRBS injection can be included in the GFI impedance model, as shown in Figure 6.8. Note that a voltage source of magnitude $PRBS \cdot H^v_{prbs}$ was added in series with the previously existing one, $G_v v_{ref}$. The term H^v_{prbs} is for the transfer function between the PRBS signal and the output voltage, calculated as shown in Appendix D. Both current and voltage sources corresponding to the current and voltage references are shaded in Figure 6.8 since the analysis to be carried out concerns only the PRBS input, so the 60 Hz steady-state components are neglected.

Figure 6.9 shows the frequency response of H^v_{prbs}, which represents the effect of the controller and the GFI power stage over the PRBS. As can be observed, the GFI acts as an amplifier for the disturbance, specially for low frequencies. From 100 Hz, the amplification smoothly decreases up to around 1400 Hz, from which the magnitude of H^v_{prbs} plummets. Thus, the DB-GFI does not manage to amplify the disturbance injected into the modulator for all frequencies, which means that only part of the PRBS energy will excite the GFI output voltage.

Looking at the circuit in Figure 6.8, the voltage source value is given by the PRBS filtered by H^v_{prbs}, whose frequency response is depicted in Figure 6.9 as well (yellow curve). Indeed, it is possible to observe that the 15%-amplitude PRBS power spectrum (blue curve) is not sufficiently amplified for high frequencies. Actually, defining whether the amplification is satisfactory or not depends on the noise in the system. If the distur-

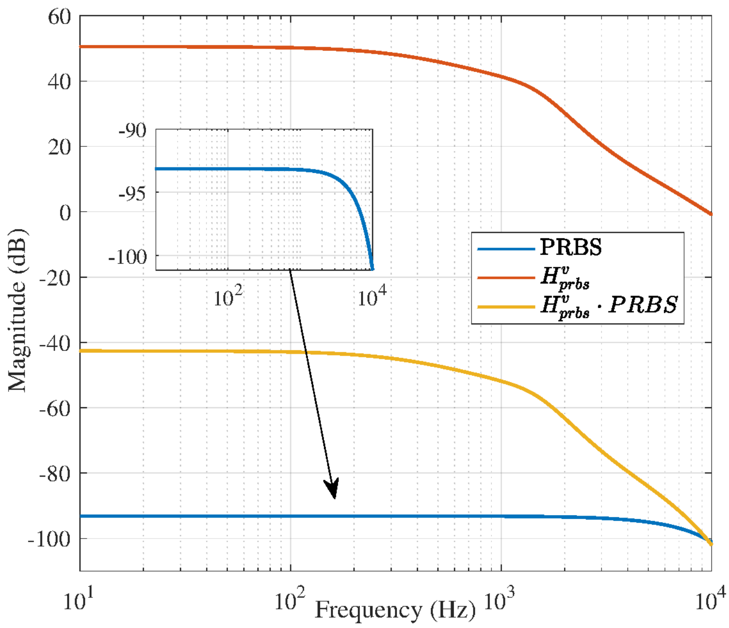

Figure 6.9 – PRBS spectrum (in blue), transfer function between the PRBS and the GFI open-circuit output voltage (H^v_{prbs}, in orange), and the filtered PRBS ($H^v_{prbs} \cdot PRBS$, in yellow).

bance source has enough power to excite the voltages and currents above the noise level, the impedance identification is possible. From the equivalent circuit, the voltage over and the current through the impedance to be identified (Z_{AFR}), respectively given by $v_{o,prbs}$ and $i_{o,prbs}$, can be analytically calculated as the models of Z_{AFR} and $Z_{o,v}$ are known. The results are presented in Figure 6.10. These frequency responses correspond to the fraction of the PRBS power that manages to reach $v_{o,prbs}$ and $i_{o,prbs}$. Note in Figure 6.10a that $v_{o,prbs}$ is virtually equal to the voltage source $PRBS \cdot H^v_{prbs}$, since $Z_{o,v}$ is considerably negligible compared to Z_{AFR}. Due to the high value of Z_{AFR}, the current $i_{o,prbs}$ exhibits a very low magnitude, below -65 dB for all frequencies. For the fact that the post-treatment methods rely on both voltage and current measurements, both $v_{o,prbs}$ and $i_{o,prbs}$ must be excited above noise levels. To exemplify, Figure 6.10 also includes a representation of the noise (considered as a white noise), whose level was arbitrarily selected just to illustrate. A noise of approximately -70 dB in the voltage measurement would enable an accurate identification only up to 2 kHz, whereas, for the current measurement, the noise level cannot exceed, roughly, -85 dB in order for the identification to be precise up to the same frequency. Specially for the current constraint, the identification is practically limited to 5 kHz—from this frequency on, unrealistically low noise levels would be required.

This analysis explains why the AFR impedance identification (Figure 6.7) was not accurate for high frequencies. It also explains why the resonant peaks were not correctly identified. As can be seen in Figure 6.10b, very low noise levels would be required for the resonances to be identified. Moreover, it is important to recall that the PRBS

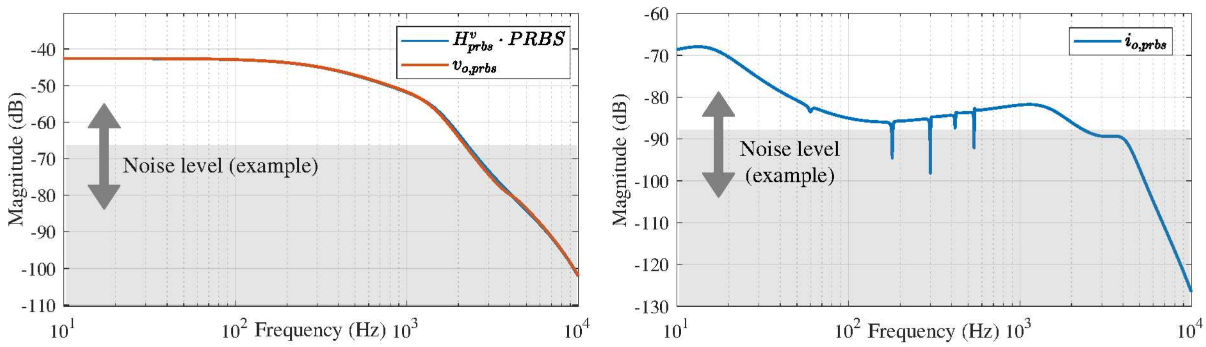

(a) $v_{o,prbs}$ (b) $i_{o,prbs}$

Figure 6.10 – Fraction of the PRBS power managing to excite the (a) output voltage and (b) the output current. An arbitrarily chosen noise level is shown along with the frequency responses.

presents a discrete spectrum, with a certain frequency resolution, although it has been represented as a continuous spectrum in Figure 6.9. As the resonance peaks are narrow, precisely placed at the harmonic frequencies, the PRBS does not necessarily excite these frequencies.

6.2.2 Experimental MLG

The experimental MLG will be calculated in two different ways. The first one considers that both converters are able to perform the identification in a *coordinated* fashion, such that the MLG is given by the ratio of the identified responses, as in (6.2). The MLG corresponding to this scenario will be referred to as MLG_C or *coordinated strategy*. The second one delegates the stability assessment to a *single* converter, which is capable of calculating the MLG by using its own impedance model along with the online measurement of the impedance looking outwards from its terminals. In this work, the GFI will be in charge of this task, since this is the converter under special analysis, whose impedance model was thoroughly discussed. Moreover, as it is the converter responsible for forming the grid, its impedance is less prone to change over time compared to the load's; hence it is preferable to update the information about the load impedance via online measurements. For this scenario, the MLG will be referred to as MLG_S or *single-converter strategy*.

Figure 6.11 presents the identified responses contrasted with the MLG obtained via the analytical model. As expected based on the previous results, the measured response becomes inaccurate for frequencies above 2 kHz. The accuracy is specially limited by the AFR impedance identification performed by the GFI, as commented in the last section. Comparing the MLG_C with the MLG_S, no important difference is noticed. Hence, using the GFI impedance model instead of the identified response provided by the AFR

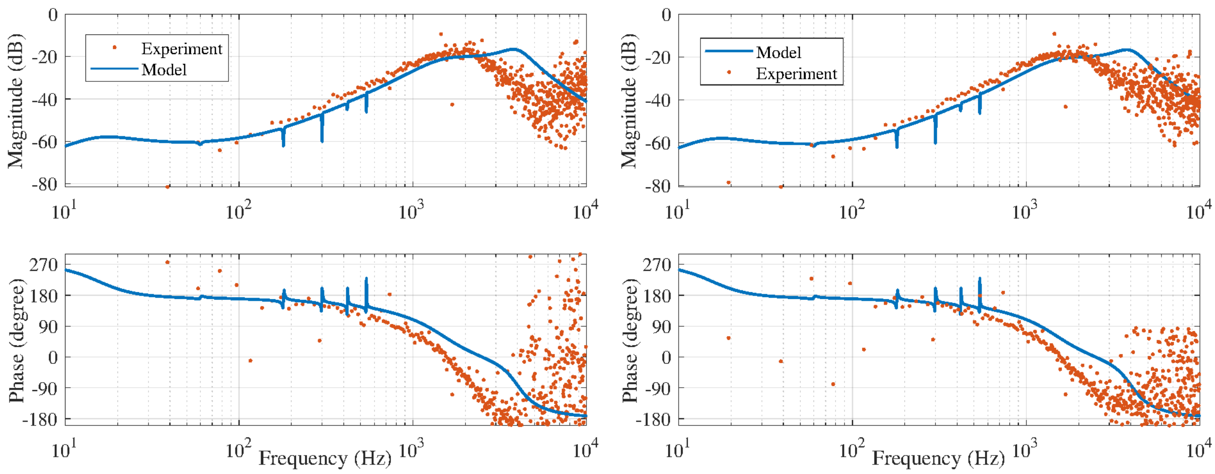

(a) MLG$_C$ (b) MLG$_S$

Figure 6.11 – Experimental identification of the MLG considering (a) a coordination between the converters (MLG$_C$) and (b) that only the GFI is in charge of the stability assessment (MLG$_S$).

produced satisfactory results. Note, however, that it was only possible because the GFI model had been appropriately analyzed and previously corrected based on experimental measurements.

Again, the identification produced a satisfactory result within the decade from 200 Hz to 2 kHz. For lower frequencies, the phase data-points are considerably dispersed. This is assumed to be due to the poor low-frequency resolution in the AFR impedance identification, since this effect was also present in Figure 6.7. While the high-frequency inaccuracy can be explained by the PRBS power analysis, as previously shown, the low-frequency imprecision is an effect of the steady-state component elimination performed in the post-treatment phase, which, in some cases, does not manage to completely suppress the 60 Hz. Despite the nonidealities present in the identified MLG, the stability assessment is not jeopardized in this case study. As a matter of fact, the magnitude of both MLG$_C$ and MLG$_S$ remains bellow 0 dB for all frequencies, so the critical point is not encircled in the complex plane.

6.2.3 Impact of Line Impedance and Passive Load

Until now, the analyses considered that the AFR and the GFI were connected together with no impedances placed between them. These *extra* impedances, however, may introduce some difficulties regarding the stability assessment through identification, as discussed in this section.

Figure 6.12 depicts a situation in which an impedance Z_s is added in series with the GFI and an impedance $Z_p = 1/Y_p$ is placed in parallel with the AFR. Z_s could

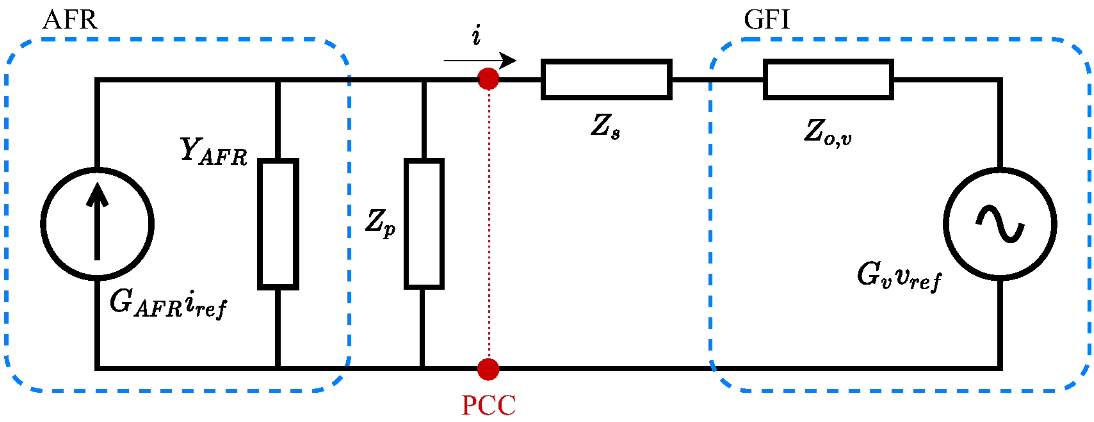

Figure 6.12 – AFR-GFI system representation with series (Z_s) and parallel (Z_p) impedances added.

represent the line impedance while Z_p symbolizes any load connected in parallel with the AFR. In this situation, where all the series impedances are placed at one side of the PCC, and all parallel impedances are located at the other side, no significant change has to be introduced in the development presented in Chapter 2. The definition of the MLG as the product ZY still holds; yet, Z_s and Y_p have to be incorporated into $Z_{o,v}$ and Y_{AFR}, respectively, as in

$$MLG = (Z_{o,v} + Z_s) \cdot (Y_{AFR} + Y_p) = \frac{Z_{o,v} + Z_s}{Z_{AFR}||Z_p}, \tag{6.3}$$

where the symbol $||$ represents the parallel association. As expected, if Z_s and Y_p are negligible, (6.1) is retrieved. For other scenarios, with more complex associations of impedances placed throughout the system, the MLG has to be cautiously redefined.

In this scenario, the stability assessment through identification is affected since the impedances seen by the AFR and by the GFI change; now, the impedances Z_p and Z_s appear in both Z_{id}^{AFR} and Z_{id}^{GFI}, as

$$\begin{cases} Z_{id}^{AFR} & = Z_p||(Z_s + Z_{o,v}) \\ Z_{id}^{GFI} & = Z_s + (Z_p||Z_{AFR}). \end{cases} \tag{6.4}$$

Thus, if the MLG is calculated from the ratio $Z_{id}^{AFR}/Z_{id}^{GFI}$, using the coordinated strategy to obtain MLG$_C$, as if Z_s and Z_p did not exist, the stability analysis may be compromised. As a matter of fact, from (6.4),

$$MLG_C = \frac{Z_{id}^{AFR}}{Z_{id}^{GFI}} = \frac{Z_p||(Z_s + Z_{o,v})}{Z_s + (Z_p||Z_{AFR})}, \tag{6.5}$$

which is different from the actual MLG expressed in (6.3). Depending on the values of Z_s and Z_p, the actual MLG may significantly differ from the identified ratio. Even if the identification is performed only by the GFI—using the single-converter strategy—the

MLG diverges from the real one, since

$$MLG_S = \frac{Z_{o,v}^{model}}{Z_{id}^{GFI}} = \frac{Z_{o,v}^{model}}{Z_s + (Z_p || Z_{AFR})}. \tag{6.6}$$

It is important to note that, as explained in Chapter 2, the MLG-based IBSC depend on the selected PCC. For the MLG$_S$ strategy, since the stability is assessed from the GFI perspective, the PCC should be located at the GFI terminals, and not as depicted in Figure 6.12. By making this change, though, the MLG defined as in (6.3) still holds, since the current i through the PCC is kept the same. Thus, even from the GFI point of view, the MLG of the system is defined as (6.3).

Figure 6.13 shows three different frequency responses for the MLG—the actual MLG, calculated via (6.3), and the responses expected by the coordinated and the single-converter identification strategies, MLG$_C$ and MLG$_S$, calculated as in (6.5) and (6.6), respectively. For all three, the frequency responses were analytically calculated—not identified—using the respective equations. Four different scenarios are considered. In Figure 6.13a, Z_s corresponds to a 50 µH inductor and Z_p to a 1 µF capacitor while, in Figure 6.13b, the capacitor was exchanged for a 10 µF one, keeping the same value for the inductance. In the third and fourth scenario (Figures 6.13c and 6.13d) the inductance presents a higher value of 3 mH. As aforementioned, the series impedance may symbolize the line impedance. In the context of microgrids, where the devices are not placed very far from each other, the line inductance is likely to be in the range of a few tens or hundreds of µH, considering cables that are a few hundreds of meters long. Even though the scenarios with a 3 mH inductor do not represent an usual grid, this value was selected in order to emphasize the impact of non-negligible line impedances, and to enable an experimental verification of instability, as will be shown later. The parallel impedance, in turn, represents any passive load that may be supplied by the GFI as well. As a capacitor, it may represent the EMI filter of eventual PECs in stand-by mode, which typically presents a few µF.

The objective of the analysis presented in Figure 6.13 is to show that, depending on the impedances located between the converters, the MLG assessment through the identification strategies may diverge from the actual MLG of the system. Note that, for the first scenario (Figure 6.13a), both the MLG$_C$ and the MLG$_S$ do not diverge from the actual MLG for frequencies up to approximately 1400 Hz. From this frequency on, however, expressive differences are noticed for the MLG$_S$ strategy. For the second scenario, with a higher capacitance value in Z_p and keeping the inductance value, the same effect is observed, which implies that the accuracy of the MLG$_C$ strategy is almost not affected by the capacitor value (except for very high frequencies). Also, it suggests that the series inductance affects more the MLG$_S$ than it does for the MLG$_C$. Looking at the third and fourth scenarios (Figures 6.13c and 6.13d), it becomes more evident that the single-converter strategy is largely affected by Z_s. In this scenario, both MLG$_C$ and MLG$_S$ strategies considerably diverge from the actual response. Nevertheless, as for the precedent cases, the coordinated strategy correlates better with the actual MLG. In short, if Z_s and Z_p are negligible, both strategies for identifying the MLG are suitable. When the effect of the in-between impedances cannot be neglected, the coordinated identification strategy provides better results, specially because this strategy is less sensitive to the series impedance.

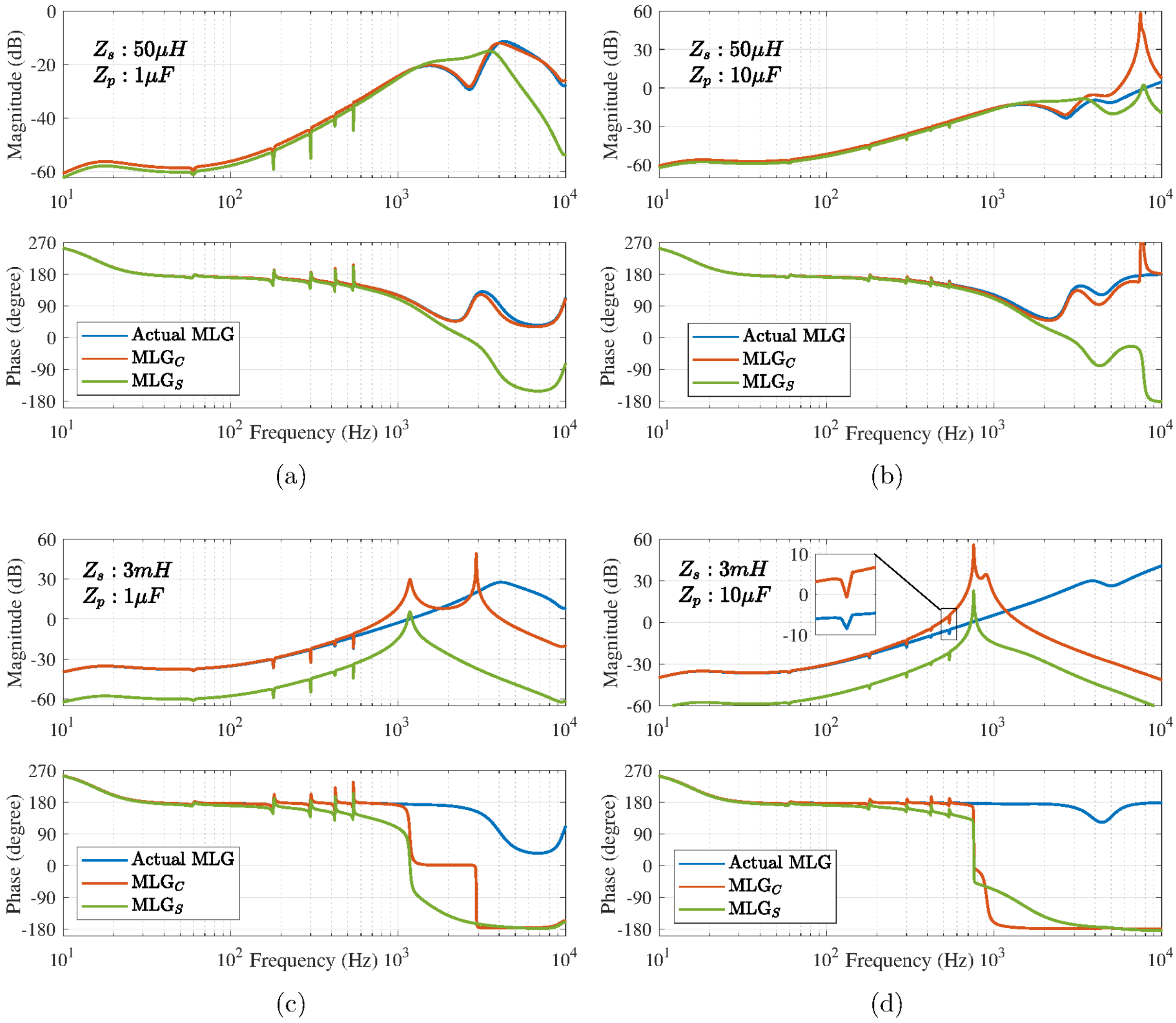

Figure 6.13 – Analytical MLG response (6.3) contrasted with the analytical results provided by the MLG$_C$ (6.5) and MLG$_S$ (6.6) strategies for three different scenarios—(a) Z_s : 50 µH and Z_p : 1 µF, (b) Z_s : 50 µH and Z_p : 10 µF, (c) Z_s : 3 mH and Z_p : 1 µF, and (d) Z_s : 3 mH and Z_p : 10 µF.

Even with the exaggerated value of Z_s in the fourth scenario, the MLG$_C$ is capable of correctly predicting an unstable operation. As shown in the detail in Figure 6.13d, the MLG$_C$ exhibits a low gain margin at 540 Hz, which is the PR-controller resonant frequency corresponding to the 9$^{\text{th}}$ harmonic. Since the phase crosses 180° at this frequency, the system may be subjected to undamped oscillations. This phenomenon was experimentally observed, as shown in Figure 6.14. In the beginning, the GFI is supplying the AFR with no impedances in between. At 500 ms, approximately, the 3 mH inductor and the 10 µF capacitor are added to the system, placed as Z_s and Z_p, respectively. Note that an undamped oscillation is launched and exponentially grows until the AFR current protection is triggered, which occurs at approximately 4.5 s. The frequency of the oscillations matches perfectly the 9$^{\text{th}}$ harmonic (540 Hz), as expected by the analysis. For the other combinations of Z_s and Z_p in Figure 6.13, no instability was observed, as expected by the models.

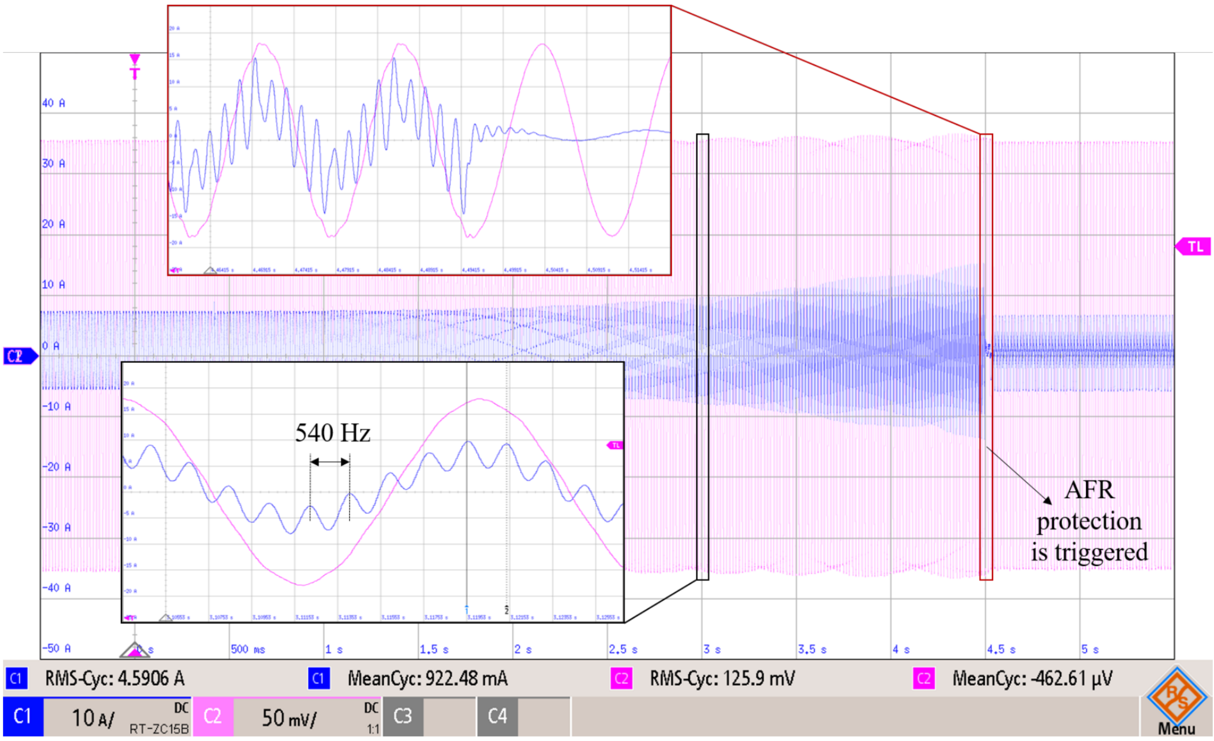

Figure 6.14 – AFI-GFI unstable operation. The GFI output voltage and current are shown in pink and blue, respectively.

It is worthy emphasizing that the unstable scenario reproduced in the experiment is unlikely to happen in a real, isolated microgrid for the parameters and impedance characteristics of the GFI and the AFR under study. As explained, even though the 10 µF capacitor is reasonable to be present in the system, the line impedance is not likely to reach a 3 mH value. Nevertheless, this case study with a magnified inductor is interesting to elucidate the impact of non-negligible line impedances on the MLG identification. Also, since the nonpassive region of the AFR impedance is located in a frequency range where the GFI impedance magnitude is considerably low, such line impedance value was necessary to experimentally verify an unstable operation. Real systems are not immune to this kind of instability, though; depending on the impedance characteristics of the interconnected converters and loads, instabilities may occur even with a negligible line impedance.

6.3 Partial Conclusions

This chapter started by introducing the AFR impedance characteristic, which exhibits nonpassive regions near the PR-controller resonant frequencies and also in the low-frequency region due to the PLL dynamics. The AFR impedance frequency response was subsequently identified by using the GFI as the PRBS source. The identified response presented good accuracy for the frequency range between 200 Hz and 2 kHz, except for the resonant peaks and phase jumps. The frequency limit of 2 kHz—which was inferior compared to the identification performed by the AFR in Chapter 5 (section 5.2) could be explained by two factors—1) the reduced PRBS generation frequency, and 2) the restriction imposed by the R-DB-GFI capability to amplify the PRBS at the GFI terminals. The PRBS power analysis showed that the R-DB controller (along with the converter power stage) was able to amplify the PRBS up to around 1400 Hz with a satisfactory magnitude. By analyzing the fraction of the PRBS energy reaching the output voltage and current used for the impedance identification, it was possible to better understand the 2 kHz accuracy limit and also why the resonant peaks could not be identified. This PRBS power analysis can be extended to any system in order to improve the design of the disturbance.

The MLG was initially analyzed through the theoretical models. It was shown that an unstable operation was unlikely to happen in the regions where both impedances are passive. Even in the 10-AFR scenario, taken as an example, in which the MLG magnitude is above 0 dB for frequencies around 2 kHz, the system remains stable since the nonpassive regions are located well bellow this frequency.

Concerning the MLG identification, two different strategies were discussed—the coordinated (MLG_C) and the single-converter (MLG_S) strategies. Both techniques produced equivalent results in this first scenario, in which the line impedance and passive loads between the converters were neglected. It is important to comment, however, that the identified MLG_S was equivalent to the MLG_C only because the GFI impedance model had been previously adjusted and studied based on experimental measurements. Indeed, if the model does not represent well the converter impedance, the coordinated strategy will produce more accurate results.

The identified MLG (Figure 6.11) presented satisfactory accuracy for up to 2 kHz, which is the limit imposed by the identification of Z_{AFR}. Beyond this frequency, no conclusion could be inferred about the system's stability. Even within the accurate range, it was shown that the resonant peaks and phase jumps were not satisfactorily identified, and that is exactly the region in which the AFR behaves as a nonpassive component and instabilities may arise. In the tested scenario, it was not a problem since the MLG magnitude was far below 0 dB. Thus, even with a certain inaccuracy level, the identification of the MLG remains useful to determine how far the system is from an unstable operation. By establishing safe gain and phase margins, following the reasoning behind the *forbidden region* criteria, it is possible to determine safe operation regions. As an example, by looking only at the identified magnitude response, it is possible to ensure stability by keeping it below 0 dB. Actually, this is exactly the Middlebrook criterion, briefly explained in section 2.1.2, which establishes that a sufficient condition for stability is keeping the MLG inside the unit circle in the complex plane (under the assumption that the MLG contains no unstable poles).

Thereafter, an analysis was carried out regarding the impact of impedances placed between the GFI and the AFR on the MLG assessment through identification. It was shown that neither the MLG_C nor the MLG_S strategies are capable of identifying the actual MLG frequency response. In the system under study, with a series inductor and a series capacitor, both strategies manage to estimate the MLG up to approximately 2 kHz when the impedances in between are almost negligible. Since that is also the frequency up to which the MLG identification produced accurate results, both strategies could be used with no considerable performance reduction if the inductor and the capacitor values are kept around tens of µH and tens of µF. For higher values of the series inductor, the MLG_S diverges more from the actual MLG compared with the MLG_C; in this case, the coordinated strategy is recommended. As it was experimentally shown, the MLG_C could assert about the system's stability even for exaggerated inductor values in Z_s.

7 Conclusion and Future Work

This work addressed three main aspects—the stability of converter-based networks, the system identification, and the controller of a GFI. In all three, the concept of impedance was at the core of the analysis. Through the impedance-based criteria, it was shown how the overall stability of an interconnected system can be investigated by looking at the terminal characteristics of the PECs. Via the cross-correlation method, associated with the PRBS injection, it was demonstrated how the PECs themselves can be used to identify an impedance of interest. For the GFI controller, the impedance model and measurement enabled the performance of the controller to be analyzed, diagnosed, and the stability of the AFR-GFI system to be assessed.

Concerning the identification scheme, the PRBS technique associated with the proposed post-processing methods produced satisfactory results, not only for the case study presented in Chapter 3, but also for the GFI impedance measurement in Chapter 5, and the MLG assessment in Chapter 6. Roughly speaking, the identification scheme was capable of accurately estimating the impedances specially within an intermediate frequency range, from approximately twice the fundamental grid-voltage frequency up to at least one tenth of the PRBS generating frequency, being the lower limit mostly due to the ac steady-state components suppression and the upper one due to the SNR. Even with the limited identification bandwidth, the resulting accuracy was adequate for both the stability assessment and the controller analysis.

Nevertheless, there is room for improvement and future work related to the identification. First of all, some works employ the post-processing directly in the frequency domain, with no need of explicitly calculating the cross-correlation function between input and output (SIEGERS *et al.*, 2013; MARTIN *et al.*, 2013; ROINILA *et al.*, 2019). Even though this approach imposes some restrictions related to the disturbance generating frequency and sampling to avoid aliasing, it enables a more flexible choice of the disturbing signal so that other binary sequences—as the IRS and the DIBS—suit well the application. In order to apply frequency-domain-based post-processing methods, however, it is also necessary to implement a synchronization mechanism between the disturbance injection and the steady-state components of the system, which burdens the communication/acquisition system with new requirements.

Regarding the GFI, the DB controller presented notable results. Its effectiveness when facing load transients and when supplying nonlinear loads has been experimentally demonstrated. Also, a comprehensive impedance analysis of the DB-GFI was done—the impact of parameter mismatches over the impedance was shown, the impedance model was contrasted with the developed analytical model, and, most importantly, the impedance measurement allowed the controller to be improved through the R-DB version. In fact, from the impedance measurement and the analytical model comparison, the effect of a resistive term (R_L) was made clear. By modeling this resistance in the DB equations, the desired DB characteristic could be retrieved, considerably reducing the impedance of the converter within the low-frequency, inductive range at the expense of increasing the high-frequency impedance around 2 kHz, which is expected by the ideal DB behavior. It was shown that, depending on the spectral content of the load current, the value of the parameter R_L^m that results in the lowest voltage distortion may not correspond to the perfect match between R_L^m and R_L. It occurs as a consequence of the trade-off between the low and the high-frequency impedance change.

As for the identification scheme, some improvement points can be listed for the controller. As future work, the even-order harmonic issue has to be further explored. Preliminary tests showed that it may be related to the dc-link voltage ripple, which is not symmetric over a fundamental cycle for the hardware topology utilized (measured over one of the dc-link capacitors). Nevertheless, more detailed investigations must be done. Another aspect is that recent works have brought in a higher-bandwidth, FPGA-based DB version (BUSO *et al.*, 2019). Although the DSP-based version represents a cost-effective, easy-to-implement solution, the FPGA-based DB presents considerable improvements in dynamics and should not be set aside in future research.

With regard to the stability assessment, the strategies for obtaining the MLG frequency response provided satisfactory results; yet, some limitations exist. First of all, the accuracy of the identified MLG depends on the accuracy of the impedance identification performed by the PECs individually. Moreover, it will be limited by the converter that exhibits the worst accuracy. In the discussed case, the MLG precision was limited by the identification performed by the GFI. Another drawback is that the MLG content in the nonpassive regions could not be correctly identified since, for the tested system, they were very narrow and would also require a great disturbance energy to excite the current above noise levels. As a consequence, in order to use the identified MLG to make decisions concerning the network operation, safe margins are recommended to be used. Moreover, it was shown that passive impedances located throughout the network may undermine the MLG estimation.

Using the identified MLG response in adaptive rules for the system is a major point for future work. The main advantage and interest behind the online identification is being able to use it to adapt the controllers of the PECs lest the overall stability be at risk. Recent works as (ROINILA *et al.*, 2019) have demonstrated the feasibility of utilizing the real-time stability assessment through PBRS identification along with adaptive techniques.

Although the studied stability assessment system is capable of estimating how far the network is from an unstable operation, a major drawback is that, once an instability is triggered, the impedance identification is not possible anymore. In other words, it is not possible to identify the MLG for a system that is already unstable. In an isolated microgrid, for instance, if a load connection provokes a step-change in the MLG that triggers an unstable oscillation, the identification system will not be able to assess the MLG frequency response anymore. To avoid this kind of issue, it is important to operate the system with safe stability margins. Another drawback is concerning systems having paralleled voltage-controlled converters, which is the case for networks operating with some types of droop control, for instance. In this case, unstable poles may be present in the MLG, which complicates the determination of stability margins (LIU *et al.*, 2020).

In conclusion, this work provided a better understanding on how an identification technique can be employed to analyze both the controller performance and the stability of a converter-based network. Details were given on the identification technique, providing valuable information on the post-treatment methods. The DB controller was also exposed in details—the predictive equations were cautiously derived, the impedance model was thoroughly presented, and the performance was experimentally evaluated. Finally, the stability of a two-converter system was evaluated, pointing out some difficulties that may arise in a real-world application.

Bibliography

ABDOLLAHI, H.; KHODAMORADI, A.; SANTI, E.; MATTAVELLI, P. Online Bus Impedance Estimation and Stabilization of DC Power Distribution Systems: A Method Based on Source Converter Loop-Gain Measurement. *Conference Proceedings - IEEE Applied Power Electronics Conference and Exposition - APEC*, v. 2020-March, p. 3371–3378, 2020.

AMIN, M.; MOLINAS, M. Small-Signal Stability Assessment of Power Electronics Based Power Systems: A Discussion of Impedance-and Eigenvalue-Based Methods. *IEEE Transactions on Industry Applications*, v. 53, n. 5, p. 5014–5030, 2017. ISSN 00939994.

BARKLEY, A.; SANTI, E. Improved online identification of a DC-DC converter and its control loop gain using cross-correlation methods. *IEEE Transactions on Power Electronics*, v. 24, n. 8, p. 2021–2031, 2009. ISSN 08858993.

BODE, G. H.; LOH, P. C.; NEWMAN, M. J.; HOLMES, D. G. An improved robust predictive current regulation algorithm. *IEEE Transactions on Industry Applications*, v. 41, p. 1720–1733, 11 2005. ISSN 00939994.

BOSE, B. K. Global energy scenario and impact of power electronics in 21st century. *IEEE Transactions on Industrial Electronics*, IEEE, v. 60, n. 7, p. 2638–2651, 2013. ISSN 02780046.

BUSO, S.; CALDOGNETTO, T.; BRANDAO, D. I. Dead-beat current controller for voltage source converters with improved large-signal response. *IEEE Transactions on Industry Applications*, IEEE, v. 2015, n. 2, p. 1588–1596, 2015. ISSN 00939994.

BUSO, S.; CALDOGNETTO, T.; LIU, Q. Analysis and Experimental Characterization of a Large-Bandwidth Triple-Loop Controller for Grid-Tied Inverters. *IEEE Transactions on Power Electronics*, IEEE, v. 34, n. 2, p. 1936–1949, feb 2019. ISSN 08858993. Disponível em: <https://ieeexplore.ieee.org/document/8357510/>.

BUSO, S.; FASOLO, S.; MATTAVELLI, P. Uninterruptible power supply multiloop control employing digital predictive voltage and current regulators. *IEEE Transactions on Industry Applications*, v. 37, n. 6, p. 1846–1854, 2001. ISSN 00939994.

BUSO, S.; MATTAVELLI, P. *Digital control in power electronics*. 2nd. ed. [S.l.]: Morgan & Claypool, 2006. v. 2. 1–158 p. ISSN 19319525. ISBN 1598291130.

CESPEDES, M.; SUN, J. Online grid impedance identification for adaptive control of grid-connected inverters. *2012 IEEE Energy Conversion Congress and Exposition, ECCE 2012*, p. 914–921, 2012.

GODOY, E. *Régulation industrielle - 2e éd: Outils de modélisation, méthodes et architectures de commande*. [S.l.]: Dunod, 2014. (Automatique et réseaux). ISBN 9782100721948.

GUERREIRO, J. F. Tese (Doutorado), 2020. Disponível em: <https://hdl.handle.net/20.500.12733/3014>.

GUERREIRO, J. F.; ARRUDA, V. C.; GUILLARDI, H.; POMILIO, J. A. Lcl filter design and damping analysis for grid-connected inverters in modern uncertain grid impedance conditions. *2021 IEEE Southern Power Electronics Conference, SPEC 2021*, 2021.

Guerreiro, J. F.; Guillardi Júnior, H.; Pomílio, J. A. An approach to the design of stable distributed energy resources. In: *2018 IEEE 19th Workshop on Control and Modeling for Power Electronics (COMPEL)*. [S.l.: s.n.], 2018. p. 1–8.

GUERREIRO, J. F.; JUNIOR, H. G.; POMILIO, J. A. Design procedures and prototyping of a full-bridge high frequency power inverter. *2019 IEEE 15th Brazilian Power Electronics Conference and 5th IEEE Southern Power Electronics Conference, COBEP/SPEC 2019*, 2019.

HAMPTON, R. L. T. A hybrid analog-digital pseudo random noise generator. *Simulation*, Sage Publications Sage CA: Thousand Oaks, CA, v. 4, n. 3, p. 179–199, 1965.

HARNEFORS, L.; WANG, X.; YEPES, A. G.; BLAABJERG, F. Passivity-Based Stability Assessment of Grid-Connected VSCs—An Overview. *IEEE Journal of Emerging and Selected Topics in Power Electronics*, IEEE, v. 4, n. 1, p. 116–125, mar 2016. ISSN 2168-6777. Disponível em: <http://ieeexplore.ieee.org/document/7298361/>.

HATZIARGYRIOU, N.; MILANOVIC, J.; RAHMANN, C.; AJJARAPU, V.; CANIZARES, C.; ERLICH, I.; HILL, D.; HISKENS, I.; KAMWA, I.; PAL, B.; POURBEIK, P.; SANCHEZ-GASCA, J.; STANKOVIC, A.; Van Cutsem, T.; VITTAL, V.; VOURNAS, C. Definition and Classification of Power System Stability - Revisited Extended. *IEEE Transactions on Power Systems*, IEEE, v. 36, n. 4, p. 3271–3281, 2021. ISSN 15580679.

IEEE Standard for the Specification of Microgrid Controllers. *IEEE Std 2030.7-2017*, p. 1–43, 2018.

KHODAMORADI, A.; LIU, G.; MATTAVELLI, P.; MESSO, T. Simultaneous Identification of Multiple Control Loops in DC Microgrid Power Converters. *IEEE Transactions on Industrial Electronics*, IEEE, v. 67, n. 12, p. 10641–10651, 2020. ISSN 15579948.

LI, Y.; GU, Y.; ZHU, Y.; JUNYENT-FERRE, A.; XIANG, X.; GREEN, T. C. Impedance Circuit Model of Grid-Forming Inverter: Visualizing Control Algorithms as Circuit Elements. *IEEE Transactions on Power Electronics*, v. 36, n. 3, p. 3377–3395, 2021. ISSN 19410107.

LIAO, Y.; WANG, X. Impedance-Based Stability Analysis for Interconnected Converter Systems with Open-Loop RHP Poles. *IEEE Transactions on Power Electronics*, IEEE, v. 35, n. 4, p. 4388–4397, 2020. ISSN 19410107.

LIN, Y.; ETO, J. H.; JOHNSON, B. B.; FLICKER, J. D.; LASSETER, R. H.; PICO, H. N. V.; SEO, G.-S.; PIERRE, B. J.; ELLIS, A. *Research roadmap on grid-forming inverters*. [S.l.], 2020.

LIU, F.; LIU, J.; ZHANG, H.; XUE, D. Stability issues of Z+Z type cascade system in hybrid energy storage system (HESS). *IEEE Transactions on Power Electronics*, v. 29, n. 11, p. 5846–5859, 2014. ISSN 08858993.

LIU, Q.; CALDOGNETTO, T.; BUSO, S. Review and Comparison of Grid-Tied Inverter Controllers in Microgrids. *IEEE Transactions on Power Electronics*, IEEE, v. 35, n. 7, p. 7624–7639, 2020. ISSN 19410107.

LJUNG, L. *System Identification: Theory for the User*. [S.l.]: Prentice Hall PTR, 1999. (Prentice Hall information and system sciences series). ISBN 9780136566953.

LUHTALA, R.; ROINILA, T.; MESSO, T. Implementation of Real-Time Impedance-Based Stability Assessment of Grid-Connected Systems Using MIMO-Identification Techniques. *IEEE Transactions on Industry Applications*, IEEE, v. 54, n. 5, p. 5054–5063, 2018. ISSN 00939994.

MARONNI, I. A.; GUERREIRO, J. F.; POMILIO, J. A. Impedance-Based Stability Analysis for a Dead - Beat-Controlled Grid-Forming Inverter Using Cross-Correlation Methods. In: *2021 Brazilian Power Electronics Conference (COBEP)*. IEEE, 2021. p. 1–8. ISBN 978-1-6654-2129-4. Disponível em: <https://ieeexplore.ieee.org/document/9684106/>.

MARTIN, D.; NAM, I.; SIEGERS, J.; SANTI, E. Wide bandwidth three-phase impedance identification using existing power electronics inverter. *Conference Proceedings - IEEE Applied Power Electronics Conference and Exposition - APEC*, IEEE, n. 2, p. 334–341, 2013.

MARTIN, D.; SANTI, E. Autotuning of digital deadbeat current controllers for grid-tie inverters using wide bandwidth impedance identification. *IEEE Transactions on Industry Applications*, v. 50, n. 1, p. 441–451, 2014. ISSN 00939994.

MIAO, B.; ZANE, R.; MAKSIMOVIĆ, D. System identification of power converters with digital control through cross-correlation methods. *IEEE Transactions on Power Electronics*, v. 20, n. 5, p. 1093–1099, 2005. ISSN 08858993.

MIDDLEBROOK, R. D. Input filter considerations in design and application of switching regulators. *Rec. 1976 IEEE Ind. Appl. Soc. Annu. Meeting*, p. 366–382, 1976.

MU, P.; MCGRATH, B.; HOLMES, D. G.; TEIXEIRA, C. Small Signal Stability Analysis of Parallel Connected Grid-Tied Inverters with Direct and Self Synchronisation of the Phase Locked Loop. *ECCE 2020 - IEEE Energy Conversion Congress and Exposition*, p. 6197–6204, 2020.

PENG, Q.; JIANG, Q.; YANG, Y.; LIU, T.; WANG, H.; BLAABJERG, F. On the Stability of Power Electronics-Dominated Systems: Challenges and Potential Solutions. *IEEE Transactions on Industry Applications*, IEEE, v. 55, n. 6, p. 7657–7670, 2019. ISSN 19399367.

PENG, X.; YANG, H. Stability analysis of multi-paralleled grid-connected inverters including the distribution parameter characteristics of transmission lines. *CSEE Journal of Power and Energy Systems*, v. 6, 2020. ISSN 20960042.

PETRIC, I.; MATTAVELLI, P.; BUSO, S. Passivation of grid-following vscs: A comparison between active damping and multi-sampled pwm. TechRxiv, 2022.

PINTELON, R.; SCHOUKENS, J. *System identification: a frequency domain approach*. [S.l.]: John Wiley & Sons, 2012.

RICCOBONO, A.; LIEGMANN, E.; MONTI, A.; Castelli Dezza, F.; SIEGERS, J.; SANTI, E. Online wideband identification of three-phase AC power grid impedances using an existing grid-tied power electronic inverter. *2016 IEEE 17th Workshop on Control and Modeling for Power Electronics, COMPEL 2016*, IEEE, v. 00, n. c, 2016.

RICCOBONO, A.; MIRZ, M.; MONTI, A. Noninvasive Online Parametric Identification of Three-Phase AC Power Impedances to Assess the Stability of Grid-Tied Power Electronic Inverters in LV Networks. *IEEE Journal of Emerging and Selected Topics in Power Electronics*, IEEE, v. 6, n. 2, p. 629–647, 2018. ISSN 21686785.

RICCOBONO, A.; SANTI, E. Comprehensive review of stability criteria for DC power distribution systems. *IEEE Transactions on Industry Applications*, IEEE, v. 50, n. 5, p. 3525–3535, 2014. ISSN 19399367.

ROCABERT, J.; LUNA, A.; BLAABJERG, F.; RODRÍGUEZ, P. Control of Power Converters in AC Microgrids. *IEEE Transactions on Power Electronics*, v. 27, n. 11, p. 4734–4749, nov 2012. ISSN 0885-8993. Disponível em: <http://ieeexplore.ieee.org/document/6200347/>.

ROINILA, T.; ABDOLLAHI, H.; ARRUA, S.; SANTI, E. Real-Time Stability Analysis and Control of Multiconverter Systems by Using MIMO-Identification Techniques. *IEEE Transactions on Power Electronics*, IEEE, v. 34, n. 4, p. 3948–3957, 2019. ISSN 08858993.

ROINILA, T.; ABDOLLAHI, H.; SANTI, E. Frequency-Domain Identification Based on Pseudorandom Sequences in Analysis and Control of DC Power Distribution Systems: A Review. *IEEE Transactions on Power Electronics*, Institute of Electrical and Electronics Engineers Inc., v. 36, n. 4, p. 3744–3756, apr 2021. ISSN 0885-8993. Disponível em: <https://ieeexplore.ieee.org/document/9200539/>.

ROINILA, T.; HELIN, T.; VILKKO, M.; SUNTIO, T.; KOIVISTO, H. Circular correlation based identification of switching power converter with uncertainty analysis using fuzzy density approach. *Simulation Modelling Practice and Theory*, Elsevier B.V., v. 17, n. 6, p. 1043–1058, 2009. ISSN 1569190X. Disponível em: <http://dx.doi.org/10.1016/j.simpat.2009.03.006>.

ROINILA, T.; MESSO, T.; SANTI, E. MIMO-identification techniques for rapid impedance-based stability assessment of three-phase systems in DQ Domain. *IEEE Transactions on Power Electronics*, IEEE, v. 33, n. 5, p. 4015–4022, 2018. ISSN 08858993.

ROINILA, T.; VILKKO, M.; Jian Sun. Online Grid Impedance Measurement Using Discrete-Interval Binary Sequence Injection. *IEEE Journal of Emerging and Selected Topics in Power Electronics*, IEEE, v. 2, n. 4, p. 985–993, dec 2014. ISSN 2168-6777. Disponível em: <http://ieeexplore.ieee.org/document/6897911/>.

ROINILA, T.; VILKKO, M.; SUN, J. Broadband methods for online grid impedance measurement. *2013 IEEE Energy Conversion Congress and Exposition, ECCE 2013*, IEEE, p. 3003–3010, 2013.

SALIS, V.; COSTABEBER, A.; COX, S. M.; ZANCHETTA, P. Stability assessment of power-converter-based AC systems by LTP theory: Eigenvalue analysis and harmonic impedance estimation. *IEEE Journal of Emerging and Selected Topics in Power Electronics*, v. 5, n. 4, p. 1513–1525, 2017. ISSN 21686785.

SIEGERS, J.; SANTI, E.; BARKLEY, A. Wide bandwidth system identification of MVDC distribution system by applying perturbations to an existing converter. *2013 IEEE Electric Ship Technologies Symposium, ESTS 2013*, IEEE, p. 434–441, 2013.

SILVA, S. M.; LOPES, B. M.; FILHO, B. J.; CAMPANA, R. P.; BOAVENTURA, W. C. Performance evaluation of PLL algorithms for single-phase grid-connected systems. *Conference Record - IAS Annual Meeting (IEEE Industry Applications Society)*, v. 4, n. 1, p. 2259–2263, 2004. ISSN 01972618.

SIMÕES, M. G.; FARRET, F. A. *Modeling Power electronics and interfacing energy conversion systems*. [S.l.]: John Wiley & Sons, 2016.

SUN, J. Impedance-Based Stability Criterion for Grid-Connected Inverters. *IEEE Transactions on Power Electronics*, IEEE, v. 26, n. 11, p. 3075–3078, nov 2011. ISSN 0885-8993. Disponível em: <http://ieeexplore.ieee.org/document/5741855/>.

SYPE, D. V. de; GUSSEME, K. D.; BOSSCHE, A. V. den; MELKEBEEK, J. Small-signal laplace-domain analysis of uniformly-sampled pulse-width modulators. In: . IEEE. p. 4292–4298. ISBN 0-7803-8399-0. Disponível em: <http://ieeexplore.ieee.org/document/1354760/>.

UNDRILL, J. M.; KOSTYNIAK, T. E. Subsynchronous oscillations part 1 — comprehensive system stability analysis. *IEEE Transactions on Power Apparatus and Systems*, v. 95, n. 4, p. 1446–1455, jul 1976. ISSN 00189510. Disponível em: <http://ieeexplore.ieee.org/document/1601842/>.

WANG, X.; BLAABJERG, F. Harmonic Stability in Power Electronic-Based Power Systems: Concept, Modeling, and Analysis. *IEEE Transactions on Smart Grid*, IEEE, v. 10, n. 3, p. 2858–2870, 2019. ISSN 19493053.

WANG, Y.; WANG, X.; BLAABJERG, F.; CHEN, Z. Harmonic instability assessment using state-space modeling and participation analysis in inverter-fed power systems. *IEEE Transactions on Industrial Electronics*, IEEE, v. 64, n. 1, p. 806–816, 2017. ISSN 02780046.

YOON, C.; BAI, H.; BERES, R. N.; WANG, X.; BAK, C. L.; BLAABJERG, F. Harmonic stability assessment for multiparalleled, grid-connected inverters. *IEEE Transactions on Sustainable Energy*, IEEE, v. 7, n. 4, p. 1388–1397, 2016. ISSN 19493029.

APPENDIX A – Details on the Modulation

This appendix presents more details on the modulation strategy utilized, describing how the relation between the modulating signal m and the dc-link voltage V_{dc} can be obtained. As mentioned in section 4.1, two-level SPWM is used in this work, as shown in the diagram in Figure A.1.

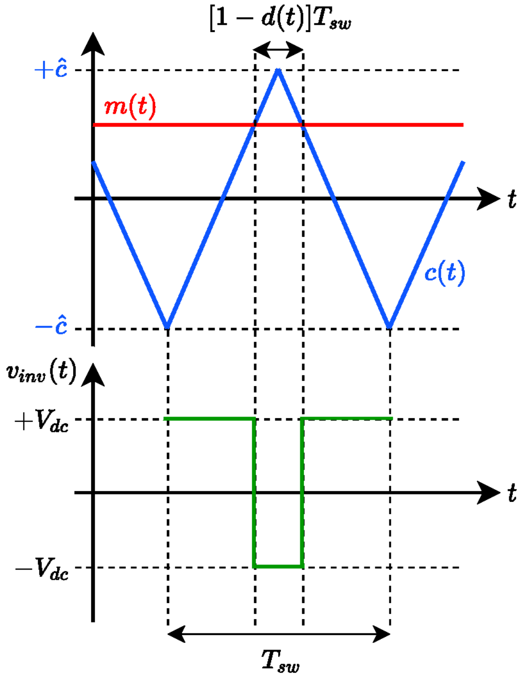

Figure A.1 – Two-level PWM diagram.

The upper part of the figure presents the triangular carrier $c(t)$ whose amplitude is given by $\hat{c}$. The carrier frequency determines the switching period, denoted as T_{sw}. The modulating signal $m(t)$ is considered to be constant within a switching cycle. The lower part of the figure presents the switched voltage v_{inv} at the output of the inverter bridge. Note that, when $m(t) > c(t)$, $v_{inv}(t)$ is equal to the dc voltage; otherwise, it is equal to minus the dc voltage. This results in a switched voltage with a duty-cycle $d(t)$, defined as the ration between the positive-voltage time and the switching period.

By triangle similarity, the relation

$$\frac{2\hat{c}}{T_{sw}} = \frac{\hat{c} - m(t)}{[1 - d(t)]T_{sw}}, \tag{A.1}$$

can be written based on the major triangle formed by the carrier itself and the tiny one formed between the modulating signal and the carrier peak. From (A.1), the duty-cycle can be written as a function of the modulating signal, as in

$$d(t) = \frac{1}{2}\left[1 + \frac{m(t)}{\hat{c}}\right], \tag{A.2}$$

Also, the average value of $v_{inv}(t)$ within a switching cycle can be calculated as

$$\langle v_{inv}\rangle(t) = V_{dc}d(t) - V_{dc}[1 - d(t)] = V_{dc}[2d(t) - 1]. \tag{A.3}$$

By substituting (A.2) into (A.4),

$$\langle v_{inv}\rangle(t) = V_{dc} \cdot \frac{m(t)}{\hat{c}}, \tag{A.4}$$

which relates the modulating signal with the average voltage produced by the inverter in a switching cycle. In the presented application, the carrier has unitary amplitude ($\hat{c} = 1$), thus

$$\langle v_{inv}\rangle(t) = V_{dc} \cdot m(t). \tag{A.5}$$

This is the equation used to derive (4.5) in Chapter 4.

APPENDIX B – Voltage-Loop Deadbeat Equation

This Appendix concerns the development of (4.8). The notation follows the same principles of section 4.2, with the discrete independent variables k and n representing the f_{sw} and the $f_{sw}/2$ operation rate domains, respectively.

By integrating the output voltage over the interval $[k, k+1]$,

$$v_o(k+1) = v_o(k) + \frac{1}{C^m f_{sw}} i_c(k), \tag{B.1}$$

and over $[k+1, k+2]$,

$$v_o(k+2) = v_o(k+1) + \frac{1}{C^m f_{sw}} i_c(k+2), \tag{B.2}$$

the following equation can be deduced:

$$v_o(k+2) = v_o(k) + \frac{1}{C^m f_{sw}} \left[i_c(k+1) + i_c(k) \right]. \tag{B.3}$$

Since the inductor current (i_L) is controlled by the inner loop, and the output current (i_o) is directly measured, the capacitor current can be considered to be indirectly controlled, such that

$$i_c(k) = i_c^{ref}(k-2) \tag{B.4}$$

holds, with i_c^{ref} being a reference value analogous to the inductor current reference (i_{ref}). Thus, rewriting (B.3) in terms of i_c^{ref}, one obtains

$$v_o(k+2) = v_o(k) + \frac{1}{C^m f_{sw}} \left[i_c^{ref}(k-1) + i_c^{ref}(k-2) \right]. \tag{B.5}$$

Assuming that i_c^{ref} does not vary very much from one switching cycle to another, (B.5) can be written as

$$v_o(k+2) = v_o(k) + \frac{2}{C^m f_{sw}} i_c^{ref}(k-2). \tag{B.6}$$

For the reasons explained in section 4.2.2, the voltage-loop voltage equation must be calculated at half the rate of the inner loop. Hence, by sampling (B.6) at a rate equal to $f_{sw}/2$,

$$v_o(n+1) = v_o(n) + \frac{2}{C^m f_{sw}} i_c^{ref}(n-1) \tag{B.7}$$

is obtained.

In order to find a predictive equation that zeroes the voltage error, (B.7) can be written in incremental terms as

$$\Delta v_o(n+1) = \Delta v_o(n) + \frac{2}{C^m f_{sw}} \Delta i_c^{ref}(n-1). \tag{B.8}$$

The control law that ensures zero voltage error in the next sampling instant is given by

$$\Delta i_c^{ref}(n) = -\frac{C^m f_{sw}}{2} \Delta v_o(n+1), \tag{B.9}$$

since $\Delta v_o(n+1) = 0$ when (B.9) is substituted into (B.8). Note, however, that $\Delta v_o(n+1)$ must be known in order to apply (B.9). One option is to obtain it through a Luenberger space observer. For a state-space representation given by

$$\begin{cases} x(n+1) &= Ax(n) + Bu(n) \\ y(n) &= Cx(n) + Du(n) \end{cases} \tag{B.10}$$

the observer equations can be written as

$$\begin{cases} \hat{x}(n+1) &= A\hat{x}(n) + Bu(n) + L[y(n) - \hat{y}(n)] \\ \hat{y}(n) &= C\hat{x}(n) + Du(n) \end{cases} \tag{B.11}$$

such that the dynamics of the observer is defined by the eigenvalues of the matrix $A-LC$, with L being an design parameter.

Equation (B.8) can be regarded as a state-space representation with $x = \Delta v_o$, $u = \Delta i_c^{ref}$, $A = 1$, $B = 2/C^m f_{sw}$, $C = 1$, and $D = 0$. Thus,

$$A - LC = 1 - L. \tag{B.12}$$

Therefore, L must be chosen as 1 in order for the observer to present a deadbeat behavior (pole located at the origin). With this choice, the estimator becomes

$$\Delta \hat{v}_o(n+1) = \Delta v_o(n) + \frac{2}{C^m f_{sw}} \Delta i_c^{ref}(n-1). \tag{B.13}$$

From (B.9) and (B.13), the control law can be obtained:

$$\Delta i_c^{ref}(n) = -\frac{C^m f_{sw}}{2} \Delta v_o(n+1) \approx -\frac{C^m f_{sw}}{2} \Delta \hat{v}_o(n+1), \tag{B.14}$$

$$\Delta i_c^{ref}(n) = -\Delta i_c^{ref}(n-1) + \frac{C^m \cdot f_{sw}}{2} \cdot [v_{ref}(n) - v_o(n)]. \tag{B.15}$$

APPENDIX C – High-Frequency Interactions in the AFR-GFI System

In addition to the LCL filter, the AFR has an EMI filter, whose topology is depicted in Figure C.1. For the experimental results presented throughout this dissertation, this EMI filter had been removed in order to avoid the high-frequency interaction discussed in this appendix. Even though this effect is out of the scope of this dissertation, it represents a practical problem that might be present in interconnected-converter systems, and may cause power quality or stability issues.

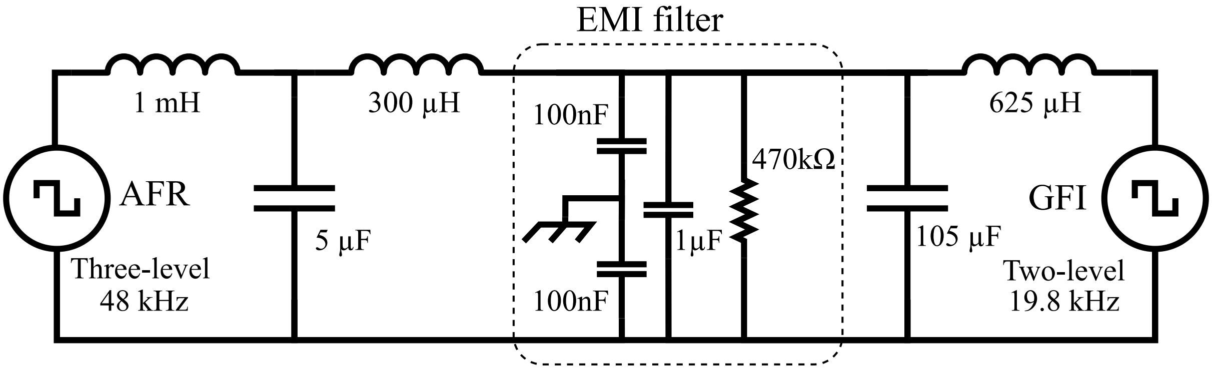

Figure C.1 – High-frequency representation of the AFR-GFI system, highlighting the AFR's EMI filter topology.

When the AFR and the GFI are interconnected, the EMI filter provides a low-impedance path for the high-frequency content produced by the switching of both converters. For high frequencies, beyond the controller's bandwidths, both converters can be regarded as switched voltage sources (see Figure C.1) with a certain spectral content around the switching frequency, which depends on the modulation in use. The AFR utilizes a three-level SPWM with the carrier frequency set at 24 kHz. Due to the three-level modulation, the most relevant spectral content of the switched voltage produced at the full-bridge's terminals appears around 48 kHz. Even though this high-frequency content is filtered by the AFR's LCL filter, it is not completely suppressed and appears over the EMI filter. The same occurs for the GFI, whose 19.8 kHz switched voltage, although attenuated by the LC filter, produces a current flow through the EMI filter.

Figure C.2 shows the GFI output current when the AFR is on standby mode, i.e. when its PWM and control are not enabled. In this case, the impedance seen by the GFI corresponds solely to the AFR's passive filters, which includes the EMI filter, the 300 μH inductor, and the 5 μF capacitor. Note from the spectrum that the polluted

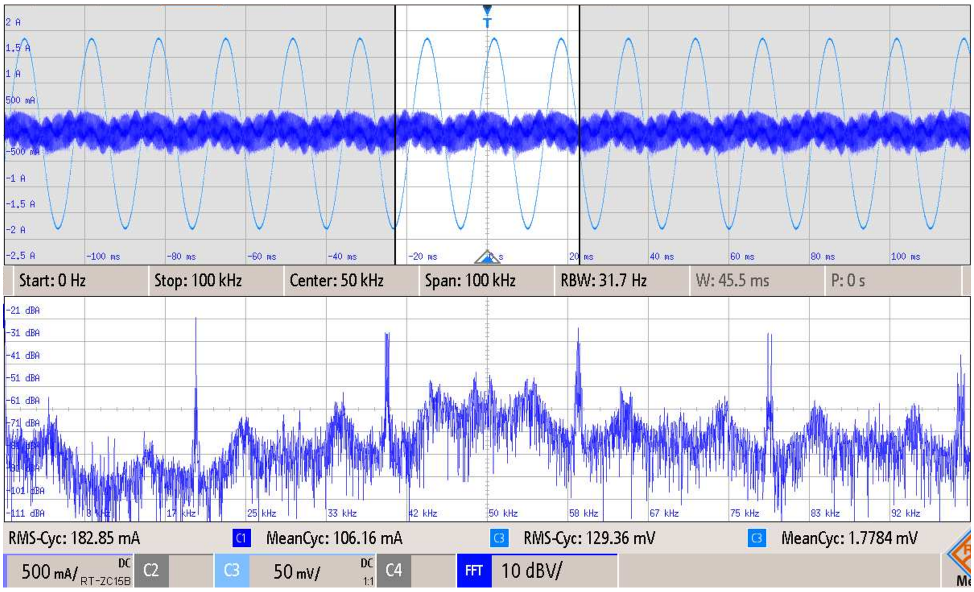

Figure C.2 – High-frequency interaction between the AFR and the GFI when the AFR's EMI filter is connected. The AFR is on standby mode (PWM disabled). The voltage (in light blue) and the current (in dark blue) are measured at the output of the GFI's LC filter.

current is mostly composed by the GFI switching frequency (19.8 kHz) and its multiples.

Similar results are shown in Figure C.3, but for the AFR's PWM enabled. In Figure C.3a the AFR is draining no current while, in Figure C.3b, it drains a current of approximately 6 A_{peak}. Now, the GFI output current contains the high-frequency components produced by the GFI itself, which circulates mostly through the EMI filter, and also the components produced by the AFR. In fact, the same high-frequency voltage that the AFR produces over the EMI filter will also be over the GFI's LC filter, causing a current to circulate towards the GFI. Thus, the AFR high-frequency pollution appears in the measured current as well. Looking at the spectra, besides the frequency components already present in Figure C.2, new ones appear around the multiples of the AFR's carrier frequency. Note that, despite the three-level modulation, not only the components that are integer multiples of 48 kHz appear, but also the multiples of 24 kHz (even though with lower magnitude). This *imperfection* in the capability of the three-level modulation to double the apparent switching frequency is mostly related to transistors' raise and falling times and to deadtime.

Problems may arise due to the high-frequency pollution if this current is used by the controller and the signals are not sufficiently filtered by the acquisition/conditioning circuitry, due to the aliasing effect. In the tested case, the DB controller managed to maintain the desired voltage despite the output current pollution—which is fed back into the voltage loop (see Figure 4.5). The denoising filter set at 19.8 kHz was probably enough to avoid complications related to the external pollution produced by the AFR. Also, the

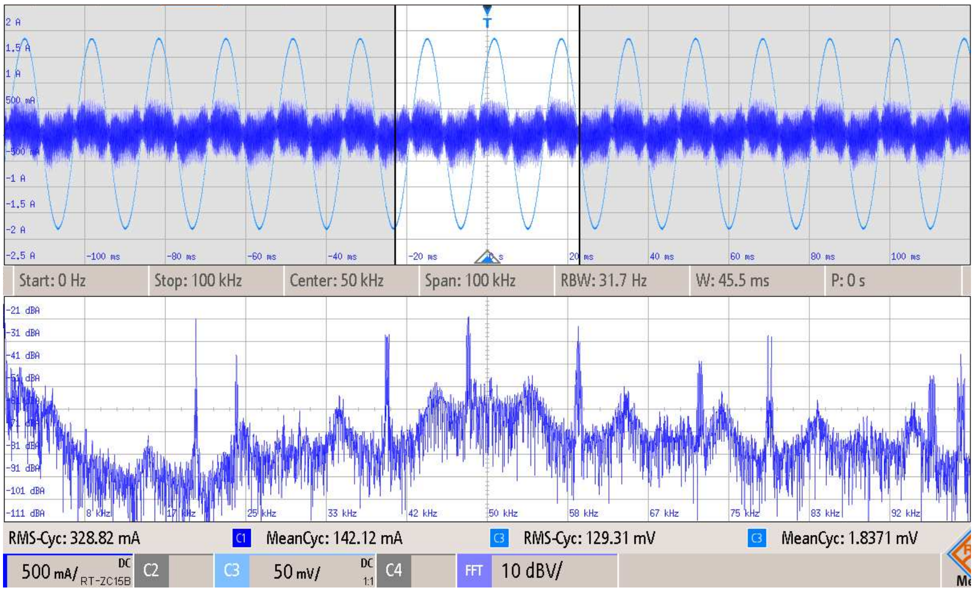

(a)

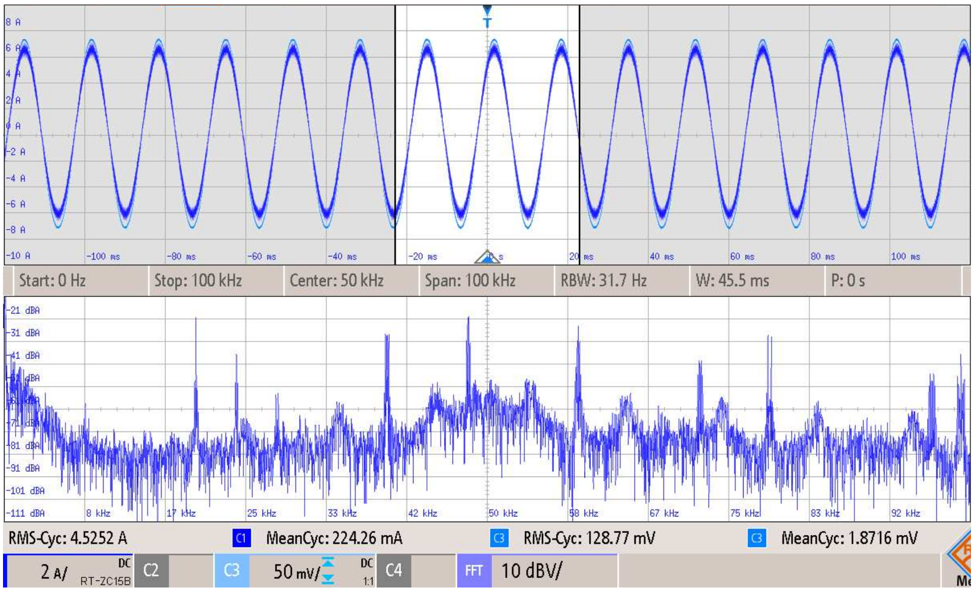

(b)

Figure C.3 – High-frequency interaction between the AFR and the GFI when the AFR's EMI filter is connected. The AFR is active (PWM enabled) and draining (a) no current and (b) 6 A_{peak}. The voltage (in light blue) and the current (in dark blue) are measured at the output of the GFI's LC filter.

identification method was not compromised by this high-frequency pollution, as stated by Figure C.4, which shows the R-DB impedance (discussed in Chapter 5) identified by the AFR in both scenarios—with and without the EMI filter connected. Nevertheless, depending on the sampling and switching frequencies involved in a multi-converter system, uncertainties caused by aliasing are assumed to appear in the identified response.

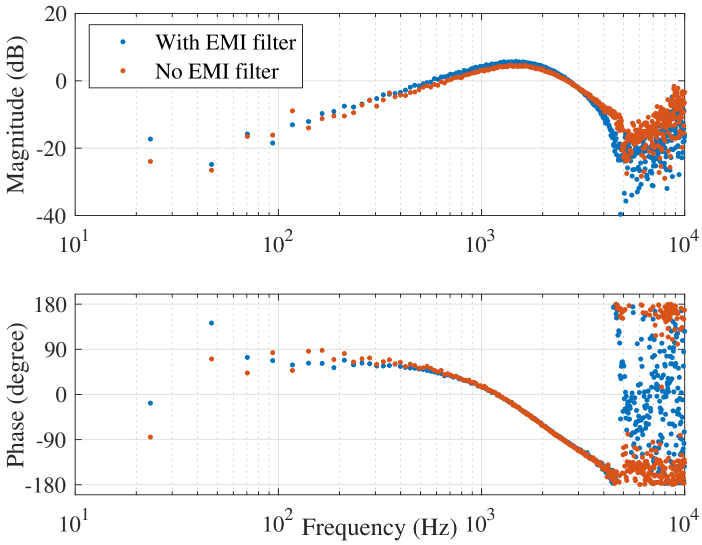

Figure C.4 – R-DB impedance identified by the AFR considering the scenarios with and without the EMI filter.

APPENDIX D – R-DB-GFI Impedance Model with PRBS

The PRBS is injected in the modulator as shown in Figure D.1, which depicts the current-loop control diagram of the R-DB.

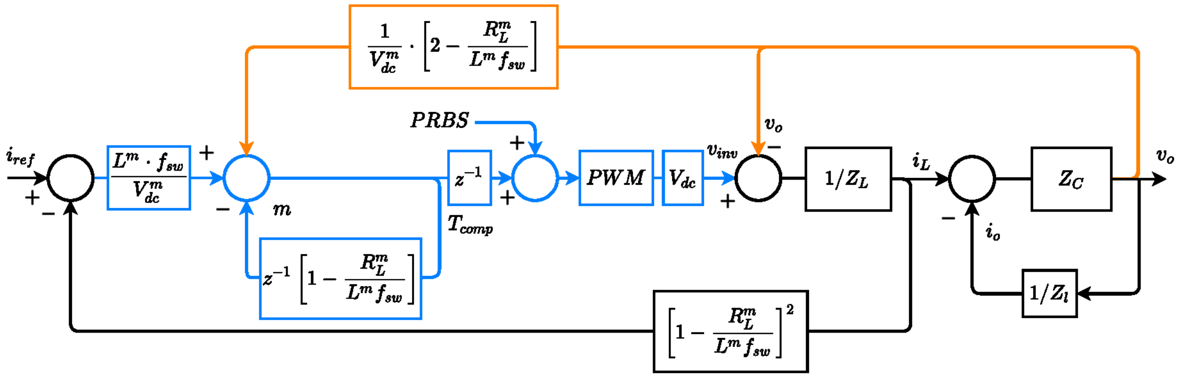

Figure D.1 – R-DB current-control diagram including the PRBS injection.

The PRBS can be regarded as a new input for the system, and can be included in the Norton equivalent circuit of the inner loop as a new current source, as presented in Figure D.2. The source has a value of $H^i_{prbs}PRBS$, with H^i_{prbs} corresponding to the transfer function between the PRBS and the inductor current i_L. Indeed, by analyzing

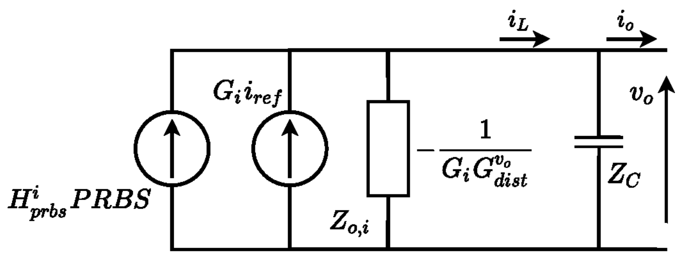

Figure D.2 – Current-loop impedance model including the PRBS.

the Norton equivalent circuit, H^i_{prbs} can be found as the relation between the PRBS and i_L when both i_{ref} and v_o are zero, as

$$H^i_{prbs} = \left.\frac{i_L}{PRBS}\right|_{i_{ref},v_o=0}, \tag{D.1}$$

which can be obtained by rearranging the block diagram as in Figure D.3.

With this modified impedance model for the current loop, the effect of the PRBS can be extended to the voltage controller. The new Norton equivalent circuit trans-

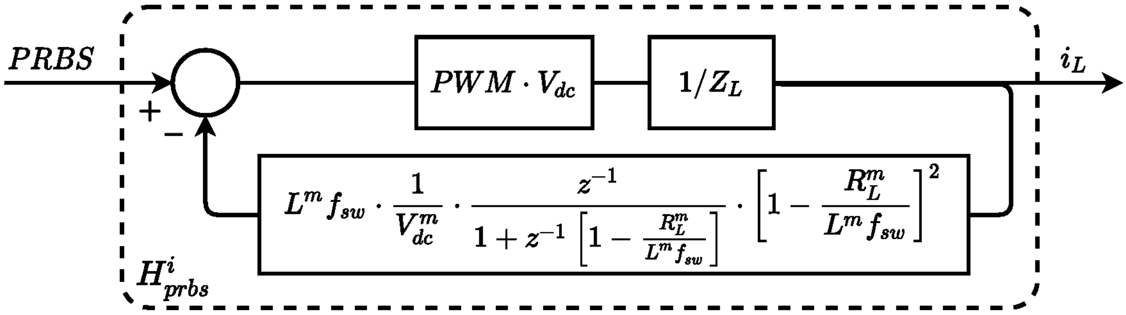

Figure D.3 – Simplified diagram for obtaining H^i_{prbs}.

forms the relation previously given by (5.8) into

$$H^i_{prbs}PRBS + G_i i_{ref} - Z_{o,i}v_o = i_o + i_c, \tag{D.2}$$

which can be represented in the voltage-loop block diagram as depicted in Figure D.4

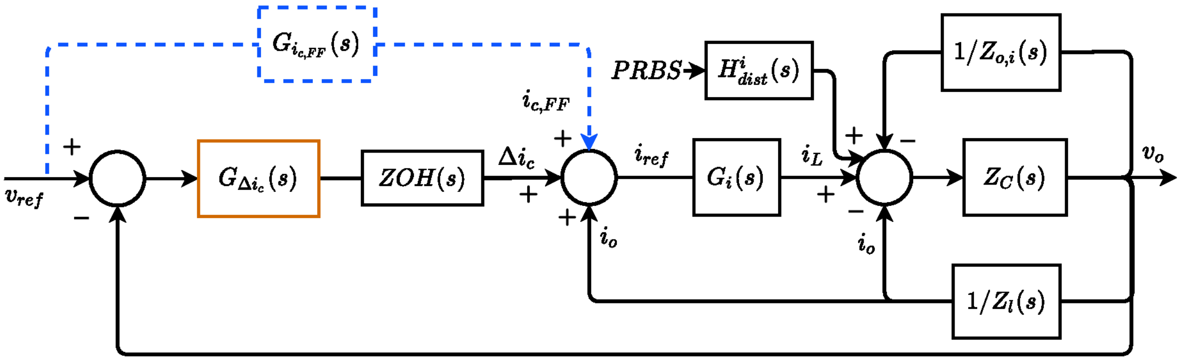

Figure D.4 – R-DB voltage-control diagram including the PRBS.

In the Thévenin equivalent circuit of the complete impedance model, the PRBS can be modeled as a voltage source of value $H^v_{prbs}PRBS$. The transfer function H^v_{prbs} can be derived as the relation between the PRBS and the output voltage v_o when the load current and the voltage reference are zero, as denoted in

$$H^v_{prbs} = \left.\frac{v_o}{PRBS}\right|_{v_{ref}, i_o=0}, \tag{D.3}$$

according to the circuit in Figure D.5.

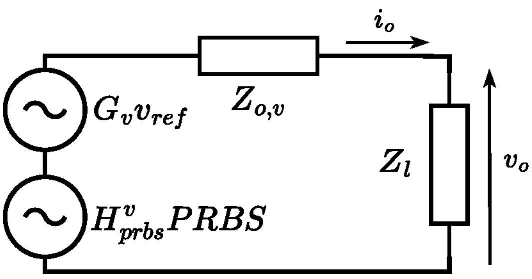

Figure D.5 – Voltage-loop impedance model including the PRBS.

By reorganizing the control diagram, the simplified block diagram for obtaining H^v_{prbs} becomes the one depicted in Figure D.6.

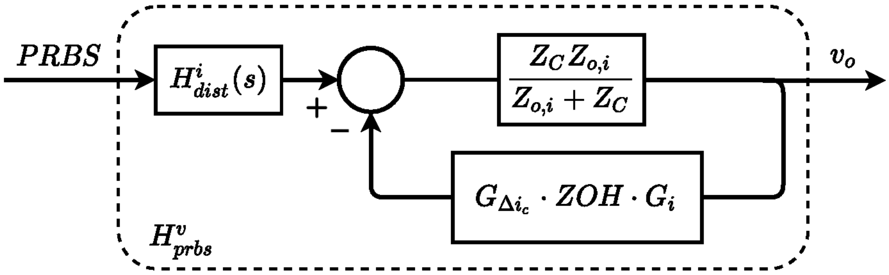

Figure D.6 – Simplified diagram for obtaining H^v_{prbs}.